

11-7-2011

# Theoretical Investigations of Communication in the Microcirculation: Conducted Responses, Myoendothelial Projections and Endothelium Derived Hyperpolarizing Factor

Sridevi Nagaraja

*Florida International University*, [snaga001@fiu.edu](mailto:snaga001@fiu.edu)

**DOI:** 10.25148/etd.FI11120802

Follow this and additional works at: <https://digitalcommons.fiu.edu/etd>

---

## Recommended Citation

Nagaraja, Sridevi, "Theoretical Investigations of Communication in the Microcirculation: Conducted Responses, Myoendothelial Projections and Endothelium Derived Hyperpolarizing Factor" (2011). *FIU Electronic Theses and Dissertations*. 520.  
<https://digitalcommons.fiu.edu/etd/520>

This work is brought to you for free and open access by the University Graduate School at FIU Digital Commons. It has been accepted for inclusion in FIU Electronic Theses and Dissertations by an authorized administrator of FIU Digital Commons. For more information, please contact [dcc@fiu.edu](mailto:dcc@fiu.edu).

FLORIDA INTERNATIONAL UNIVERSITY

Miami, Florida

THEORETICAL INVESTIGATIONS OF INTERCELLULAR COMMUNICATION IN THE  
MICROCIRCULATION: CONDUCTED RESPONSES, MYOENDOTHELIAL  
PROJECTIONS AND ENDOTHELIUM DERIVED HYPERPOLARIZING FACTOR

A dissertation submitted in partial fulfillment of

the requirements for the degree of

DOCTOR OF PHILOSOPHY

in

BIOMEDICAL ENGINEERING

by

Sridevi Nagaraja

2011

To: Dean Amir Mirmiran  
College of Engineering and Computing

This dissertation, written by Sridevi Nagaraja, and entitled Theoretical investigations of intercellular communication in the microcirculation: conducted responses, myoendothelial projections and endothelium derived hyperpolarizing factor, having been approved in respect to style and intellectual content, is referred to you for judgment.

We have read this dissertation and recommend that it be approved.

---

Wei-Chiang Lin

---

Anuradha Godavarty

---

Lidia Kos

---

Yen-Chih Huang

---

Nikolaos Tsoukias, Major Professor

Date of Defense: November 7, 2011

The dissertation of Sridevi Nagaraja is approved.

---

Dean Amir Mirmiran  
College of Engineering and Computing

---

Dean Lakshmi N. Reddi  
University Graduate School

Florida International University, 2011

## ACKNOWLEDGMENTS

I am extremely grateful to all my teachers for their time and effort towards my education. Dr. Adam Kapela who trained me initially and helped me understand the basics of mathematical modeling. I want to thank him for his patience and encouragement through every mistake I made during the learning process.

I want to thank my lab members Shabnam Namin, Luis Alonzo, Jaimit Parikh, Konstantinos Sebekos, Zenith Acosta, Carolina Bautista, Roxana Ordonez, Kumpal Madarasi and all others who made time fly.

I would like thank all my committee members Dr. Wei-Chiang Lin, Dr. Anuradha Godavarty, Dr Yen-Chih Huang and Dr. Lidia Kos who have provided advice and invaluable insight towards my dissertation.

I would like to acknowledge the support of the University Graduate School for providing me with the Dissertation Year Fellowship in the final year of my PhD.

I would like to extend my sincere thanks to Dr. Nikolaos Tsoukias for being such a great mentor. He invested a lot of his time in teaching me technical writing and presentation of scientific work. His patient yet persistent guidance has taught me to never give up on my goals and the value of critical thinking. He is a big part of the success of this dissertation and all my future accomplishments.

I would like to acknowledge my family, my mother, M.S.Gayathri, my brother, Aditya Nagaraja and two of my most favorite people in the world, Avani Mulchandani and Abhignyan Nagesetti for their unconditional love and support. I would like to acknowledge my father, M.K.Nagaraja, whose cherished memories always stay with me wherever I am and continue to guide me in everything I do.

ABSTRACT OF THE DISSERTATION

THEORETICAL INVESTIGATIONS OF INTERCELLULAR COMMUNICATION IN THE  
MICROCIRCULATION: CONDUCTED RESPONSES, MYOENDOTHELIAL  
PROJECTIONS AND ENDOTHELIUM DERIVED HYPERPOLARIZING FACTOR

by

Sridevi Nagaraja

Florida International University, 2011

Miami, Florida

Professor Nikolaos Tsoukias, Major Professor

The contractile state of microcirculatory vessels is a major determinant of the blood pressure of the whole systemic circulation. Continuous bi-directional communication exists between the endothelial cells (ECs) and smooth muscle cells (SMCs) that regulates calcium ( $\text{Ca}^{2+}$ ) dynamics in these cells. This study presents theoretical approaches to understand some of the important and currently unresolved microcirculatory phenomena.

Agonist induced events at local sites have been shown to spread long distances in the microcirculation. We have developed a multicellular computational model by integrating detailed single EC and SMC models with gap junction and nitric oxide (NO) coupling to understand the mechanisms behind this effect. Simulations suggest that spreading vasodilation mainly occurs through  $\text{Ca}^{2+}$  independent passive conduction of hyperpolarization in RMAs. Model predicts a superior role for intercellular diffusion of inositol (1,4,5)-trisphosphate ( $\text{IP}_3$ ) than  $\text{Ca}^{2+}$  in modulating the spreading response.

Endothelial derived signals are initiated even during vasoconstriction of stimulated SMCs by the movement of  $\text{Ca}^{2+}$  and/or  $\text{IP}_3$  into the EC which provide hyperpolarizing feedback to

SMCs to counter the ongoing constriction. Myoendothelial projections (MPs) present in the ECs have been recently proposed to play a role in myoendothelial feedback. We have developed two models using compartmental and 2D finite element methods to examine the role of these MPs by adding a sub compartment in the EC to simulate MP with localization of intermediate conductance calcium activated potassium channels ( $IK_{Ca}$ ) and  $IP_3$  receptors ( $IP_3R$ ). Both models predicted  $IP_3$  mediated high  $Ca^{2+}$  gradients in the MP after SMC stimulation with limited global spread. This  $Ca^{2+}$  transient generated a hyperpolarizing feedback of  $\sim 2-3mV$ .

Endothelium derived hyperpolarizing factor (EDHF) is the dominant form of endothelial control of SMC constriction in the microcirculation. A number of factors have been proposed for the role of EDHF but no single pathway is agreed upon. We have examined the potential of myoendothelial gap junctions (MEGJs) and potassium ( $K^+$ ) accumulation as EDHF using two models (compartmental and 2D finite element). An extra compartment is added in SMC to simulate micro domains (MD) which have  $NaK_{\alpha 2}$  isoform sodium potassium pumps. Simulations predict that MEGJ coupling is much stronger in producing EDHF than alone  $K^+$  accumulation. On the contrary,  $K^+$  accumulation can alter other important parameters (EC  $V_m$ ,  $IK_{Ca}$  current) and inhibit its own release as well as EDHF conduction via MEGJs. The models developed in this study are essential building blocks for future models and provide important insights to the current understanding of myoendothelial feedback and EDHF.

## TABLE OF CONTENTS

| CHAPTER  | PAGE   |
|--|--------|
| Chapter 1. Introduction  | 1      |
| 1.1 Motivation   | 1      |
| 1.2 Background   | 3      |
| 1.2.1 Potassium channels   | 4      |
| 1.2.2 Sodium- potassium pumps  | 5      |
| 1.2.3 Sodium- calcium exchanger  | 6      |
| 1.2.4 Calcium channels on plasma membrane                                      | 6      |
| 1.2.5 Calcium channels in SR   | 8      |
| 1.2.6 Sarcoplasmic/endoplasmic reticulum calcium pumps                         | 9      |
| 1.2.7 Calcium buffering  | 9      |
| 1.2.8 Theoretical modeling of vascular SMCs                                    | 10     |
| 1.2.9 Inward rectifier potassium channels                                      | 13     |
| 1.2.10 Small and intermediate conductance calcium activated potassium channels | 13     |
| 1.2.11 Theoretical modeling of vascular ECs                                    | 14     |
| <br>Chapter 2: Myoendothelial communication                                    | <br>16 |
| 2.1 Gap junction coupling  | 16     |
| 2.2 Endothelium derived controllers  | 17     |
| 2.2.1 Nitric oxide   | 17     |
| 2.2.2 Prostacyclin   | 19     |
| 2.2.3 Endothelium derived hyperpolarizing factor                               | 19     |
| 2.3 Myoendothelial feedback  | 20     |
| 2. 4 Theoretical modeling of myoendothelial communication                      | 21     |
| 2.4.1 Modeling of gap junction fluxes  | 21     |
| 2.4.2 Multicellular modeling   | 23     |
| <br>Chapter 3: Conducted responses in blood vessels                            | <br>25 |
| Abstract   | 25     |
| 3.1 Introduction   | 26     |
| 3.2 Methods  | 29     |
| 3.2.1 Multicellular vessel model   | 29     |
| 3.2.2 Intercellular communication  | 32     |
| 3.2.3 Length constants   | 36     |
| 3.2. 4 Numerical methods   | 37     |
| 3.3 Results  | 38     |
| 3.3.1 Electrical stimulation   | 38     |
| 3.3.2 Norepinephrin and actylcholine stimulation                               | 42     |
| 3.3.3 Effect of stimulus strength on membrane potential and calcium spread     | 47     |
| 3.4 Discussion   | 48     |
| 3.4.1 Role of gap junctions in $V_m$ spread                                    | 48     |
| 3.4.2 Current vs. voltage clamp stimulations                                   | 51     |
| 3.4.3 Physiological relevance of stimulatory protocols                         | 53     |
| 3.4.4 Role of endothelial cell $Ca^{2+}$ spread                                | 54     |

|  |     |
|--|-----|
| 3.4.5 IP <sub>3</sub> -mediated Ca <sup>2+</sup> spread vs. direct interendothelial Ca <sup>2+</sup> diffusion | 55  |
| 3.4.6 Effect of intercellular and transmembrane potential gradients  | 56  |
| 3.4.7 Effect of stimulus strength  | 57  |
| 3.4.9 Spread of relaxation   | 59  |
| 3.5 Model limitations  | 59  |
| 3.6 Conclusions  | 61  |
| <br>   |     |
| Chapter 4: Myoendothelial projections  | 63  |
| 4.1 Introduction   | 64  |
| 4.2 Model development:   | 66  |
| 4.2.1 Compartmental model  | 66  |
| 4.2.2 Finite element method model  | 71  |
| 4.3 Results  | 73  |
| 4.3.1 Global vs. local Ca <sup>2+</sup> and IP <sub>3</sub> changes  | 73  |
| 4.3.2 Effect of microprojections   | 77  |
| 4.3.3 IP <sub>3</sub> vs. Ca <sup>2+</sup> signaling   | 78  |
| 4.3.4 Parametric studies   | 79  |
| 4.4 Discussion   | 81  |
| 4.4.2 Feedback   | 82  |
| 4.4.3 Parametric studies   | 83  |
| 4.4.4 IP <sub>3</sub> vs. Ca <sup>2+</sup> diffusion   | 86  |
| 4.5 Limitations  | 88  |
| 4.6 Conclusion   | 89  |
| <br>   |     |
| Chapter 5: Endothelium derived hyperpolarizing factor  | 91  |
| 5.1 Introduction   | 92  |
| 5.2 Model development  | 95  |
| 5.2.1 Compartmental model  | 95  |
| 5.2.2 2D finite element model  | 96  |
| 5.3 Results  | 97  |
| 5.3.1 Potassium accumulation with leaky extracellular space  | 97  |
| 5.3.2 Potassium accumulation with no leak into extracellular space   | 97  |
| 5.3.3 Effect of potassium accumulation during Ach stimulation  | 98  |
| 5.3.4 Effect of potassium accumulation on pre stimulated arteries  | 99  |
| 5.3.5 Gap junction coupling vs. potassium accumulation   | 100 |
| 5.4 Discussion   | 103 |
| 5.4.1 Accumulation of potassium  | 103 |
| 5.4.2 Role of myoendothelial gap junctions   | 104 |
| 5.4.3 Effect of potassium accumulation   | 104 |
| 5.5 Limitations  | 106 |
| 5.6 Conclusion   | 107 |
| <br>   |     |
| Chapter 6: Summary and future work   | 108 |
| 6.1 Summary  | 108 |
| 6.1.1 Conducted responses  | 108 |
| 6.1.2 Myoendothelial projections   | 109 |



|   |     |
|---|-----|
| 6.1.3 Endothelium derived hyperpolarizing factor                            | 110 |
| 6.1.4 Compartmental methods vs. Finite element methods                      | 112 |
| 6.2 Future work   | 113 |
| 6.2.1 Calcium induced calcium release in IP <sub>3</sub> receptor           | 113 |
| 6.2.2 Calcium oscillations and waves in endothelial and smooth muscle cells | 116 |
| APPENDICES  | 136 |
| VITA  | 152 |

## LIST OF FIGURES

| FIGURE   | PAGE |
|--|------|
| Figure 1.1 Schematic showing EC and SMC in a blood vessel.....   | 2    |
| Figure 1.2: Schematics diagram of SMC model [56] .....   | 12   |
| Figure 1.3 Schematic diagram of EC model components and their interactions [78] .....  | 15   |
| Figure 2.1 Schematic of some identified endothelium derived pathways (Figure adapted from[105]).....   | 18   |
| Figure 2.2 Schematic diagram of two cells, n and m, connected by gap junctions permeable to ionic species S, generating intercellular current proportional to electrochemical gradient. ....   | 21   |
| Figure 2.3 Schematic diagram of EC SMC model [127]. The cells are coupled by gap junctions and NO coupling. ....   | 24   |
| Figure 3.1 Schematic diagram of the EC and SMC models. Cells are coupled by nitric oxide (NO) and myoendothelial gap junctions permeable to $Ca^{2+}$ , $Na^+$ , $K^+$ , and $Cl^-$ ions, and $IP_3$ .....   | 30   |
| Figure 3.2 Arrangement of ECs and SMCs in the vessel model. Fifteen SMCs overlap each EC, and fifteen ECs overlap each SMC. A serial arrangement of ECs with regular end-to-end couplings is assumed (shown in the right side of the vessel) as equivalent to the overlapping arrangement (shown in the left side). Circumferential symmetry allows us to consider only one SMC and one EC at each discrete position along the vessel. The whole vessel segment is 3 mm long, spanning 30 ECs and 450 SMCs in the axial direction..... | 31   |
| Figure 3.3 The electrical analogue of the vessel model. Gradients in the circumferential direction are negligible and each cell is connected with its neighbors on the same layer and with the overlapping cells on the adjacent layer. Fifteen identical ECs are assumed and the effect of ECs on neighboring SMCs is included by multiplying myoendothelial fluxes into a SMC by fifteen times (i.e. resistance decreases 15-fold). ....   | 32   |
| Figure 3.4 The effect of myoendothelial gap junction resistance on EC (squares) and SMC (circles) $V_m$ in the 3 mm long vessel at rest and at $t = 3$ s, after injection of a hyperpolarizing current (-150 pA per EC, for 3 s) into the ECs located at $x = 0$ . Simulations are shown for a low = 70 M $\Omega$ (A), an intermediate = 525 M $\Omega$ (B) and high = 13.5 G $\Omega$ (C).....   | 39   |
| Figure 3.5 EC (squares) and SMC (circles) $V_m$ in the 3 mm long vessel at rest and at $t = 3$ s, after injection of a depolarizing current. 15x150 pA were injected for 3 s into either a single SMC (A, C, E) or to 15 SMCs (B, D, F). Simulations are shown for a low = 70 M $\Omega$ (A, B), an intermediate = 525 M $\Omega$ (C, D) and a high =13.5 G $\Omega$ (E, F). ....  | 40   |
| Figure 3.6. EC (squares) and SMC (circles) $V_m$ in the 3 mm long vessel at rest and at $t = 6$ s, after local NE application. SMCs are stimulated for 6 s with a saturating concentration of NE (10 $\mu$ M). (A) Three adjacent cells are stimulated and a strong myoendothelial coupling is assumed (   |      |

$R_{gj}^{EC-SMC} = 70 \text{ M}\Omega$ ). (B) Three SMCs are stimulated and a weak myoendothelial coupling is assumed ( $R_{gj}^{EC-SMC} = 13.5 \text{ G}\Omega$ ). (C) Nine SMCs are stimulated and a strong myoendothelial coupling is assumed ( $R_{gj}^{EC-SMC} = 70 \text{ M}\Omega$ ). (D) Nine SMCs are stimulated and a weak myoendothelial coupling is assumed ( $R_{gj}^{EC-SMC} = 13.5 \text{ G}\Omega$ ). The same agonist stimulus has a significantly larger effect at the local site if the SM is poorly coupled to the endothelium. .... 42

Figure 3.7. Model responses to local Ach stimulation in a vessel prestimulated with 200 nM of NE and with  $R_{gj}^{EC-SMC} = 525 \text{ M}\Omega$ . From time  $t = 2 \text{ s}$ , the ECs at position  $x = 0$  are continuously stimulated with Ach ( $QIP_{3,ss} = 0.55 \text{ nM/ms}$ ). (A) Endothelial  $[Ca^{2+}]_i$  as a function of time and distance from stimulus site. (B) Endothelial  $V_m$  as a function of time and distance from stimulus site. (C) Smooth muscle  $[Ca^{2+}]_i$  as a function of time and distance from stimulus site. (D) Smooth muscle  $V_m$  as a function of time and distance from stimulus site. .... 44

Figure 3.8. (A) Predicted changes in SM  $[Ca^{2+}]_i$  during local Ach application in a vessel prestimulated with NE. 100 % change indicates a reduction in  $[Ca^{2+}]_i$  to the resting value prior to NE application. The Figure shows simulations with (dotted line) and without (solid line) contribution from the NO, and after inhibition of endothelial  $IP_3$  diffusion ( $p_{IP_3}^{EC-EC} = 0$ ). (B) Normalized steady-state endothelial  $Ca^{2+}$  profiles during local stimulation with Ach. Under control conditions (solid line), the  $Ca^{2+}$  spread was limited to  $\sim 300 \mu\text{m}$  (three ECs). Inhibition of axial  $IP_3$  diffusion ( $p_{IP_3}^{EC-EC} = 0$ ) practically abolished the  $Ca^{2+}$  spread. One hundred-fold greater permeability of the endothelial gap junctions to  $Ca^{2+}$  extended  $Ca^{2+}$  spread to  $< 400 \mu\text{m}$ . .... 46

Figure 3.9. Endothelial  $Ca^{2+}$  electrodiffusion during local Ach stimulation.  $IP_3$  release rate is increased in the fifth EC simulating local Ach stimulation. (A) Endothelial  $[Ca^{2+}]_i$  profile is shown as a function of the number of cells from the inlet of the vessel. (B) Predicted hyperpolarization following stimulation (stars) is presented next to experimental data from [138] (circles). (C) Intercellular  $Ca^{2+}$  current presenting  $Ca^{2+}$  flux between neighboring ECs. Positive values denote  $Ca^{2+}$  flow from the left to the right. Insert shows data at 100-fold higher resolution. Small  $Ca^{2+}$  fluxes towards the stimulation site appear after the tenth EC. .... 47

Figure 3.10 (A) The length constant ( $\lambda_{Ca}$ ) of  $Ca^{2+}$  decrease from the site of local Ach stimulation is shown for different levels of NE prestimulation. Ach stimulus strength was either held constant ( $QIP_{3,ss} = 0.33 \text{ nM ms}^{-1}$ ) (solid line) or was adjusted to produce the same local  $Ca^{2+}$  response at each prestimulation level (dashed line). (B) The length constant of  $V_m$  attenuation ( $\lambda_{el,Ach}$ ) is shown for vessel prestimulation with different NE concentrations. Ach stimulus strength was held constant ( $QIP_{3,ss} = 0.33 \text{ nM ms}^{-1}$ ) and simulations were repeated for a weak ( $R_{gj}^{EC-SMC} = 13.5 \text{ G}\Omega$ ) or a strong ( $R_{gj}^{EC-SMC} = 70 \text{ M}\Omega$ ) myoendothelial coupling. NE prestimulation increases the EC  $Ca^{2+}$  spread but reduces  $V_m$  spread. .... 49

Figure 4.1: Figure shows experimental characterization and related hypothesis for the functional presence of MPs. Immunohistochemical labeling study results in rat mesenteric artery showing localization of A)  $IK_{Ca}$ , B)  $IP_3R$  channels on the projection [118] and C) electron microscopy images of the projection in rat saphenous arteries [84]. D) Hypothesis based on experimental findings suggesting a role for  $IP_3$  entering the projection during SMC stimulation. .... 65

|  |    |
|--|----|
| Figure 4.2 a) Model schematic showing all the channels and pumps incorporated in the EC MP compartmental model. b) Schematic showing the dimensions of the EC microprojections (MP). Blue double sided arrows represent areas of diffusion between the MP and bulk EC compartment. ....  | 67 |
| Figure 4.3 2D FEM. a) shows the model geometry with SMC, EC as rectangular segments with a microprojection whose shape is imported from EM Figure by Sandow et al. Ion channel currents are uniformly distributed along the top and bottom boundaries of each cell. b) shows the EC projection with finite element mesh. $IK_{Ca}$ channels and $IP_3Rs$ are localized in the microprojection. ....  | 72 |
| Figure 4.4 Compartmental model results showing $Ca^{2+}$ (red lines) and $IP_3$ (blue lines) concentration in the EC microprojection (solid lines) and EC bulk (dashed lines) during $1\mu M$ NE stimulation of SMC (a) at 150s and Ach stimulation of EC (b) at 150s. MEGJ resistance is maintained as $900 M\Omega$ with restricted diffusion between the projection and bulk EC. 10% of $IP_3R$ receptors are concentrated in the MP compartment. $Ca^{2+}$ transients in the EC microprojection during NE stimulation is almost 4 times that of the EC bulk during Ach stimulation. .... | 74 |
| Figure 4.5 2D FEM model results for NE (a,c) and Ach stimulation(b,d) of the SMC and EC respectively. Colour bar shows the concentration of $Ca^{2+}$ and $IP_3$ in nM. Figure shows predicted $Ca^{2+}$ concentration inside the MP after NE stimulation of SMC (a) bulk EC stimulation with Ach (b). c and d show the predicted $IP_3$ transients in the MP for SMC and EC stimulation respectively. $Ca^{2+}$ and $IP_3$ concentration profiles are shown at time 7.5s after $1\mu M$ NE stimulation of SMC and Ach stimulation of EC at 2s respectively. ....                            | 75 |
| Figure 4.6 Predicted $Ca^{2+}$ concentration inside the MP after NE stimulation of SMC under control volume (a,b) and a 5 times smaller volume (c,d) for different MP shapes. Color bar shows the $Ca^{2+}$ concentration in nM. Inset in 5b shows the experimental electron microscopy image of the projection by Herberlin et al. [113]. ....  | 76 |
| Figure 4.7 Predicted global spread of the $Ca^{2+}$ gradients in the EC bulk after NE stimulation of SMC. ....   | 77 |
| Figure 4.8 SMC $V_m$ (a) and EC microprojection $Ca^{2+}$ (b) under three scenarios: No MP (dashed lines), control (solid line) and No MP with MEGJ resistance = $9 M\Omega$ and $IP_3R$ increased $10^3$ fold (dotted lines) ....   | 78 |
| Figure 4.9 2D FEM results shows $Ca^{2+}$ transients in the MP under control conditions (a) and with $IP_3$ diffusion across GJ blocked (b) for different MEGJ resistances after NE stimulation of SMC at 2s. Control MEGJ resistance is $900 M\Omega$ . ....  | 79 |
| Figure 4.10 Compartmental model results showing a) SMC $V_m$ and b) $Ca^{2+}$ concentration in the EC microprojection after stimulation with $1\mu M$ NE at 150 s under different $IK_{Ca}$ distribution in EC. ....   | 80 |

|   |     |
|---|-----|
| Figure 4.11 $\text{Ca}^{2+}$ transients in the SMC (b) and the corresponding changes in SMC $V_m$ (a) after SMC stimulation with $1\mu\text{M}$ NE at 150s for different myoendothelial gap junction resistances. (c) and (d) show the cumulative feedback with respect to SMC $V_m$ and SMC $\text{Ca}^{2+}$ .....   | 84  |
| Figure 4.12 SMC $V_m$ (a) and SMC $\text{Ca}^{2+}$ transients (b) for different $\text{IP}_3\text{R}$ density inside the projection. Cumulative feedback in the form of SMC $V_m$ (c) and SMC $\text{Ca}^{2+}$ (d) is as shown.....   | 85  |
| Figure 5.1 $\text{NaK}_{\alpha 2}$ is defined over the lower boundaries of SMC facing the extracellular space where $\text{K}^+$ can accumulate.....  | 97  |
| Figure 5.2 Extracellular $\text{K}^+$ (mM) accumulation during a) Ach stimulation of EC and b) NE stimulation of the SMC.....   | 98  |
| Figure 5.3 $\text{K}^+$ accumulation (mM)(color bar) in the extracellular spaces during Ach stimulation with no leak into space beyond the EC and SMC area with a) localized $\text{IK}_{\text{Ca}}$ channels on the MP and b) uniform $\text{IK}_{\text{Ca}}$ channels distribution across whole EC.....   | 98  |
| Figure 5.4 Extracellular $\text{K}^+$ (a), Nernst potential of $\text{K}^+$ (b), $\text{IK}_{\text{Ca}}$ current (c) and $V_m$ (d) for uniform $\text{IK}_{\text{Ca}}$ channels with extracellular leak (dashed), localized $\text{IK}_{\text{Ca}}$ with extracellular leak(solid) and localized $\text{IK}_{\text{Ca}}$ with no leak(dotted) during Ach stimulation of EC in the 2D FEM.....   | 100 |
| Figure 5.5 SMC $V_m$ (a) , and extracellular $\text{K}^+$ accumulation (b) for Ach stimulation of EC in prestimulated SMC for control (solid lines), No $\text{K}^+$ accumulation (dash-dot lines), High $\text{K}^+$ accumulation (less leaky extracellular)(dotted lines) and control with 50% $\text{NaK}_{\alpha 2}$ current (dashed lines). Summary of change in SMC $V_m$ (c) and SMC $\text{Ca}^{2+}$ (d) after stimulation of EC with Ach is presented for different values of extracellular $\text{K}^+$ .....   | 101 |
| Figure 5.6 SMC $V_m$ (a) and SMC $\text{Ca}^{2+}$ (b) for Ach stimulation of EC in prestimulated SMC (d-f) for control (solid lines), MEGJ blocked (dotted lines), MEGJ blocked 50% $\text{NaK}_{\alpha 2}$ current (dashed lines) and MEGJ coupling with 90% $\text{NaK}_{\alpha 2}$ current (dash-dot lines).....   | 102 |
| Figure 6.1 $\text{IP}_3\text{R}$ inactivation probability ( $P_i, \text{IP}_3\text{R}$ ) model fit (solid line) as a function of $[\text{Ca}^{2+}]_i$ to experimental data (circles) from porcine aortic ECs [207].....   | 114 |
| Figure 6.2 : Predicted open probability for $\text{IP}_3\text{R}$ with the inclusion of $\text{Ca}^{2+}$ dependent activation [70]. The data for $2\mu\text{M}$ $\text{IP}_3\text{R}$ is taken from Bezprozvanny et al [208]. .....   | 114 |
| Figure 6.3 a) and b) show $\text{Ca}^{2+}$ mediated (or $\text{Ca}^{2+}$ diffusion from SMC to EC blocked, blue dotted), $\text{IP}_3$ mediated (or $\text{IP}_3$ diffusion from SMC to EC blocked, red solid), both $\text{Ca}^{2+}$ and $\text{IP}_3$ mediated (or both $\text{IP}_3$ and $\text{Ca}^{2+}$ from SMC to EC blocked, green dashed) and $\text{IP}_3\text{R}$ mediated (or $\text{IP}_3\text{R}$ blocked, orange dash-dot) feedback for $\text{K}_{\text{dact}}$ of 130 nM and 350nM respectively. Figure c and d show the respective SMC $\text{Ca}^{2+}$ feedback..... | 115 |
| Figure 6.4 $\text{Ca}^{2+}$ oscillations in the EC compartmental model after incorporation of CICR in the $\text{IP}_3\text{R}$ .....   | 116 |
| Figure 6.5 Intracellular $\text{Ca}^{2+}$ propagation in EC compartmental model.....  | 117 |

Figure A2.1: a) difference in area and thickness of MP with respect to the bulk EC, b) boundaries in the finite element model where discontinuity is applied. .... 149

## LIST OF TABLES

| TABLE   | PAGE |
|---|------|
| Table 3.1 Cell dimensions and the population ratios of ECs to SMCs in various tissues and computational models .....  | 30   |
| Table 3.2 Gap junction resistances .....  | 35   |
| Table 3.3. Predicted electrical length constant, $\lambda_{el}$ (mm).....   | 41   |
| Table 4.1: List of parameters describing dimensions of MPs and microdomains along with values of diffusion constants of ions and $IP_3$ in the cytosol..... | 71   |
| Table 5.1: List of parameters changed from the EC-SMC model .....   | 96   |

## LIST OF ACRONYMS

|                  |  |
|------------------|--|
| EC               | Endothelial cell   |
| SMC              | Smooth muscle cell   |
| Ca <sup>2+</sup> | Calcium ion  |
| K <sup>+</sup>   | Potassium  |
| Na <sup>+</sup>  | Sodium   |
| Cl <sup>-</sup>  | Chloride   |
| SR               | Sarcoplasmic reticulum                                       |
| ER               | Endoplasmic reticulum  |
| NE               | Norepinephrine   |
| PE               | Phenylephrine  |
| Ach              | Acetylcholine  |
| RyR              | Ryanodine receptors  |
| CICR             | Calcium induced calcium release                              |
| VGCC             | Voltage gated calcium channels                               |
| ANGII            | Angiotensin II   |
| SK <sub>Ca</sub> | Small conductance calcium activated potassium channel        |
| IK <sub>Ca</sub> | Intermediate conductance calcium activated potassium channel |
| BK <sub>Ca</sub> | Large conductance calcium activated potassium channel        |
| NO               | Nitric oxide   |
| cGMP             | Cyclic guanosine monophosphate                               |
| NaK              | Sodium-potassium ATPase pump                                 |
| NCX              | Sodium-calcium exchanger                                     |



|                   |  |
|-------------------|--|
| KCl               | Potassium chloride                             |
| IP <sub>3</sub>   | Inositol (1,4,5)-trisphosphate                 |
| DAG               | Diacylglycerol                                 |
| PIP <sub>2</sub>  | Phosphatidylinositol-4-5-biphosphate           |
| ADP               | Adenosine di phosphate                         |
| cADPR             | cyclic ADP ribose                              |
| NAADP             | Nicotinic acid dinucleotide phosphate          |
| PMCa              | Plasma membrane Ca <sup>2+</sup> ATPase        |
| SOC               | Store operated Ca <sup>2+</sup> channels       |
| IP <sub>3</sub> R | IP <sub>3</sub> receptor                       |
| PKC               | Protein kinase C                               |
| SERCA             | Sarcoplasmic reticulum Ca <sup>2+</sup> ATPase |
| NSC               | Non-selective cation channels                  |
| K <sub>ir</sub>   | Inward rectifying potassium channels           |
| CQSN              | Calsequestrin                                  |
| K <sub>v</sub>    | Voltage gated potassium channels               |
| V <sub>m</sub>    | membrane potential                             |
| VRAC              | Volume regulated anion channels                |
| CaCC              | Calcium-activated Cl <sup>-</sup> channels     |
| sGC               | Soluble guanylate cyclase                      |
| Cx                | Connexin                                       |
| MEGJ              | Myoendothelial gap junction                    |
| R <sub>gj</sub>   | Gap junction resistance                        |

|                               |  |
|-------------------------------|--|
| NOS                           | Nitric oxide synthase                      |
| MLCK                          | Myosin light chain kinase                  |
| COX                           | Cyclooxygenase                             |
| AA                            | Arachidonic acid                           |
| PGI <sub>2</sub>              | Prostacyclin                               |
| PGH <sub>2</sub>              | Prostaglandin                              |
| cAMP                          | Cyclic adenosine monophosphate             |
| MP                            | Myoendothelial projections                 |
| MD                            | Microdomain                                |
| FEM                           | Finite element method                      |
| EDHF                          | Endothelium derived hyperpolarizing factor |
| EDRF                          | Endothelium derived relaxing factor        |
| GHK                           | Goldman-Hodgkin-Katz                       |
| CNP                           | C-type natriuretic peptide                 |
| CO                            | Carbon monoxide                            |
| H <sub>2</sub> O <sub>2</sub> | Hydrogen peroxide                          |
| EET                           | Epoxyeicosatrienoic acids                  |
| IEL                           | Internal elastic lamina                    |

## LIST OF SYMBOLS

|                |                          |
|----------------|--------------------------|
| mM             | millimolar               |
| nM             | nanomolar                |
| $\Omega$       | Ohm                      |
| $\lambda$      | Length constant          |
| $\Delta$       | change/difference        |
| $\mu\text{M}$  | micromolar               |
| $\mu\text{m}$  | micrometer               |
| [X]            | concentration of X       |
| mV             | millivolt                |
| pA             | picoampere               |
| $\tau$         | time constant            |
| R              | Universal gas constant   |
| T              | temperature              |
| F              | Faraday constant         |
| $z_X$          | charge of ion X          |
| ms             | millisecond              |
| $K_d$          | Half activation constant |
| $[\text{X}]^n$ | n = Hill coefficient     |
| cm             | centimeter               |
| s              | second                   |

## **Chapter 1. Introduction**

### **1.1 Motivation**

Hypertension or high blood pressure is a serious condition that affects one in every three Americans. It can lead to many life threatening diseases such as to coronary heart disease, heart failure, stroke, kidney failure among others [1]. Hypertension was directly responsible for approximately 24000 deaths in 2008 in the United States. The blood pressure in the body is mainly determined by the cardiac output and the total peripheral resistance. The total peripheral resistance in turn depends on the diameters of arteries in the systemic circulation [2].

Microcirculation is the region of the vasculature where small vessels (diameter <300  $\mu\text{m}$ ) are located. It is the site of generation of maximum resistance to systemic circulation. The functional state of the microcirculation is one of the main determinants of whole system blood pressure [2]. Myogenic tone is a highly critical feature of small arteries because it determines peripheral vascular resistance and blood pressure. Small arteries in the microvasculature are in a state of partial contraction due to the transmural pressure applied by luminal flow of blood. They can be dilated or constricted by external agonists or agonists flowing in the blood such as acetylcholine (Ach), norepinephrine (NE), phenylephrine (PE), endothelin among others. The two main constituents of the microcirculation: endothelial cells (ECs) and smooth muscle cells (SMCs) are in constant bidirectional communication both in radial as well as axial directions (Figure 1.1). Substantial amount of experimental efforts have been directed towards the exploration of microcirculatory pathways and its importance is now well appreciated.

Unfortunately, theoretical modeling of microcirculatory pathways has not received similar attention. Mathematical modeling offers a systematic approach to the analysis of these mechanisms and can serve as a tool for data interpretation and for guiding new experimental studies. Currently, advanced models describing  $\text{Ca}^{2+}$  dynamics exist in other systems such as cardiac myocytes [3-7]. Often these models are integrated with descriptions for membrane electrophysiology, cell mechanics, metabolic and signal-transduction pathways and multicellular/multiscale models have emerged for the heart [8-13]. These models are capable of describing function at the tissue level while integrating mechanisms at the subcellular/molecular level and have been utilized to investigate physiological function as well as disease states [14-17]. Although  $\text{Ca}^{2+}$  signaling in different cells shares certain qualitative aspects, there are vast differences in  $\text{Ca}^{2+}$  mobilization between cardiac and vascular cells [18-23]. Recently, similar attempts have begun for modeling of  $\text{Ca}^{2+}$  dynamics in vascular cells in single as well as multicellular models. Advancement of these models is necessary to achieve the level of sophistication analogous to cardiac models. These models will contribute towards the development of a theoretical framework for the understanding of microcirculatory phenomena.

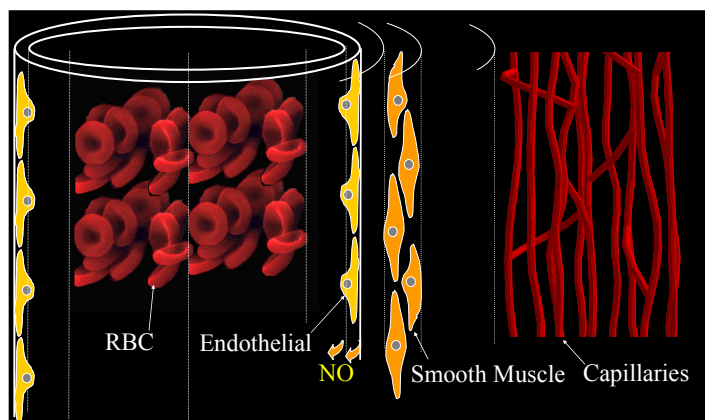


Figure 1.1 Schematic showing EC and SMC in a blood vessel

## 1.2 Background

$\text{Ca}^{2+}$  is a universal signaling molecule with a central role in a number of vascular functions including in the regulation of tone and blood flow.  $\text{Ca}^{2+}$  homeostasis in the cells is maintained by a host of different ion channels and pumps. The expression and density of the various membrane channel components differ among tissues, species and even size of arteries in the same microcirculatory bed. The mesenteric microcirculation is one of the good models of resistance arteries with dense innervations and easy accessibility [24]. It is also one of the most thoroughly studied vascular beds with vast amount of experimental data available. Therefore, in most of our models we use data from small rat mesenteric arteries (RMAs). This section describes the major channels and pumps present on SMCs and ECs and some of the major agonist induced pathways present in RMAs.

### A) Regulation of $\text{Ca}^{2+}$ in SMC

Cytosolic concentration of  $\text{Ca}^{2+}$  controls the level of constriction in SMCs. An elaborate signaling network exists that regulates  $\text{Ca}^{2+}$  concentrations in the vascular wall [25]. These pathways include intracellular as well as inter cellular signaling by paracrine factors or diffusion of ions through homo or hetero cellular gap junctions.  $\text{Ca}^{2+}$  concentration in the SMCs can be increased by influx of extracellular  $\text{Ca}^{2+}$  through calcium channels existing on the plasma membrane or via intracellular  $\text{Ca}^{2+}$  stores sarcoplasmic reticulum (SR). The  $\text{Ca}^{2+}$  entering from the extracellular space can induce further  $\text{Ca}^{2+}$  influx from the intracellular stores by activation of ryanodine receptors (RyRs). This phenomenon is also termed as calcium induced calcium release (CICR) [26, 27]. Potassium channels present on the plasma membrane are capable of hyperpolarizing the SMC membrane leading to the closure of voltage gated calcium channels (VGCC)

thus reducing the  $\text{Ca}^{2+}$  concentration in the SMC. Other channels, pumps and exchangers present in rat mesenteric arteriole which influence  $\text{Ca}^{2+}$  signaling are described below.

### **1.2.1 Potassium channels:**

Ion channels are transmembrane proteins which allow the transport selective transport of ionic species across the membrane. Potassium channels are the most diverse type of channels occurring over the SMC membrane and potassium ion are the largest current carries inside the cell. They play a crucial role in maintaining the potential of the membrane and smooth muscle dilation. Potassium channels can be largely classified into the following two types:

#### a.) Voltage gated potassium channels

In the SMC, the outward potassium current flowing through the voltage activated potassium channels ( $\text{K}_v$ ) is an important component of membrane potential ( $V_m$ ) of the cell and can be divided into two types based on its inactivation mechanism the delayed rectifier current and rapidly inactivating transient outward current. Depending on the type of species or the type of tissue being studies, the SMC can express one or both of these channels types[28]. These channels are activated by depolarization of the  $V_m$  which can be caused due to increase in intraluminal pressure or neurotransmitters such as NE, endothelin, angiotensin II (ANG II) etc. This allows restoration of the  $V_m$  after depolarization and avoids excessive constriction of the vessel.

#### b.) Calcium activated potassium channels

This family of  $\text{Ca}^{2+}$  activated potassium channels constitutes of three types of channels differentiated on the basis of their conductances ie: small ( $\text{SK}_{\text{Ca}}$ ), intermediate ( $\text{IK}_{\text{Ca}}$ ) and large ( $\text{BK}_{\text{Ca}}$ ) conductance calcium activated potassium channels. The SMCs

express only the  $BK_{Ca}$  channels while the  $SK_{Ca}$  and  $IK_{Ca}$  channels are found on the EC membrane.  $BK_{Ca}$  channels are activated by both depolarizing voltage and increase in  $Ca^{2+}$  concentration [29].  $BK_{Ca}$  can also be activated by nitric oxide (NO) directly through cyclic guanosine monophosphate (cGMP) [30]. They play an important role in limiting  $Ca^{2+}$  entry into the cell.

### 1.2.2 Sodium–potassium pumps

A sodium-potassium pump also called  $Na^+/K^+$ ATPase (NaK) is a ubiquitous feature of the membrane of almost every species. Every cell expresses hundreds or even a million NaK.  $Na^+/K^+$ ATPase pump extrudes three sodium ions out of the cell for two potassium ions into the cell against their concentration gradient by phosphorylation of adenosine tri phosphate (ATP) stored in the cell. Its action is dependent on the internal and extracellular concentrations of  $Na^+$  and  $K^+$  respectively [31]. This action is necessary to maintain the sodium potassium gradient across the membrane which is necessary to drive many co and counter transporters for intake of glucose from blood, regulation of cell volume, pH balance and  $Ca^{2+}$  homeostasis.  $Na^+/K^+$ ATPase pump comprises of a non-covalently linked  $\alpha$  subunit ( $\alpha 1$  to  $\alpha 4$ ) and a glycosilated  $\beta$  subunit ( $\beta 1$  to  $\beta 3$ ). Four isoforms  $\alpha$  subunit ( $\alpha 1$  to  $\alpha 4$ ) of the alpha subunit and three isoforms of  $\beta$  subunit ( $\beta 1$  to  $\beta 3$ ) are known to exist in cells. The occurrence and ratio of distribution of each isoform differs between different species and even different vascular beds [32]. The  $\alpha 1$  isoform of the  $Na^+/K^+$ ATPase is the most common and widely expressed of all the others in both SMC and EC. This isoform is almost completely activated at physiological extracellular concentrations of potassium (5mM). However, recent studies done with rat mesenteric arterioles have found that  $\alpha 2$  and  $\alpha 3$  isoforms are present in specialized domains in the



SMC which are activated by potassium in the concentration ranges of 3-15 mM and are sensitive to inhibitory action of ouabain. [33, 34]

### **1.2.3 Sodium-calcium exchanger**

Sodium- calcium or  $\text{Na}^+ / \text{Ca}^{2+}$  exchangers (NCX) are expressed in the plasma membranes of SMC which regulate intracellular  $\text{Ca}^{2+}$ . NCX is a bidirectional electrogenic ion transporter which couples the transport of 3  $\text{Na}^+$  ions inside the cell in exchange of transporting two  $\text{Ca}^{2+}$  ions outside of the cell. The NCX is driven by the energy of the sodium ( $\text{Na}^+$ ) electrochemical gradient which exists in cells in the event of  $\text{Na}^+ / \text{Ca}^{2+}$  blockade, the  $\text{Na}^+$  concentration increases inside the cell which reverses the direction of NCX thereby resulting in translocation of  $\text{Na}^+$  outside the cell and  $\text{Ca}^{2+}$  inside the cell causing  $\text{Ca}^{2+}$  concentration to increase. NCX is important for three major actions. Firstly, it plays a major role in net  $\text{Ca}^{2+}$  removal from the cytoplasm during cell activation and restores normal  $\text{Ca}^{2+}$  concentrations. In reverse mode, it mediates  $\text{Ca}^{2+}$  entry during cell activation and depolarisation. It plays a minor role in modulating resting concentrations of  $\text{Ca}^{2+}$ , the majority of which is regulated by low capacity high affinity adenosine triphosphate (ATP) driven  $\text{Ca}^{2+}$  pump [35, 36].

### **1.2.4 Calcium channels on plasma membrane**

#### a.) Voltage operated $\text{Ca}^{2+}$ channels

Vascular SMCs contain voltage gated  $\text{Ca}^{2+}$  channels (VGCC) which are further differentiated as L-type and T-type channels depending on their gating time constants. VGCCs are the main route of  $\text{Ca}^{2+}$  entry into the cell [25, 37]. SMCs in rat are known to possess mostly L-type VGCC's. Depolarization of SMC increase the open probability of

VGCC. Vasoactive agents like potassium chloride (KCl) cause an increase in SMC  $\text{Ca}^{2+}$  by activating VGCCs. VGCCs can be directly activated by stretching of the vessel [25].

#### b.) Receptor activated $\text{Ca}^{2+}$ channels

Ion channels protein which opens upon binding of an external ligand as known as receptor activated channels. These channels open to allow influx of  $\text{Ca}^{2+}$  into the cell [25]. The cell surface receptors are made of G-protein linked receptors and receptor tyrosine kinase. Some important agonists known to activate these cells include transmitters like Ach, ATP, NE, glutamate etc. Stimulation by these agonists causes generation of inositol (1,4,5)-trisphosphate ( $\text{IP}_3$ ) and DAG by hydrolysis of phosphatidylinositol-4-5-bisphosphate ( $\text{PIP}_2$ ) by phospholipase C (PLC) enzymes (PLC  $\beta$  and PLC  $\gamma$ ), cyclic ADP ribose (cADPR) and nicotinic acid dinucleotide phosphate (NAADP). The molecules generated downstream of these reactions also cause release of  $\text{Ca}^{2+}$  from intracellular stores by activation of  $\text{IP}_3$  receptors on the SR.

#### c.) Plasma membrane $\text{Ca}^{2+}$ ATPase

$\text{Ca}^{2+}$  adenosine triphosphatase (PMCA) pumps are present on SMC plasma membrane. These pumps remove intracellular  $\text{Ca}^{2+}$  by active transport [25, 37]. PMCA mediates sustained release of  $\text{Ca}^{2+}$  from the cell unlike NCX which cause acute removal of intracellular  $\text{Ca}^{2+}$ . PMCA is formed of two domains, an ATP binding domain in the cytoplasm and a  $\text{Ca}^{2+}$  binding domain which traverses the cell membrane. Phosphorylation of aspartate residue (Asp351) by terminal phosphate ATP causes a conformational change in both the domains which leads to the transport of  $\text{Ca}^{2+}$  outside the cell. Release of  $\text{Ca}^{2+}$  outside the cell acts as a signal for hydrolysis of Asp351 phosphate group and returns the pump to its original state. PMCA pumps use the energy

derived from the hydrolysis of ATP to ADP to remove  $\text{Ca}^{2+}$  from the cytoplasm and induce relaxation in the SMCs. Four isoforms of PMCS are known to exist (PMCA 1, PMCA 2, PMCA 3, and PMCA 4) in the vasculature. Of these, PMCA 1 is the most abundantly found PMCA isoform on rat mesenteric arterioles [38].

#### d.) Store operated $\text{Ca}^{2+}$ channels

Depletion of intracellular stores as a result of agonist induced depolarization in SMCs via  $\text{IP}_3$  pathway result in opening of store operated  $\text{Ca}^{2+}$  channels (SOC) present on the cell membrane [39]. Increase in  $\text{Ca}^{2+}$  causes SMC contraction. As, the intracellular stores are depleted of the  $\text{Ca}^{2+}$ , a diffusible signal might be transmitted to the membrane which opens store operated channel leading  $\text{Ca}^{2+}$  influx exclusively to refill the SR.

### **1.2.5 Calcium channels in SR**

#### a.) Release through ryanodine receptors (RyR)

SR is the main intracellular source of  $\text{Ca}^{2+}$  in the cell. SR membrane of arterial SMC contains RyRs [40].  $\text{Ca}^{2+}$  is the main activator of RyRs. RyR regulation is modulated by cADPR which is generated by nicotinamide adeninedinucleotide (NAD). Increase in cytoplasmic  $\text{Ca}^{2+}$  which can result from activation of VGCC or receptor activated channels causes activation of RyR thus adding to intracellular  $\text{Ca}^{2+}$  by a release from the SR. This  $\text{Ca}^{2+}$  release causes transients in cytoplasmic  $\text{Ca}^{2+}$  also called  $\text{Ca}^{2+}$  sparks.

#### b.) Release through $\text{IP}_3$ receptors

Along with RyRs, the SR also contains  $\text{IP}_3$  receptors spread across its membrane [40]. Vasoactive agents like NE stimulate PLC pathway by stimulation of associated G proteins on the membrane. This leads to conversion of  $\text{PIP}_2$  into  $\text{IP}_3$  and diacylglycerol

(DAG).  $\text{Ca}^{2+}$  is the main effector of  $\text{IP}_3\text{Rs}$ . It has been shown that an increase in luminal SR  $\text{Ca}^{2+}$  increases  $\text{IP}_3\text{Rs}$  sensitivity thus opening the  $\text{IP}_3\text{R}$  channels. Dependence of  $\text{IP}_3\text{R}$  sensitivity on  $\text{Ca}^{2+}$  has seen conflicting reports. Low  $\text{Ca}^{2+}$  concentration (100-300nM) in the cytoplasm has a stimulatory effect on  $\text{IP}_3\text{Rs}$  while concentrations above 300nM become inhibitory for  $\text{IP}_3\text{Rs}$ . The relationship of  $\text{Ca}^{2+}$  concentration and  $\text{IP}_3\text{R}$  activation has been reported to be sigmoidal. The  $\text{Ca}^{2+}$  release from intracellular stores by opening of  $\text{IP}_3$  channels amplifies cytosolic  $\text{Ca}^{2+}$  leading to SMC contraction. The other product of the hydrolysis of  $\text{PIP}_2$  i.e. DAG activates protein kinase C (PKC). The activation of PKC causes persistence of  $\text{Ca}^{2+}$  dependent responses. Rapid hydrolysis of  $\text{IP}_3$  deactivates  $\text{IP}_3\text{R}$  and leads to termination of  $\text{Ca}^{2+}$  release from SR [25].

#### **1.2.6 Sarcoplasmic/ endoplasmic reticulum calcium pumps**

Sarcoplasmic/endoplasmic reticulum Ca ATPase pumps (SERCA pumps) are present on the SR membrane alongside of RyRs and  $\text{IP}_3\text{Rs}$ . These pumps sequester  $\text{Ca}^{2+}$  back into the SR and contribute towards decreasing the cytoplasmic concentration of  $\text{Ca}^{2+}$ . Similar to PMCA, SERCA pumps utilize energy derived from hydrolysis of ATP to ADP to transport  $\text{Ca}^{2+}$  into the SR [25, 41].

#### **1.2.7 Calcium buffering**

$\text{Ca}^{2+}$  buffering also plays an important role in  $\text{Ca}^{2+}$  regulation. SMC contraction primarily depends on availability of free  $\text{Ca}^{2+}$ . Almost 90% of  $\text{Ca}^{2+}$  inside the cell exists as a complex with different intracellular protein like calmodulin, calsequestrin (CQSN) and troponin and is reversibly converted to free  $\text{Ca}^{2+}$  [42]. The amplitude and duration of  $\text{Ca}^{2+}$  signal as well as spatial spreading of local  $\text{Ca}^{2+}$  depend largely on the extent of cytoplasmic  $\text{Ca}^{2+}$  buffering [25].

### 1.2.8 Theoretical modeling of vascular SMCs

Modeling of  $\text{Ca}^{2+}$  dynamics in SMCs has received more attention than in ECs. Early attempts include the generic models of Wong and Klassen [43, 44], the oscillatory model of Gonzalez-Fernandez and Ermentrout [45], the  $\text{IP}_3$ -dependent  $\text{Ca}^{2+}$  release model in A7r5 cells of Fink and coworkers [46] and the NE diffusion model of Bennett and coworkers [47]. The complexity of  $\text{Ca}^{2+}$  mobilization and the many components affecting membrane's electrical activity prompted Parthimos and coworkers [48] to develop a minimal model of a SMC. The reduced number of parameters made their model attractive for subsequent studies of vascular signaling [49-51]. Model simulations showed chaotic behavior in  $\text{Ca}^{2+}$  levels as a result of the nonlinear interaction between a membrane oscillator and an intracellular store  $\text{Ca}^{2+}$  oscillator. The model was able to reproduce behavior seen under various experimental conditions and pharmacological interventions [52, 53]. A different approach was followed by Yang and coworkers. Their aim was to develop a detailed model that will incorporate all the known significant components of the plasma membrane in SMCs for rat cerebrovascular arteries [54]. Their study presents perhaps the first attempt for a detailed, tissue-specific vascular model of  $\text{Ca}^{2+}$  dynamics. The ability of this study to simulate macro scale responses prompted the development of subsequent models that followed a similar, detailed, tissue-specific modeling approach with significant effort to obtain current descriptions based on electrophysiological recordings [55, 56]. These detailed models, combined, include descriptions for important transmembrane currents such as  $\text{VOCC}$ ,  $\text{K}_v$ ,  $\text{BK}_{\text{Ca}}$ ,  $\text{K}_{\text{ir}}$  channels, stress-activated NSC,  $\text{Cl}^-$  channels,  $\text{Na}^+$ - $\text{Ca}^{2+}$  exchanger,  $\text{Na}^+$ - $\text{K}^+$ -ATPase, and  $\text{Ca}^{2+}$ -ATPase pumps. Descriptions for  $\text{Ca}^{2+}$ ,  $\text{Na}^+$ ,  $\text{Cl}^-$ ,  $\text{K}^+$ , and  $\text{IP}_3$  balance have been

presented.  $IP_3$  and  $Ca^{2+}$  sensitive intracellular stores have also been implemented that exhibit CICR, and  $Ca^{2+}$  sequestrations through SERCA (Figure 1.2). Descriptions for the  $\alpha_1$ -adrenoceptor and nitric oxide (NO)/cGMP signaling pathways have been utilized as well as formulations for the DAG-dependence of NSC activation as a mechanism for sustained cell depolarization following adrenoceptor stimulation [56, 57]. The  $Ca^{2+}$  models have been integrated with biomechanics models capable of simulating diameter responses to  $Ca^{2+}$  mobilization [58, 59]. In one of the models [55], an intracellular subcompartment accounts for subcellular heterogeneity and the presence of subplasmalemmal microdomains. Elements from the minimal model of Parthimos [48] and the detailed approach of Yang [54] have been incorporated in a SMC model presented by Jacobsen and co-workers [51]. A significant feature of this model is that it abandons the compartmental approach of the previous modeling attempts and provides a description for cytosolic  $Ca^{2+}$  with spatial heterogeneity. This was accomplished by incorporating diffusion of  $Ca^{2+}$  within the cytosol in the longitudinal direction of the cell. Through this process, it has become obvious that detailed models of  $Ca^{2+}$  dynamics offer many advantages in investigations of  $Ca^{2+}$  signaling. These models, however, have to deal with significant obstacles/limitations in the form of considerable number of unknown parameters, the absence of tissue-specific quantitative data (particularly electrophysiological recordings for transmembrane currents), the structure and function of the intracellular stores and the spatial distribution of receptors, channels and pumps, to name a few. ECs and SMCs regulate  $Ca^{2+}$  entry and  $V_m$  by expressing an abundant and diverse collection of ion channels. In addition, considering the balance of the other major intracellular ionic species (i.e.,  $Na^+$ ,  $K^+$ ,  $Cl^-$ ) is essential to modeling both single-cell

electrophysiology and cell-to-cell electrochemical coupling and communication. Finally, the models need to integrate relevant signal transduction pathways. Consequently, there is still a need to build upon previous modeling work in order to develop cellular models that will assist in the investigations of vascular tone regulation in health and disease.

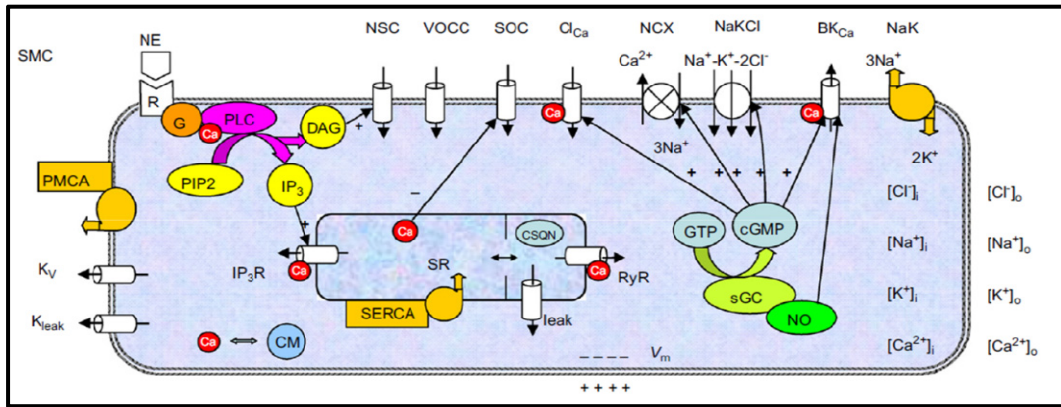


Figure 1.2: Schematics diagram of SMC model [56]

## B) $Ca^{2+}$ regulation in EC

Endothelial cells located at the interface of the blood and vessel wall. They play an important role in both normal tissue function and various pathological conditions [60, 61]. ECs perform a host of functions including immunological response regulation, blood coagulation, vessel repair, angiogenesis and vascular tone modulation [61]. Common endothelial responses to mechanical or chemical stimuli include release of physiological signal or alteration of surface molecule expression and adhesion, gene expression, cytoskeletal remodeling, cell growth and angiogenesis [21]. In EC, elevation of intracellular  $Ca^{2+}$  leads to production of vasoactive substances like prostanoids and nitric oxide (NO). NO is produced by the activation of endothelial NO synthases [21] which are activated by  $Ca^{2+}$ . When stimulated by an agonist, the initial increase in  $Ca^{2+}$  occurs by release from the opening of intracellular stores and the following plateau is maintained by

extracellular  $\text{Ca}^{2+}$  entry.  $\text{Ca}^{2+}$  store depletion and electrochemical driving force are the main regulators of  $\text{Ca}^{2+}$  entry from the extracellular medium. SOC, NSCC, NaKATPase pump and NCX are common to both SMC and EC plasma membrane. Among the  $\text{Ca}^{2+}$  activated potassium channels,  $\text{SK}_{\text{Ca}}$  and  $\text{IK}_{\text{Ca}}$  are expressed in the EC of rat mesenteric while the  $\text{BK}_{\text{Ca}}$  channels are only present in the SMC. Other channels specific to EC are described below.

### **1.2.9 Inward rectifier potassium channels**

Inward rectifier potassium channels ( $\text{K}_{\text{ir}}$ ) are sensitive to extracellular concentration of potassium in the range of 1 to 20 mM. These channels increase entry of potassium into the cell thereby hyperpolarizing of EC and subsequently the SMC. They are present in almost all endothelial cells and contribute towards the resting  $V_m$  of the EC. EC  $\text{K}_{\text{ir}}$  channels are known to be activated not only by potassium but also by shear stress.

### **1.2.10 Small and intermediate conductance calcium activated potassium channels**

RMA ECs express both small ( $\text{SK}_{\text{Ca}}$ ) and intermediate ( $\text{IK}_{\text{Ca}}$ ) conductance calcium activated potassium channels. The  $\text{K}_{\text{Ca}}$  channels are not constitutively opened  $\text{SK}_{\text{Ca}}$  channels have  $\text{Ca}^{2+}$  sensitivity in the concentration range of 0.0- 0.7  $\mu\text{M}$  and are virtually inactive at resting  $\text{Ca}_i$ .  $\text{KCa}$  channels are activated during EC stimulation (i.e., as  $[\text{Ca}^{2+}]_i$  rises) to induce hyperpolarization, essentially linking  $[\text{Ca}^{2+}]_i$  changes to  $V_m$  alterations [21, 62].  $\text{K}_{\text{Ca}}$  currents are considered to be both voltage and time independent [63, 64].  $\text{SK}_{\text{Ca}}$  channels can be blocked by toxins like apamin. The  $\text{IK}_{\text{Ca}}$  channel has conductances lying between  $\text{SK}_{\text{Ca}}$  and  $\text{BK}_{\text{Ca}}$  channels. These channels are insensitive to apamin but are blocked by toxins charybdotoxin, 1-[(2-chlorophenyl) diphenylmethyl]-



1H-pyrazole (Tram-34) and 2-(2-chlorophenyl)-2,2-diphenylacetonitrile (Tram-39) [65-67].

### 1.2.11 Theoretical modeling of vascular ECs

The first endothelial cell models were based on earlier generic models of  $\text{Ca}^{2+}$  dynamics in electrically non-excitable cells [68-71]. Early models started with simple descriptions of  $\text{Ca}^{2+}$  handling components and few transmembrane currents. Winston and coworkers [72] studied the effects of mechanical strain on cultured bovine pulmonary artery endothelial (BPAE) cells.  $\text{Ca}^{2+}$  dynamics and electrical activity of vascular ECs were first examined in a model introduced by Wong and Klassen [73, 74].

The first in-depth model of  $\text{Ca}^{2+}$  dynamics was presented by Wiesner and coworkers [75] for Human Umbilical Vein Endothelial Cells (HUVECS), and incorporated detailed thrombin receptor kinetics [76]. The model included most of the major  $\text{Ca}^{2+}$  mobilization pathways including CICR, CCE,  $\text{IP}_3\text{R}$  dependent store  $\text{Ca}^{2+}$  release, and  $\text{Ca}^{2+}$  buffering. The model described  $\text{IP}_3$  and  $\text{Ca}^{2+}$  dynamics and included separate mass balances for cytosolic, store and buffered  $\text{Ca}^{2+}$ . Schuster and coworkers [77] developed a model to simulate changes in membrane electrical activity following bradykinin stimulation of coronary artery ECs. Experimental data provided empirical correlations for the cytosolic  $\text{Ca}^{2+}$  and  $\text{IP}_3$  changes following stimulation. The focus of the model was to predict  $\text{K}^+$  currents and  $V_m$  changes in the presence and absence of extracellular  $\text{Ca}^{2+}$ . In a recent study, we presented a detailed EC model (Figure 1.3) that integrates both EC  $\text{Ca}^{2+}$  dynamics and plasmalemmal electrical activity to investigate EC responses to various stimulatory conditions and the relationship between  $\text{Ca}^{2+}$  and  $V_m$  [78]. The model describes most of the major membrane channels and pumps present in EC of rat

mesenteric arteries (RMA). The plasma membrane includes kinetic descriptions for NSC, SOC, SK<sub>Ca</sub> and IK<sub>Ca</sub>, K<sub>ir</sub>, volume regulated anion channels (VRAC), calcium-activated Cl<sup>-</sup> channels (CaCC), NCX and Na<sup>+</sup>-K<sup>+</sup>-Cl<sup>-</sup> cotransporter and Na<sup>+</sup>-K<sup>+</sup>-ATPase pump. It also includes intracellular Ca<sup>2+</sup> handling components such as IP<sub>3</sub> receptor, sarco/endoplasmic reticulum (ER), SERCA and plasma membrane Ca<sup>2+</sup>-ATPase (PMCA) pumps. For the first time, we integrated balances for the major ionic species (i.e. K<sup>+</sup>, Cl<sup>-</sup>, Na<sup>+</sup>) in addition to the balances for cytosolic, store and buffered Ca<sup>2+</sup> and IP<sub>3</sub> and the Hodgkin-Huxley type formalism for the V<sub>m</sub>.

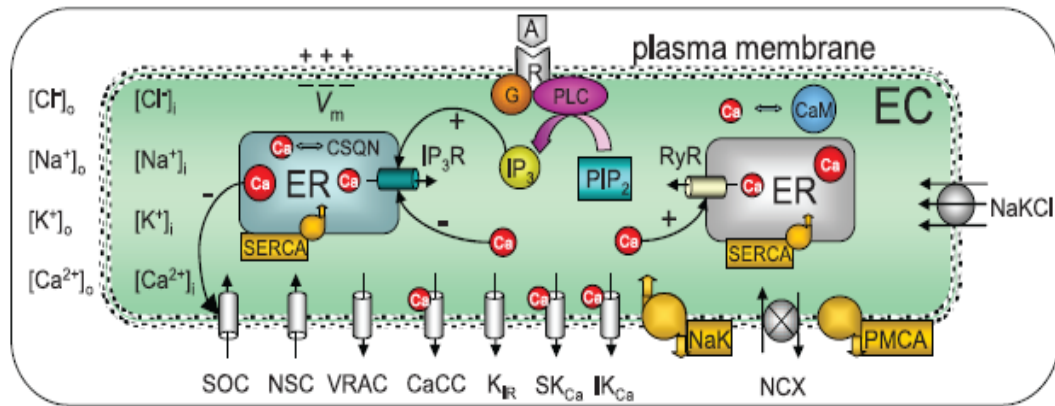


**Figure 1.3 Schematic diagram of EC model components and their interactions [78]**

The model reproduces experimentally observed Ca<sup>2+</sup> transients during agonist stimulation. Up to this date, the majority of the EC models were compartmental in nature. Recently, Hong et al [79] developed a 2-D finite element model that incorporated intracellular resolution and spatial concentration gradients. This study highlighted the need for subcellular resolution in future models of EC Ca<sup>2+</sup> dynamics and signaling.

## **Chapter 2: Myoendothelial communication**

Myoendothelial communication is an important aspect of vascular tone regulation. Complex bidirectional pathways exist between the EC and smooth muscle cell SMC layer which form tightly controlled feedback loops to regulate  $\text{Ca}^{2+}$  in the SMC and maintain the arterial tone. The importance of myoendothelial signaling has been shown not only in local feedback mechanisms [80] but also in long term vasoactive phenomena such as conducted responses along the vessel [81] and spontaneous synchronized constriction and dilation of vessels also known as vasomotion. Many myoendothelial pathways have been identified in the vasculature and are discussed below.

### **2.1 Gap junction coupling**

Vascular cells communicate with each other primarily via electrochemical coupling due to gap junction proteins [82]. Gap junction proteins known as connexins (Cxs) are present all along the vasculature with highest numbers in the microcirculation [83]. Gap junctions can be both homocellular i.e. connecting two ECs or two SMCs or heterocellular i.e. connecting an EC and SMC. The latter are also known as myoendothelial gap junctions (MEGJs). Electrochemical coupling properties of MEGJs have been established using direct as well as indirect methods like electron microscopy and dye coupling between the two cells [84-86]. Myoendothelial signaling is highly diminished or even abolished in the presence of gap junction blockers like 18-glycyrrhetic acid (18-GA) and carbenoxolone [87-94]. Gap junctions physically connect the cytoplasm of two cells allowing low resistance pathway for exchange of ions and other small second messenger molecules like  $\text{IP}_3$ . Gap junctions are believed to be nonselective in nature with similar permeabilities for all ions and  $\text{IP}_3$  [82, 95]. Literature

values of gap junction resistances ( $R_{gj}$ ) are spread over a large range of 70 – 900 M $\Omega$  depending on the particular tissue and experimental conditions [96-98]. The value of  $R_{gj}$  will affect the permeability of different ions and IP<sub>3</sub> between cells.

## **2.2 Endothelium derived controllers**

Endothelium regulates vascular tone by releasing factors that constrict or relax the smooth muscle cells by changing the intracellular concentration of SMC. Many endothelium derived pathways have been identified in the vasculature such as: endothelium derived relaxing factor (EDRF), prostacyclin (PGI<sub>2</sub>) and endothelium derived hyperpolarizing factor (EDHF) among others [80, 99, 100] which cause agonist induced vasodilation of SMCs as shown in Figure 2.1.

One or more of these pathways are often found disrupted in diseases related to altered vasoreactivity such as hypertension, diabetes etc [64, 101, 102].

### **2.2.1 Nitric oxide**

Nitric oxide was identified as the endothelium derived relaxing factor in 1980 [103]. NO plays a crucial role in several physiological processes such as reproduction, inflammation, neurotransmission, host defense response, apoptosis, regulation of vascular tone and blood flow [104, 105]. The nitric oxide molecule is extremely reactive owing to an unshared pair of electron and is vital to many physiological and pathological processes. NO is produced inside the body by the enzymatic degradation of nitric oxide synthase (NOS). Three different forms of NOS exist which are expressed on tissues or whose expression is induced by cytokines [106]. Inducible NOS (iNOS) produces NO in the nano to micromolar range. Endothelial NOS (eNOS) and neuronal NOS (nNOS) are expressed constitutively and can produce NO in the pico to nano molar range. NO is

produced in the endothelium in response to agonist or hemodynamic stimulation. NO is produced by oxidation of guanidine nitrogen of L-Arginine to L-citrulline in the presence of eNOS which is the isoform of NOS present in endothelial cells.

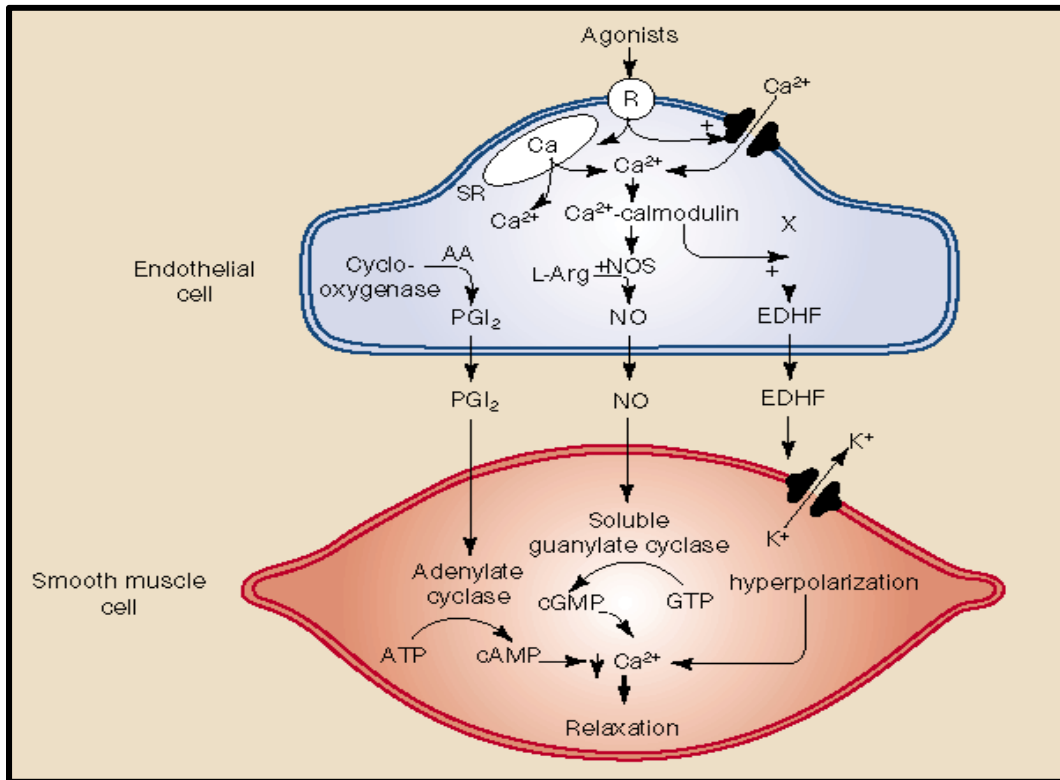


**Figure 2.1 Schematic of some identified endothelium derived pathways (Figure adapted from [107])**

This NO diffuses to the overlying SMC and increases the concentration of cyclic guanine monophosphate (cGMP) in two step reaction kinetics. NO first reacts with soluble guanylate cyclase (sGC) to form a 5 coordinate sGC-NO complex. This catalytically active compound then converts guanine triphosphate (GTP) into cGMP. The increase in cGMP causes an increase in protein kinase (PKG) which decreases intracellular concentration of free  $Ca^{2+}$ . cGMP also effects channels on SMC membrane like  $BK_{Ca}$  channels, NCX and CaCC to decrease the concentration of  $Ca^{2+}$ . A decrease in free  $Ca^{2+}$  concentration has an inhibitory effect on the activation of myosin light chain kinase (MLCK) thus leading to

relaxation of the SMC. The NO produced by eNOs expressed in the cells is in the nano molar range which is sufficient for the activation of sGC [108].

### **2.2.2 Prostacyclin**

Prostacyclin (PGI<sub>2</sub>) was discovered in 1976 and characterized as an endogenous anticouagulator for platelets and a strong vasodilator. PGI<sub>2</sub> is produced by the cyclooxygenase (COX) system. COX is an integral protein in microsomal membranes [109]. In tissues, arachidonic acid (AA) is converted to prostaglandin H<sub>2</sub> (PGH<sub>2</sub>) by COX which is further reduced to PGI<sub>2</sub> by the action of PGI<sub>2</sub> synthase (PGIS). PGI<sub>2</sub> can be produced in the body by either COX-1 or COX-2 coupled to PGIS [110]. The signaling pathways of PGI<sub>2</sub> constitutes of a G-protein coupled cell surface receptor called IP [66]. Activation of IP stimulates adenylyl cyclase production leading to an increased production of cAMP. cAMP in turn protein kinase A cascade or phospholipase C activation [66]. Both EC and SMC have the ability to generate PGI<sub>2</sub> via PGIS. However, in rat mesenteric arterioles, PGI<sub>2</sub> does not exert a hyperpolarizing effect. The involvement of PGI<sub>2</sub> pathways is usually studied using COX inhibitor (Indomethacin).

### **2.2.3 Endothelium derived hyperpolarizing factor**

EDHF is an endothelium derived non- nitric oxide (NO) and non-cyclooxygenase (COX) hyperpolarizing pathway that is involved in the regulation of vascular tone in many arterial beds. Since its introduction in the 1970s [111] around the same time as EDRF, EDHF has been extensively researched and reviewed [99, 112, 113], but hasn't attained consensus regarding its identity or mechanism. EDHF is the dominant mode of vascular tone regulation in the microcirculation and is an often found disrupted in many diseased animal models like hypertension, diabetes etc. [83, 114]. Hence, its elucidation

will be vital to developing therapeutic strategies in combating these diseases. The non-uniformity of experimental studies and a lack of a clear definition of what constitutes as EDHF action have been major obstacles in the elucidation of EDHF mechanisms. This is further complicated by the fact the EDHF action might propagate by a single pathway or a combination of different pathways depending on the type of species, tissue, size of arterial bed, age, and even the level of constriction in the arteries [87, 90, 94, 96, 115, 116]. Another common obstacle in the study of EDHF is the unavailability of selective blockers for different ion channels and gap-junction proteins. In spite of all the difficulties, certain critical advances have been made over the years; experimentalists have standardized certain attributes to distinguish EDHF from other similar endothelium derived actions. Increase in EC  $Ca^{2+}$  and EC hyperpolarization by activation of  $IK_{Ca}$  and  $SK_{Ca}$  is now a widely accepted finger print of EDHF action across many studies. However, its propagation to the SMC is still being investigated.

### **2.3 Myoendothelial feedback**

Studies have shown that endothelium derived pathways can also be induced during SMC stimulation which brought about the concept of myoendothelial feedback. The idea was based on the observed global  $Ca^{2+}$  changes in EC following SMC stimulation [80]. Some studies have also reported local  $Ca^{2+}$  events in the EC after SMC stimulation [117-120]. The proposed action of endothelial feedback principally relies on the movement of  $Ca^{2+}$  and/or  $IP_3$  from the stimulated SMCs to EC leading to an experimentally observed global and/or local  $Ca^{2+}$  mobilization [80, 117-119, 121, 122] sufficient to activate  $Ca^{2+}$  dependent vasodilatory mechanisms in the EC. The theory of

endothelial feedback is now generally accepted, however, the nature of this feedback response (local or global) and its main contributor ( $\text{Ca}^{2+}$  or  $\text{IP}_3$ ) still remain unresolved.

## 2. 4 Theoretical modeling of myoendothelial communication

### 2.4.1 Modeling of gap junction fluxes

Modeling intercellular coupling through gap junctions depends foremost on the questions being addressed by a model, and cellular description. Traditionally, two signaling pathways have been studied in multicellular systems: electrical coupling and diffusion of second messenger  $\text{Ca}^{2+}$  and/or  $\text{IP}_3$ . These two modes of communication were often studied and modeled in separation from each other. With the advent of more detailed cellular models, integrating  $\text{Ca}^{2+}$  dynamics with membrane electrophysiology, electrical and diffusional fluxes can be unified as electrodiffusion of various cytosolic species.

#### a) Electrical coupling

To study their electrical properties, micro vessels can be considered as continuous 1D cable. Discrete electrical equivalents have been formulated, in which cell membrane is represented by capacitor and parallel nonlinear conductance, while gap junctions are assumed ohmic resistances [123]. Under this approximation, electric current between two coupled cells can be calculated as:

$$I_{\text{gj}} = (V_m^n - V_m^m)/R_{\text{gj}} = \Delta V_{\text{gj}}/R_{\text{gj}} \quad (2.1)$$

where  $R_{\text{gj}}$  is gap junction resistance, and  $\Delta V_{\text{gj}}$  represents  $V_m$  cells n-th and m-th (Figure 2.2).

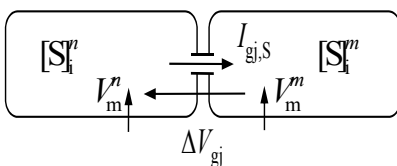


**Figure 2.2 Schematic diagram of two cells,  $n$  and  $m$ , connected by gap junctions permeable to ionic species  $S$ , generating intercellular current proportional to electrochemical gradient.**



### b) Diffusional coupling

A generic model of gap junctional diffusion of second messenger molecules in the vascular wall of a small resistance vessel has been described by Christ et al. [124]. In a linear chain of cells, concentration of species  $S$  is described by one-dimensional diffusion equation. Gap junction communication is implemented as boundary flux proportional to concentration difference at the edges of the prejunctional and postjunctional cells:

$$J_{gj,S} = P_{gj,S}([S]_i^n - [S]_i^m) \quad (2.2)$$

where  $P_{gj,S}$  is the gap junction permeability to  $S$  (e.g.,  $Ca^{2+}$ ,  $IP_3$ , cAMP, cGMP). This approach does not require detailed cellular models, it is easy to implement, and it allows certain analytical solutions, such as effective diffusion coefficient and concentration profiles.

### c) Electrochemical coupling

Ionic motion is governed in general by the Nernst-Planck equation for the electro diffusion. Assuming ionic independence and constant electric field, a current of an ionic species via gap junctions can be estimated with the Goldman-Hodgkin-Katz (GHK) equation:

$$I_{gj,S} = P_{gj,S} \frac{z_s^2 F^2}{RT} \Delta V_{gj} \frac{[S]_i^n - [S]_i^m \exp(-z_s F \Delta V_{gj} / RT)}{1 - \exp(-z_s F \Delta V_{gj} / RT)} \quad (2.3)$$

where  $z_s$ ,  $F$ ,  $R$  and  $T$  are the valence of ion  $S$ , Faraday's constant, gas constant and temperature, respectively. GHK equation describes an ionic current between two coupled cells as a function of  $V_m$  and concentration differences, i.e., electrochemical gradient. It predicts rectifying  $I-V$  relationship when ionic concentrations are unequal, with larger conductance when current flows from the higher concentration side [125]. The

rectification is low at physiological concentration gradients, and a simpler linear approximation can also be used:

$$I_{gj,S} = P_{gj,S} z_S F \left( \Delta[S]_{gj} + \frac{z_S F}{RT} [\bar{S}]_{gj} \Delta V_{gj} \right) \quad (2.4)$$

where  $\Delta[S]_{gj} = [S]_i^n - [S]_i^m$ , and  $[\bar{S}]_{gj} = ([S]_i^n + [S]_i^m)/2$  is the average concentration across gap junction. This equation was used to calculate  $Ca^{2+}$  fluxes between SMCs during vasomotion [126]. Concentrations of  $K^+$ ,  $Cl^-$ , and  $Na^+$  were constant and the same in all cells, and the Eq. 2.4 for these ions reduced to Eq. 2.1. These are suitable assumptions for homocellular couplings where cytosolic species, except  $Ca^{2+}$ , are effectively symmetrical at the examined time scale. In case of heterocellular coupling,  $V_m$  and concentrations of all cytosolic species may have significant gradients, and cellular models should account for the effect of resulting steady state and transient fluxes on the intracellular concentrations.

#### 2.4.2 Multicellular modeling

One or more of the above described forms of gap junction communication have been used to account for the effect of EC-SMC interaction in various microcirculatory phenomena such as vasomotion [127], conducted responses [123, 128], and myoendothelial feedback [129].

We have recently presented a theoretical analysis of myoendothelial communication [129] by integrating an isolated EC [78] and a SMC[56] model shown in Figure 2.3. The cells were coupled by nonselective gap junctions (permeable to  $Ca^{2+}$ ,  $K^+$ ,  $Na^+$  and  $Cl^-$  ions, and to  $IP_3$ ) and the diffusion of NO (Figure 2.3).

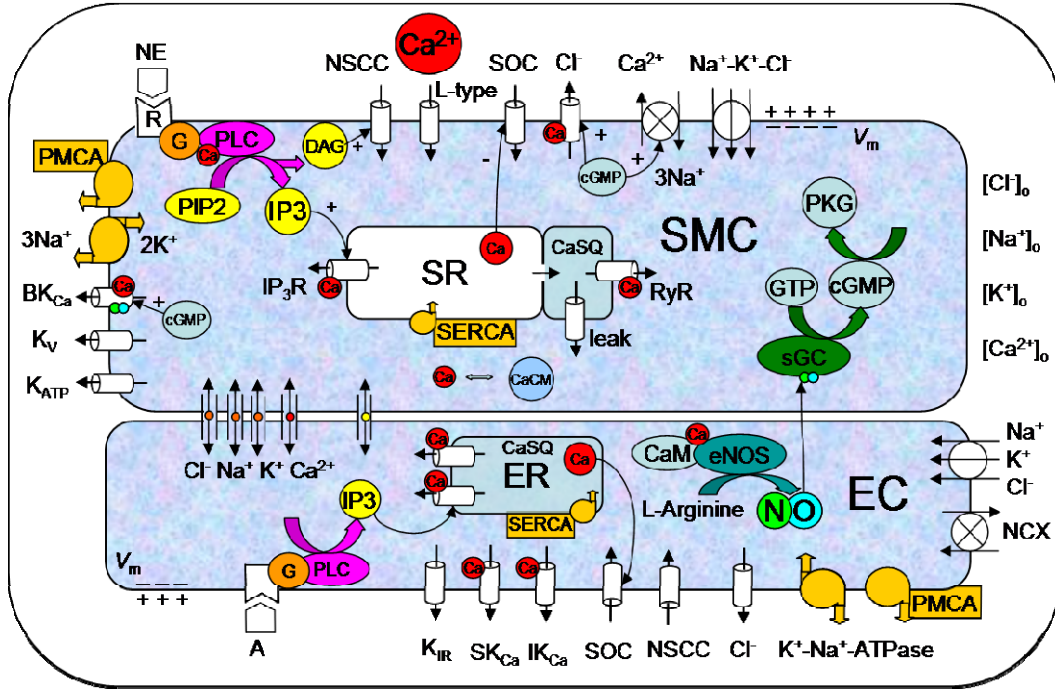


Figure 2.3 Schematic diagram of EC SMC model [129]. The cells are coupled by gap junctions and NO coupling.

SMC was agonist-activated through  $\alpha_1$ -adrenoceptors and NSC channels that cause membrane depolarization, opening of VOCC channels, and increase in intracellular Ca<sup>2+</sup>. EC agonist generated IP<sub>3</sub> that activates IP<sub>3</sub>R and increases cytosolic Ca<sup>2+</sup>, which opens SK<sub>Ca</sub> and IK<sub>Ca</sub> channels and hyperpolarizes EC. The model was able to capture many of the known features of EC-SMC interaction. EC stimulation increased EC Ca<sup>2+</sup>, but reduced SMC Ca<sup>2+</sup> through the EDHF and EDRF mechanisms. The EDHF action was due to hyperpolarizing current flowing through MEGJs and was abolished in a synergistic manner by inhibition of EC SK<sub>Ca</sub> and IK<sub>Ca</sub> channels. Following stimulation of either cell, the predicted myoendothelial Ca<sup>2+</sup> fluxes were too small to affect bulk Ca<sup>2+</sup> in the other cell. Significant gap junction permeability to IP<sub>3</sub> and EC IP<sub>3</sub>R currents had to be assumed in order to capture the feedback response to SMC stimulation in the model.

### **Chapter 3: Conducted responses in blood vessels**

This chapter was published as follows (with slight modifications)

Kapela, A., S. Nagaraja, et al. 2009, "A mathematical model of vasoreactivity in rat mesenteric arterioles.II. Conducted vasoreactivity. "Am J Physiol Heart Circ Physiol 298(1):H52-65

#### **Abstract**

This study presents a multicellular computational model of a rat mesenteric arteriole to investigate the signal transduction mechanisms involved in the generation of conducted vasoreactivity. The model comprises detailed descriptions of endothelial (ECs) and smooth muscle (SMCs) cells coupled by nonselective gap junctions. With strong myoendothelial coupling, local agonist stimulation of the EC or SM layer causes local changes in membrane potential  $V_m$  that are conducted electrotonically primarily through the endothelium. When myoendothelial coupling is weak, signals initiated in the SM conduct poorly, but the sensitivity of the SMCs to current injection and agonist stimulation increases. Thus, physiological transmembrane currents can induce different levels of local  $V_m$  change depending on cell's gap junction connectivity. The physiological relevance of current and voltage clamp stimulations in intact vessels is discussed. Focal agonist stimulation of the endothelium reduces cytosolic calcium ( $[Ca^{2+}]_i$ ) in the prestimulated SM layer. This SMC  $Ca^{2+}$  reduction is attributed to a spread of EC hyperpolarization via gap junctions.  $IP_3$ , but not  $Ca^{2+}$ , diffusion through homocellular gap junctions can increase  $[Ca^{2+}]_i$  in neighboring ECs. The small endothelial  $Ca^{2+}$  spread can amplify the total current generated at the local site by the ECs and through the nitric oxide pathway, by the SMCs, and thus reduces the number of

stimulated cells required to induce distant responses. The distance of the electrotonic and  $\text{Ca}^{2+}$  spread depend on the magnitude of SM prestimulation and the number of SM layers. Model results are consistent with experimental data for vasoreactivity in rat mesenteric resistance arteries.

Keywords: intercellular communication, membrane potential, calcium dynamics

### **3.1 Introduction**

Focal application of certain vasoactive agents to micro vessels may cause significant vasomotor responses both locally and at relatively distant sites. The distant responses are mediated by intrinsic signal transduction mechanisms within the vascular wall, independently of the diffusion of the stimulating agent, hemodynamic effects, or innervations. These conducted responses have been reported in different vascular beds and species [130-134] and may play a role in both the rapid and long-term coordination of microvascular function. Vasodilatation initiated locally by increased metabolic demand may be conducted upstream to feed arteries to allow adequate increase in blood flow [135, 136]; conducted vasoconstriction may be important in the tubuloglomerular feedback mechanism of renal autoregulation [133]; and theoretical simulations suggest that axial communication in the vasculature is required to suppress the generation of large proximal shunts during long-term structural adaptation of microvascular networks [137].

The underlying mechanisms of spreading responses remain poorly understood, but electrotonic transmission of membrane potential changes ( $\Delta V_m$ ) and  $\text{Ca}^{2+}$  waves through the endothelium seem to play the major role [138, 139]. In some vessels, including in rat mesenteric resistance arteries (RMA), the signal is attenuated away from the stimulus site and the vasoreactivity observed at a distant site is attributed to  $\text{Ca}^{2+}$ -

independent passive electronic diffusion through gap junctions [81, 133]. In other vascular beds, the conducted signal can spread over significant distances with minimal attenuation and thus facilitating/regenerative mechanisms should be involved [140]. A number of hypotheses have been proposed to account for the facilitation of the transmitted signal. One suggestion is that membrane hyperpolarization is enhanced by inwardly rectifying potassium ( $K_{ir}$ ) channels and/or the sodium-potassium pump (NaK) [141]. Alternatively, a wave of nitric oxide (NO) release along the arteriolar endothelium, triggered by a spread of  $Ca^{2+}$  could induce spreading dilatation [142, 143]. Remote  $Ca^{2+}$  waves have been reported in hamster feed arteries [143, 144]. A regenerative mechanism based on the activation of endothelial voltage-dependent sodium ( $Na_v$ ) and calcium ( $Ca_v$ ) channels has also been suggested [145].

A number of theoretical studies have been performed to investigate spreading responses. Hirst and Neild [146] modeled a vessel segment as a continuous wire with uniform axial resistance and applied traditional cable theory to determine its electrical properties. Crane et al. [147] used a cable model to simulate the spread of  $V_m$  changes in microvascular trees. The results of these simulations suggest that a thick smooth muscle layer could favor electrical conduction, but passive conduction was insufficient to explain the experimental recordings. Haug and Segal [148] predicted with a similar passive cable model that the inhibition of conducted vasodilation by  $\alpha_1$ - and  $\alpha_2$ -adrenoceptors can be explained by decreased smooth muscle cell (SMC) membrane resistance or increased myoendothelial resistance. Diep et al. [123] developed a detailed computational model of skeletal muscle resistance artery with discrete SMCs and endothelial cells (ECs). Each cell was treated as a capacitor coupled in parallel with a non-linear resistor representing

ionic conductance. Intercellular gap junctions were represented by ohmic resistances. According to the simulations, the vessel wall was not a syncytium and electrical stimuli did not spread uniformly. The cells' orientation and coupling resistances were the critical factors in determining the differential electrical communication within and between the endothelium and the smooth muscle.

Previous theoretical studies [123, 146-148] have focused mostly on the electrical behavior of the vessel and have provided insights into the major aspects of spreading responses. To assist further in the elucidation of mechanisms and parameters of the phenomenon, we developed a more comprehensive computational model of a vessel segment that integrates subcellular components and mechanisms with intercellular signaling between neighboring cells in the vascular wall. Unlike earlier models, it incorporates detailed descriptions of  $\text{Ca}^{2+}$  dynamics and plasma membrane electrophysiology in vascular endothelial and smooth muscle cells. The discrete cells are coupled by the NO pathway and by homocellular and heterocellular gap junctions permeable to  $\text{Ca}^{2+}$ ,  $\text{K}^+$ ,  $\text{Na}^+$ , and  $\text{Cl}^-$  ions, and  $\text{IP}_3$ . The present study focuses on the behavior of rat mesenteric vessels and it does not account for mechanisms observed in other vessel types. It forms however a theoretical framework for developing similar models in other vessel types. The model predicts  $V_m$  and  $\text{Ca}^{2+}$  responses along the vessel segment under various scenarios of agonist stimulations. It investigates the mechanisms that can enhance or attenuate the transmitted signal in conducted vasoreactivity, the contribution of the intercellular diffusion of second messengers in the phenomenon, and the currents generated by membrane channels. We also examine responses to external

current injections, and discuss the physiological relevance of experimental protocols of electrical stimulation.

## **3.2 Methods**

We have previously developed detailed mathematical models of plasma membrane electrophysiology and  $\text{Ca}^{2+}$  dynamics in isolated EC [78] and SMC [56]. Schematics of these models are depicted in Figure 3.1. Both cellular models are based primarily on data from RMA. Only the salient features of these models are presented here.

### **3.2.1 Multicellular vessel model**

A 3 mm arteriolar segment was constructed through the appropriate arrangement of ECs and SMCs (Figure 3.2), similar to the study by Diep et al. [123]. We assume a single layer of SMCs is surrounding the ECs. The SMCs are aligned perpendicular to the ECs and the vessel axis. The vessel model was reduced to two dimensions (axial and radial) on the assumption that concentration and potential gradients in the circumferential direction are negligible [147]. These gradients should be minimal during circumferentially uniform stimulations, but are small even during local stimulation with an intracellular microelectrode [146]. In this study we assume that an EC spans 15 SMCs and vice versa. This results in an EC to SMC population ratio in the vascular wall of 1:1 and assumes a SMC width equal to 1/15 of the EC length. Representative cell dimensions and population ratios of ECs and SMCs from various tissues are summarized in Table 3.1. The exact cell dimensions can vary significantly between different tissues and with vessel size.



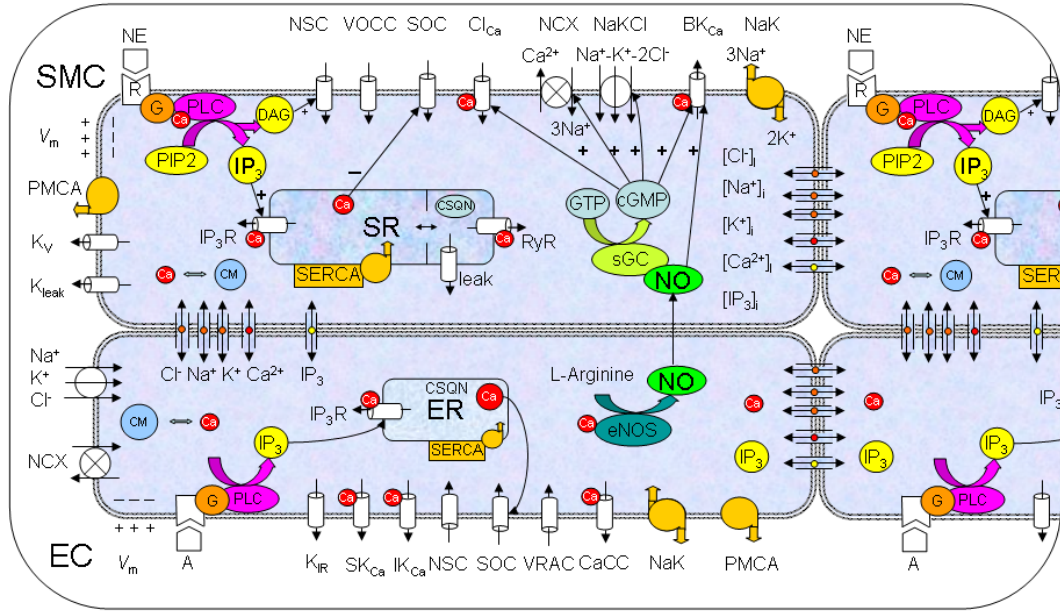


**Figure 3.1 Schematic diagram of the EC and SMC models. Cells are coupled by nitric oxide (NO) and myoendothelial gap junctions permeable to  $\text{Ca}^{2+}$ ,  $\text{Na}^+$ ,  $\text{K}^+$ , and  $\text{Cl}^-$  ions, and  $\text{IP}_3$ .**

| Parameter                    | Range    | Assumed value | References                   |
|------------------------------|----------|---------------|------------------------------|
| EC length ( $\mu\text{m}$ )  | 50 – 141 | 100           | [81, 96, 123, 149, 150]      |
| EC width ( $\mu\text{m}$ )   | 5 – 10   | 6.7           | [123, 149, 150]              |
| SMC length ( $\mu\text{m}$ ) | 50 – 100 | 100           | [96, 98, 123, 126, 149, 151] |
| SMC width ( $\mu\text{m}$ )  | 2 – 8    | 6.7           | [96, 98, 123, 149, 151]      |
| # SMCs / EC                  | 10 – 20  | 15            | [96, 123, 149, 151]          |
| # ECs / SMC                  | 5 – 16   | 15            | [123, 149, 151]              |

**Table 3.1 Cell dimensions and the population ratios of ECs to SMCs in various tissues and computational models**

An EC length of 100  $\mu\text{m}$  is assumed in this study in order to translate the number of cells through which a signal is transmitted, into a longitudinal distance. Due to the

circumferential symmetry, only one SMC is implemented at each discrete axial position along the vessel (Figure 3.2). We assume that each cell is connected with its neighbors in the same layer and with overlapping cells on the other layer. Only one EC at a given axial position is simulated and identical ECs are assumed in the circumferential direction (Figure 3.2). The overlapping arrangement of ECs is simplified and replaced by a serial arrangement with regular end to end couplings as shown in Figure 3.2. The ECs' effect on a neighboring SMC is estimated by multiplying the myoendothelial flux into a SMC by fifteen (i.e. one for each of the fifteen identical ECs that overlap the SMC). The simulated vessel segment is 3 mm long, and incorporates 450 ECs and 450 SMCs. [Note that only 30 of the 450 ECs are simulated since there are 15 identical ECs in each longitudinal position]. An actual vessel segment of the same length should contain a higher number of cells that is dependent on the vessel's diameter. The assumption of circumferential symmetry allows us to significantly reduce the number of simulated cells and thus the number of differential equations.

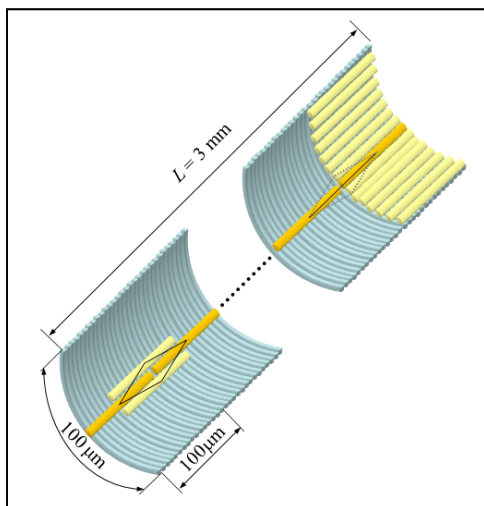


**Figure 3.2** Arrangement of ECs and SMCs in the vessel model. Fifteen SMCs overlap each EC, and fifteen ECs overlap each SMC. A serial arrangement of ECs with regular end-to-end couplings is assumed (shown in the right side of the vessel) as equivalent to the overlapping arrangement (shown in the left side). Circumferential symmetry allows us to consider only one SMC and one EC at each discrete position along the vessel. The whole vessel segment is 3 mm long, spanning 30 ECs and 450 SMCs in the axial direction.

The electrical equivalent of the model vessel is shown in Figure 3.3. We assumed electrically sealed ends [146], small intracellular and extracellular resistances, and negligible effect of tight junctions between ECs. The model assumes that the individual ECs and SMCs are isopotential [149], and without intracellular concentration gradients. For spatially uniform endothelial and/or smooth muscle stimulation, the vessel model is equivalent to a two-cell EC/SMC model, a scenario that has been examined elsewhere [129]

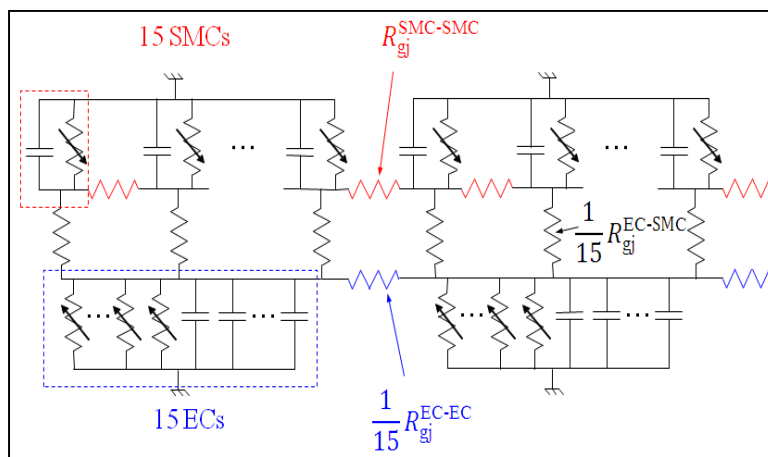


**Figure 3.3** The electrical analogue of the vessel model. Gradients in the circumferential direction are negligible and each cell is connected with its neighbors on the same layer and with the overlapping cells on the adjacent layer. Fifteen identical ECs are assumed and the effect of ECs on neighboring SMCs is included by multiplying myoendothelial fluxes into a SMC by fifteen times (i.e. resistance decreases 15-fold).

### 3.2.2 Intercellular communication

a) Cell coupling through gap junctions: Homocellular gap junctions are present in the endothelium and smooth muscle but are usually more prevalent in the endothelium [96, 133, 138, 152]. Myoendothelial gap junctions, connecting SMCs with ECs, are present in RMA [89, 96], although they may be absent in some other vessels [138]. The homo- and hetero-cellular gap junctions are thought to be nonselective and permeable to ions, as well as to  $IP_3$  molecules [82, 95]. In this model all neighboring cells within the smooth muscle or the endothelial layer are connected via homocellular gap junctions while myoendothelial gap junctions connect overlapping EC and SMCs.

**b) Ionic Coupling:** We used a novel approach to account for the electrical coupling of neighboring cells. The detailed balances in intracellular ionic concentrations enable us to partition the total current flow between two cells into currents carried by individual ions (Eq. 3.1). In this way current flow and ionic exchange can be monitored simultaneously. The ionic fluxes through the gap junctions are expressed by four independent Goldman-Hodgkin-Katz equations, one for each ionic species ( $\text{Ca}^{2+}$ ,  $\text{Na}^+$ ,  $\text{K}^+$ , and  $\text{Cl}^-$ ) (Eq. 3.2) [129]:

$$I_{\text{gj}} = \sum_{\text{S}} I_{\text{gj,S}} \quad (3.1)$$

$$I_{\text{gj,S}} = Pz_{\text{S}}^2 \frac{V_{\text{gj}} F^2}{RT} \frac{[\text{S}]_{\text{i}}^n - [\text{S}]_{\text{i}}^m \exp(-z_{\text{S}} V_{\text{gj}} F / RT)}{1 - \exp(-z_{\text{S}} V_{\text{gj}} F / RT)} \quad (3.2)$$

where  $I_{\text{gj}}$  is the total ionic current flowing from cell  $n$  to  $m$ ;  $\text{S} = \text{Ca}^{2+}$ ,  $\text{K}^+$ ,  $\text{Na}^+$ ,  $\text{Cl}^-$ ; is the  $V_{\text{gj}} = V_{\text{m}}^n - V_{\text{m}}^m$  potential drop across the gap junction that is equal to the difference between  $V_{\text{m}}$  of cell  $n$  and cell  $m$ ;  $[\text{S}]_{\text{i}}^n$  is the intracellular concentration of ion  $\text{S}$  in cell  $n$ ;  $z_{\text{S}}$ ,  $F$ ,  $R$  and  $T$  represent the valence of ion  $\text{S}$ , the Faraday's constant, the gas constant and the absolute temperature, respectively. The ionic permeability's depend on the connexin isoforms participating in channel formation and their phosphorylation state but such dependencies have not been incorporated in the model at this stage. Instead, the permeability,  $P$ , is assumed to be the same for all four ions (i.e., gap junctions are nonselective), and represents resultant behavior of various gap junction channels. This parameter has been arbitrarily assigned in previous studies but can be estimated from the total gap junction resistance ( $R_{\text{gj}}$ ) as we have recently described in [129]  $R_{\text{gj}}$  can be determined experimentally and some values for different vascular beds exist in the literature.

$$P = \frac{RT}{F^2 R_{gj} \sum_S (z_S^2 [S]_i)} \quad (3.3)$$

Table 3.2 summarizes different experimental estimates of  $R_{gj}$ , as well as values utilized in previous theoretical studies. Similar simulation results would be obtained if the GHK equations were replaced with an additive model as described in [126], in which the fluxes are proportional to a linear combination of concentration and potential differences, and the gap junction permeability.

| Tissue              | SMCs            | ECs             | SMC/EC                              | Reference |
|---------------------|-----------------|-----------------|-------------------------------------|-----------|
| RMA                 | -               | -               | 70 M $\Omega$ *<br>35 M $\Omega$ ** | [96]      |
| Cultured RMA        | 84.7 M $\Omega$ | -               | -                                   | [153]     |
| Guinea-pig MA       | 90 M $\Omega$   | -               | 900 M $\Omega$ **                   | [98]      |
| HUAEC               | -               | 31.8 M $\Omega$ | -                                   | [154]     |
| HUVEC               | -               | 60.2 M $\Omega$ | -                                   |           |
| Rat skeletal muscle | -               | 3.3 M $\Omega$  | -                                   | [155]     |
| Theoretical models  |                 |                 |                                     |           |
| Generic             | 100 M $\Omega$  | 33 M $\Omega$   | 1000 M $\Omega$<br>**               | [127]     |
| Skeletal muscle     | 90 M $\Omega$   | 3 M $\Omega$    | 1800 M $\Omega$ *                   | [123]     |

|            |         |        |                                 |
|------------|---------|--------|---------------------------------|
| This model | 84.7 MΩ | 3.3 MΩ | 70- 13500 MΩ *<br>4.7-900 MΩ ** |
|------------|---------|--------|---------------------------------|

**Table 3.2** Gap junction resistances

c) IP<sub>3</sub> coupling: The IP<sub>3</sub> flux through the gap junction was assumed to be proportional to the IP<sub>3</sub> concentration difference between the two cells:

$$J_{IP_3} = p_{IP_3} ([IP_3]^n - [IP_3]^m) \quad (3.4)$$

The permeability coefficient,  $p_{IP_3}$ , has not been determined experimentally. Koenigsberger et al. [127] utilized a value for the myoendothelial IP<sub>3</sub> permeability of  $0.05 \text{ s}^{-1}$ , for a gap junctional resistance per SMC of  $0.9 \text{ G}\Omega$ . The value of the IP<sub>3</sub> permeability between two overlapping cells utilized in this study ( $p_{IP_3}^{EC-SMC} = 0.0033 \text{ s}^{-1}$ ) corresponds to the same total cell permeability of the earlier study (Note: the permeability has to decrease 15-fold to account for the distribution of flux into 15 overlapping cells). The permeability of IP<sub>3</sub> should be inversely proportional to  $R_{gj}$ , because an increase in the number of gap junction channels increases in the same proportion both the electrical conductance and permeability for larger molecules. Based on the assumed values for  $R_{gj}^{EC-EC}$  and  $R_{gj}^{SMC-SMC}$  the intercellular permeability's of IP<sub>3</sub> in the endothelial and smooth muscle layers were adjusted accordingly (i.e.  $p_{IP_3}^{EC-EC} = 13.6 \text{ s}^{-1}$ ;  $p_{IP_3}^{SMC-SMC} = 0.53 \text{ s}^{-1}$ ). The IP<sub>3</sub> permeability is larger in the endothelium than in the smooth muscle due to the smaller endothelial  $R_{gj}$ . The regulation of the macromolecule permeability relative to electrical conductance in gap junction channels is not taken into account.

d) NO/cGMP pathway: The EC [78] and SMC [56] models were modified to include a description for myoendothelial communication through the NO/cGMP pathway as previously described [129]. Simultaneous measurements of  $\text{Ca}^{2+}$  and NO in agonist-stimulated ECs indicate that NO production is regulated by cytosolic  $\text{Ca}^{2+}$  [156-158]. EC may also release NO in a  $\text{Ca}^{2+}$ -independent fashion, under some conditions, but such release is not accounted by the model at this stage [159]. Thus, we assumed that the relative NO production rate depends only on EC  $\text{Ca}^{2+}$  concentration with a sigmoidal function. Once released by the endothelium NO can freely diffuse across cell membranes and reach the SM to exercise its vasodilatory action. Theoretical models of NO transport in arterioles [160] predict that the concentration of the endothelium-derived NO in the smooth muscle ( $[\text{NO}]_{\text{SMC}}$ ) is proportional to the EC NO release rate and the concentration profile is relative flat in the smooth muscle in the absence of significant extravascular scavenging. Equations and parameters that relate EC  $[\text{Ca}^{2+}]_i$  to the NO levels in the smooth muscle are presented in [129].  $[\text{NO}]_{\text{SMC}}$  can affect SMC  $[\text{Ca}^{2+}]_i$  and  $V_m$  by modifying four cellular components as described earlier (Figure 3.1).

### 3.2.3 Length constants

A blood vessel can be approximated from the electrical point of view as a cable with certain membrane and internal conductances [146, 161]. In a passive linear cable with infinite length, the steady-state spread of a local potential change is attenuated exponentially:

$$\Delta V_m(x) = \Delta V_{m,\text{max}} \exp(-x/\lambda), \quad x \geq 0 \quad (3.5)$$

where  $x$  is the distance along the vessel from the stimulus site, and  $\Delta V_{m,\text{max}}$  is the maximum change in  $V_m$  at the local site (i.e.  $\Delta V_m(x=0)$ ). The constant ( $\lambda$ ), referred to as

the cable length constant, characterizes the attenuation, and quantifies the extent of spread of voltage changes and the distance that information can be transmitted. If the cable's length ( $L$ ) is finite (i.e., comparable to  $\lambda$ ), the attenuation is not exponential. In a segment with sealed ends, the  $\Delta V_m$  profile is described by the following equation:

$$\Delta V_m(x) = \begin{cases} \Delta V_{m,\max} \cosh\left(\frac{(L-y)-x}{\lambda}\right) / \cosh\left(\frac{L-y}{\lambda}\right), & 0 \leq x \leq L-y \\ \Delta V_{m,\max} \cosh\left(\frac{y+x}{\lambda}\right) / \cosh\left(\frac{y}{\lambda}\right), & -y \leq x \leq 0 \end{cases} \quad (3.6)$$

where  $y$  is the location of the stimulus site (i.e.,  $0 < y < L$ ). Eq. 3.6 is fitted to SMC  $\Delta V_m$  profiles predicted during current and Ach stimulation, and the length constants  $\lambda_{el}$  and  $\lambda_{el,Ach}$ , respectively, are estimated.

In a similar fashion a length constant can be defined for the attenuation of the EC  $Ca^{2+}$  spread along the vessel axis following stimulation and an increase of intracellular  $Ca^{2+}$  at the local site. Fitting the  $Ca^{2+}$  profile with an exponential function yields an apparent length constant for the  $Ca^{2+}$  spread ( $\lambda_{Ca}$ ):

$$\Delta[Ca^{2+}]_i(x) = \Delta[Ca^{2+}]_{i,\max} \exp(-x/\lambda_{Ca}), \quad 0 \leq x \leq L-y \quad (3.7)$$

where  $\Delta[Ca^{2+}]_{i,\max}$  is the EC  $Ca^{2+}$  elevation at the Ach stimulation site (i.e.,  $\Delta[Ca^{2+}]_i(x = 0)$ ). The exponential function was used because the  $Ca^{2+}$  spread in the endothelium was much smaller than the length of the vessel examined, and in spite of the fact the  $Ca^{2+}$  spread is affected by the diffusion of  $IP_3$  in a nonlinear fashion.

### 3.2. 4 Numerical Methods

Each EC and SMC was modeled with 11 and 26 differential equations, respectively, and the vessel segment was described by a system of 12030 differential equations (i.e., 30 ECs  $\times$  11 Eqs./EC + 450 SMCs  $\times$  26 Eqs./SMC). The equations were



coded in Fortran 90 and solved numerically using Gear's backward differentiation formula method for stiff systems (IMSL Numerical Library routine). The maximum time step was 4 ms, and the tolerance for convergence was 0.0005. Eqs.3.6 and 3.7 were fitted in their corresponding domains to the predicted profiles using the least squares method. Both the length constant and the maximum local response were optimized in the fittings.

### 3.3 Results

To examine possible differences in mechanisms and properties of spreading responses induced by agonist and electrical stimulations and the physiological relevance of the latter, we performed simulations with both types of stimuli.

#### 3.3.1 Electrical stimulation

In Figure 3.4, a hyperpolarizing current (-150 pA per EC) was injected for 3 s into the ECs located at  $x = 0$ . (Note that due to circumferential symmetry the current was injected to every EC located at  $x = 0$ ). The circles and squares represent  $V_m$  in SMCs and ECs, respectively, as a function of their location along the longitudinal direction ( $x$ ). The maximum change in  $V_m$  occurred at the local site and was attenuated with distance. The  $V_m$  profile is fitted well by Eq. 3.6 with an apparent length constant,  $\lambda_{el} = 1.6$  mm. [Note that a simple exponential function does not adequately fit the profile and overestimates the length constant]. Low and intermediate values for  $R_{gj}^{EC-SMC}$  of 70 M $\Omega$  or 525 M $\Omega$  (i.e., equivalent to 4.7 M $\Omega$  and 35 M $\Omega$  per single SMC) [96] result in almost identical EC and SMC  $V_m$ . Despite the significant difference in the two resistances there was no observable difference in the  $V_m$  profile (Figures. 3.4, *A* and *B*). A high  $R_{gj}^{EC-SMC}$  of 13.5 G $\Omega$  (i.e., equivalent to 900 M $\Omega$  per single SMC [98]) affects the resting EC and SM  $V_m$

but does not affect  $\lambda_{cl}$  (Figure 3.4 C). Overall a significant increase in  $R_{gj}^{EC-SMC}$  had only a moderate effect on the conduction of signals initiated in the endothelium.

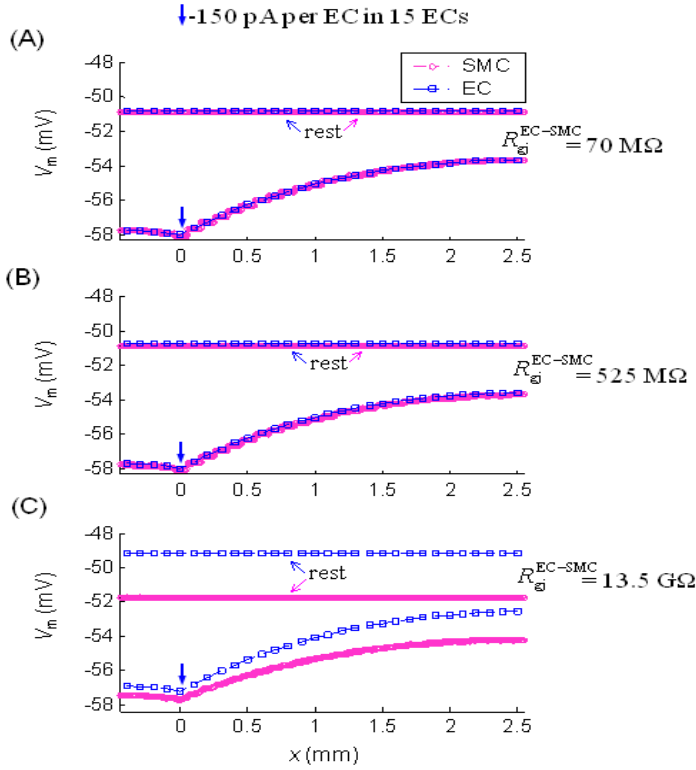


**Figure 3.4** The effect of myoendothelial gap junction resistance on EC (squares) and SMC (circles)  $V_m$  in the 3 mm long vessel at rest and at  $t = 3$  s, after injection of a hyperpolarizing current (-150 pA per EC, for 3 s) into the ECs located at  $x = 0$ . Simulations are shown for a low = 70 M $\Omega$  (A), an intermediate = 525 M $\Omega$  (B) and high = 13.5 G $\Omega$  (C).

In a series of simulations the vessel was also stimulated locally at the SM side. Figures 3.5, A-F present SMC  $V_m$  as a function of longitudinal distance for two different stimulation protocols, utilizing three different values for  $R_{gj}^{EC-SMC}$ . A significant depolarizing current (15x150 pA) was injected into a single SMC located at  $y = 500 \mu\text{m}$  (Figures. 3.5, A, C and E). Alternatively, all SMCs connected to the same EC were stimulated by current injection (150 pA per SMC) (Figures. 3.5, B, D and F) (similar to the arteriolar-segment voltage-clamp protocol presented in [123]). Contrary to the EC stimulation in Figure 3.4, there was a biphasic response when the vessel was stimulated from the SM side. The stimulated cell(s) exhibited significant depolarization that was

more pronounced when  $R_{gj}^{EC-SMC}$  was high (20 mV in Figure 3.5 A vs. 110 mV in Figure 3.5 E) and when the same total current was injected in a single versus a series of SMCs (20 mV in Figure 3.5 A vs. 9 mV in Figure 3.5 B). Away from the stimulus site the length constant of the electrotonic spread was maintained in all four scenarios and was similar to the length constant observed during the EC stimulation ( $\lambda_{el} = 1.6$  mm). The amplitude of distant depolarization, however, decreased as the  $R_{gj}^{EC-SMC}$  value increased (i.e., at  $x = 2.5$  mm there is 3 mV depolarization in Figure 3.5 A vs. 0.5 mV in Figure 3.5 E).

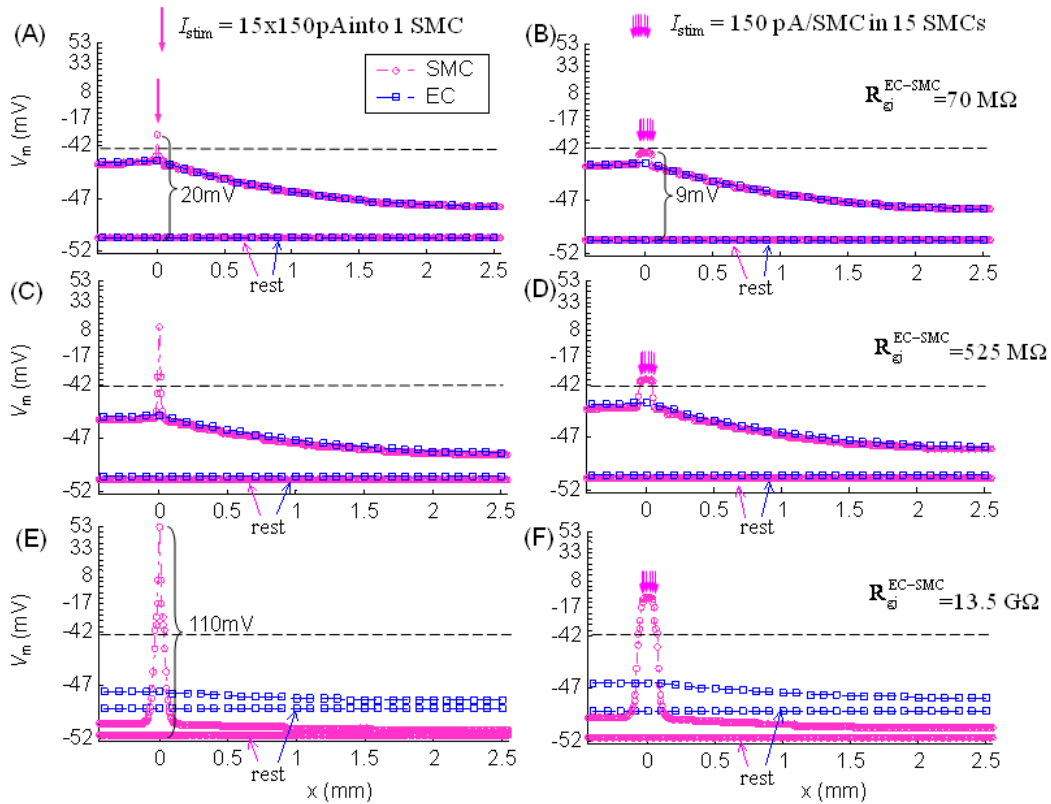


**Figure 3.5** EC (squares) and SMC (circles)  $V_m$  in the 3 mm long vessel at rest and at  $t = 3$  s, after injection of a depolarizing current. 15x150 pA were injected for 3 s into either a single SMC (A, C, E) or to 15 SMCs (B, D, F). Simulations are shown for a low = 70 M $\Omega$  (A, B), an intermediate = 525 M $\Omega$  (C, D) and a high = 13.5 G $\Omega$  (E, F).

The cable length constant can be affected by the gap junction resistances in the endothelial and smooth muscle layers. Some experimental values for homocellular  $R_{gj}$  have been reported in different vascular beds but literature values vary significantly for the inter endothelial  $R_{gj}$  ( $R_{gj}^{EC-EC}$ ). Table 3.3 summarizes model predictions for  $\lambda_{el}$  utilizing different values for the homocellular gap junction resistances.

| $R_{gj}^{SMC-SMC}$ (M $\Omega$ ) \ / \ $R_{gj}^{EC-EC}$ (M $\Omega$ ) | $\frac{3.3}{15 \times 15}$ | $\frac{3.3}{15}$ | 3.3  | 84.7 | $\infty$ |
|---|----------------------------|------------------|------|------|----------|
| 3.3   | -                          | -                | -    | 1.6  | 1.6      |
| 17.5  | -                          | -                | -    | 0.67 | -        |
| 31.8  | -                          | -                | -    | 0.5  | -        |
| $\infty$  | 1.45                       | 0.46             | 0.23 | 0.07 | -        |

**Table 3.3. Predicted electrical length constant,  $\lambda_{el}$  (mm).**

For these simulations, the endothelium was stimulated with current injection similar to Figure 3.4. An  $R_{gj}^{EC-EC}$  in the lower range of the previously reported values (i.e., 3.3 M $\Omega$ ) yields a cable length constant which is consistent with experiments in RMA [81]. Based on this observation we utilized this value for  $R_{gj}^{EC-EC}$  in this study. Disruption of the endothelial gap junctions (i.e.,  $R_{gj}^{EC-EC} = \infty$ ) reduced the length constant by 20 fold, whereas disruption of the smooth muscle gap junctions (i.e.,  $R_{gj}^{SMC-SMC} = \infty$ ) had no significant effect on  $\lambda_{el}$ . In order for the SM layer to conduct changes in  $V_m$  similarly to the endothelium,  $R_{gj}^{SMC-SMC}$  has to be reduced to a value  $15^2$  times smaller than  $R_{gj}^{EC-EC}$ .

This is due to the SMCs' perpendicular orientation relative to the vessel's axis and the number of SMCs assumed to span the length of an EC. Thus, the endothelium is the major pathway for the electrotonic communication in the model. The estimated  $\lambda_{el}$  does not depend significantly on the magnitude and polarity of the injected current provided that the resulting change in  $V_m$  remains within physiological range. Thus, the vessel behaves similar to a linear cable in the physiological range of  $V_m$ , in agreement with experiments (Figure 3 in [146]).

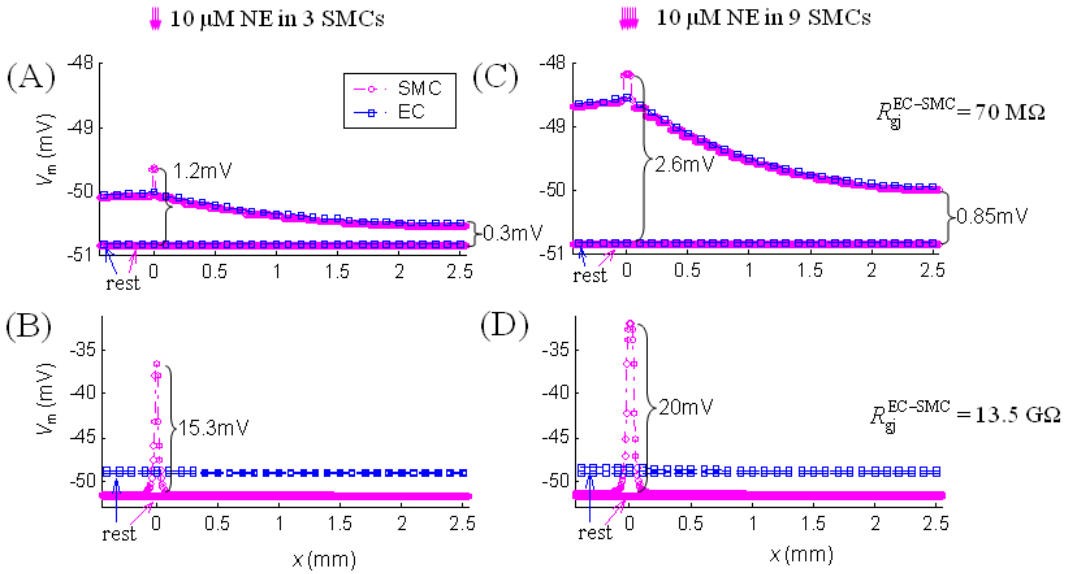


**Figure 3.6.** EC (squares) and SMC (circles)  $V_m$  in the 3 mm long vessel at rest and at  $t = 6$  s, after local NE application. SMCs are stimulated for 6 s with a saturating concentration of NE ( $10 \mu\text{M}$ ). (A) Three adjacent cells are stimulated and a strong myoendothelial coupling is assumed ( $R_{gj}^{\text{EC-SMC}} = 70 \text{ M}\Omega$ ). (B) Three SMCs are stimulated and a weak myoendothelial coupling is assumed ( $R_{gj}^{\text{EC-SMC}} = 13.5 \text{ G}\Omega$ ). (C) Nine SMCs are stimulated and a strong myoendothelial coupling is assumed ( $R_{gj}^{\text{EC-SMC}} = 70 \text{ M}\Omega$ ). (D) Nine SMCs are stimulated and a weak myoendothelial coupling is assumed ( $R_{gj}^{\text{EC-SMC}} = 13.5 \text{ G}\Omega$ ). The same agonist stimulus has a significantly larger effect at the local site if the SM is poorly coupled to the endothelium.

### 3.3.2 Norepinephrine and acetylcholine stimulation

Figure 3.6 presents the change in  $V_m$  along the vessel, after 6 s of localized NE application. In Figures 3.6 A and B three adjacent SMCs were stimulated with saturating

concentration of NE (10  $\mu\text{M}$ ). In the model, NE generates a depolarizing current through activation of the NSC channels (Figure 3. 1). Simulations were performed for low (Figure 3.6 *A*) and high (Figure 3.6 *B*)  $R_{\text{gj}}^{\text{EC-SMC}}$ . The same stimulus had a significantly higher impact on the SMCs at the local site, if the SM was not well-coupled to the endothelium (1.2 mV hyperpolarization in Figure 3.6*A* vs. 15.3 mV in Figure 3.6*B*). In both cases the predicted effect of NE away from the stimulus site was small. In the first case (Figure 3.6 *A*),  $V_m$  changes were conducted effectively along the vessel, but the distant response was small because the total NE-induced transmembrane current was insufficient. In the second case (Figure 3.6*B*), the NE-induced transmembrane current did not diffuse to other cells and produced a large local  $\Delta V_m$ . This change, however, was poorly conducted to distant sites. In Figures 3.6*C* and *D* nine adjacent SMCs were stimulated with a saturating concentration of NE (10  $\mu\text{M}$ ). When the cells were sufficiently coupled with ECs (i.e. low  $R_{\text{gj}}^{\text{EC-SMC}}$ ), local and distant responses to NE were amplified as a result of the increased number of stimulated cells (Figure 3.6*C*).

Figure 3.7 shows a representative Ach-induced conducted response. The simulation scenario mimics the experimental protocol from an earlier study of conducted vasoreactivity in RMA [81]. The difference between the *in silico* and the *in vitro* study is that a sustained local application of the agonist is simulated here. In experiments, transient focal stimulation is utilized to limit the diffusion of agonist away from the local site. Figure 3.7 shows the endothelial  $\text{Ca}^{2+}$  concentration (*A*), the endothelial  $V_m$  (*B*), the smooth muscle  $\text{Ca}^{2+}$  concentration (*C*), and the smooth muscle  $V_m$  (*D*) as a function of time and distance from the stimulation site.

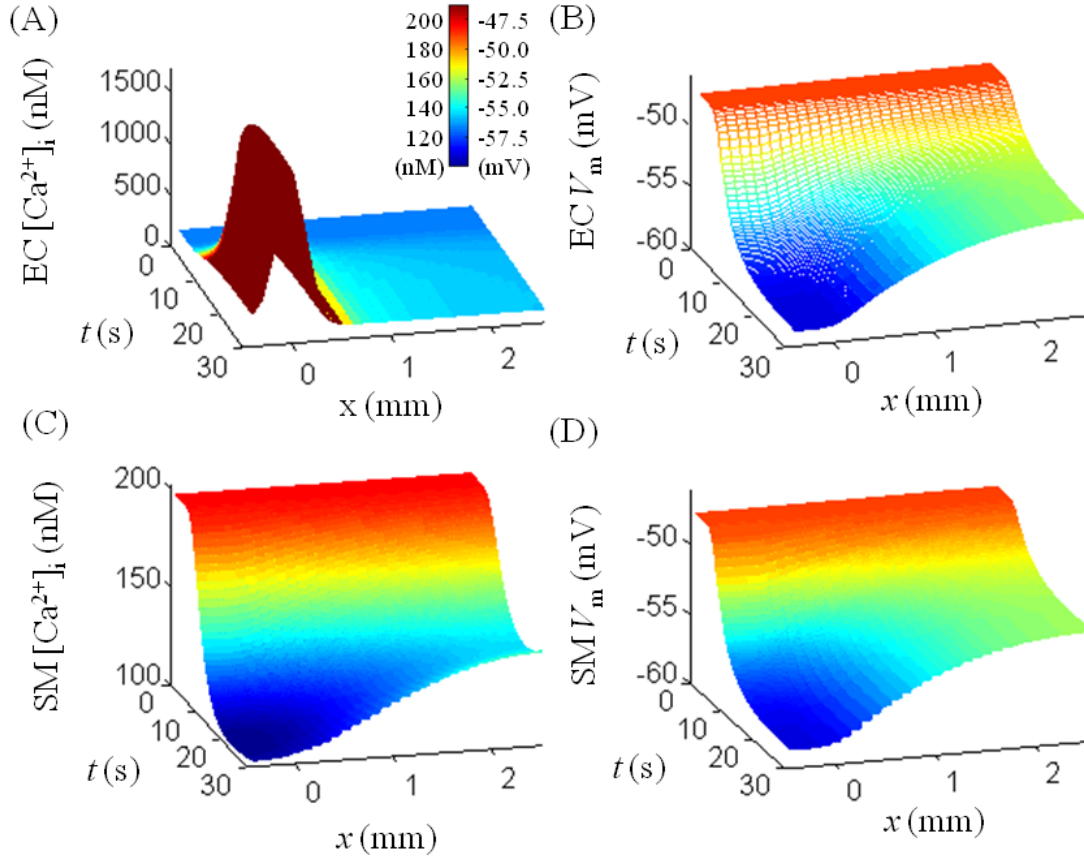


**Figure 3.7. Model responses to local Ach stimulation in a vessel prestimulated with 200 nM of NE and with  $R_{gj}^{EC-SMC} = 525 \text{ M}\Omega$ . From time  $t = 2 \text{ s}$ , the ECs at position  $x = 0$  are continuously stimulated with Ach ( $Q_{IP_{3,ss}} = 0.55 \text{ nM/ms}$ ). (A) Endothelial  $[Ca^{2+}]_i$  as a function of time and distance from stimulus site. (B) Endothelial  $V_m$  as a function of time and distance from stimulus site. (C) Smooth muscle  $[Ca^{2+}]_i$  as a function of time and distance from stimulus site. (D) Smooth muscle  $V_m$  as a function of time and distance from stimulus site.**

First, a continuous and uniform prestimulation of the vessel with 200 nM of NE is simulated until a steady-state is reached ( $t = 0$ ). This results in an elevation of the SM  $Ca^{2+}$  along the entire vessel to around 200 nM. At time  $t = 2 \text{ s}$ , Ach is applied locally to 15 ECs located at distance  $y = 400\text{-}500\mu\text{m}$  from the inlet of the arteriole. The concentration of Ach is not specified, but it is assumed that it increases the  $IP_3$  release rate,  $Q_{GIP_{3,ss}}$ , from 0 to  $0.55 \text{ nM ms}^{-1}$ .  $IP_3$  generation increases the  $[Ca^{2+}]_i$  in the ECs (Figure 3.7A). In response to the elevation of  $[Ca^{2+}]_i$ , the  $SK_{Ca}$  and  $IK_{Ca}$  channels open and hyperpolarize the cell (Figure 3.7B). This hyperpolarization spreads rapidly to

neighboring ECs and SMCs via gap junctions (Figure 3.7B and D). Hyperpolarization of the SMCs closes the VOCCs, and reduces intracellular  $\text{Ca}^{2+}$  (Figure 3.7C). Figure 3.8A depicts relative  $\text{Ca}^{2+}$  changes in the SM along the vessel calculated from Figure 3.7C. A hundred percent change denotes a reduction of  $\text{Ca}^{2+}$  concentration to its resting value prior to NE prestimulation (i.e., from  $\text{SMC } [\text{Ca}^{2+}]_{i,\text{NE}} = 200 \text{ nM}$  to  $\text{SMC } [\text{Ca}^{2+}]_{i,\text{rest}} = 130 \text{ nM}$ ). The model predicts significant  $\text{Ca}^{2+}$  change throughout the vessel segment. Incorporation of the NO pathway in the simulations (Figure 3.8A, *dashed line*) increased slightly the smooth muscle  $\text{Ca}^{2+}$  reduction at the local and at the distant site. The NO/cGMP pathway activates at the local site  $\text{BK}_{\text{Ca}}$  channels in SMCs (Figure 3.1), which generate hyperpolarizing currents. Because the myoendothelial coupling is strong, these currents are transmitted and enhance SM hyperpolarization at distant sites as well. The result is higher  $\text{Ca}^{2+}$  reduction (i.e. relaxation). Inhibition of the inter-endothelial  $\text{IP}_3$  diffusion impaired significantly the Ach-induced SM  $\text{Ca}^{2+}$  reduction (Figure 3.8A, *dashed-dotted line*). The inhibition of  $\text{IP}_3$  diffusion abolishes EC  $\text{Ca}^{2+}$  spread (Figure 3.8B), which reduces the number of ECs with open  $\text{SK}_{\text{Ca}}$  and  $\text{IK}_{\text{Ca}}$  channels. Consequently, the total hyperpolarizing current generated at the local site is smaller, and the SM relaxation is impaired.

Figure 3.8 B investigates the endothelial  $\text{Ca}^{2+}$  spread along the vessel. The difference between the basal pre-stimulation level and the post-stimulation steady-state value of EC  $\text{Ca}^{2+}$  (i.e., Figure 3.7 A;  $t = 0$  and  $t = 30 \text{ s}$ ) is depicted as a function of the distance ( $x$ ) from the stimulation site.  $\text{Ca}^{2+}$  changes are normalized by the maximum change at the local site. Under control conditions (*solid line*), significant  $\text{Ca}^{2+}$  elevation



was observed only within 300  $\mu\text{m}$  from the stimulus site (apparent length constant,  $\lambda_{\text{Ca}}=0.17$  mm).

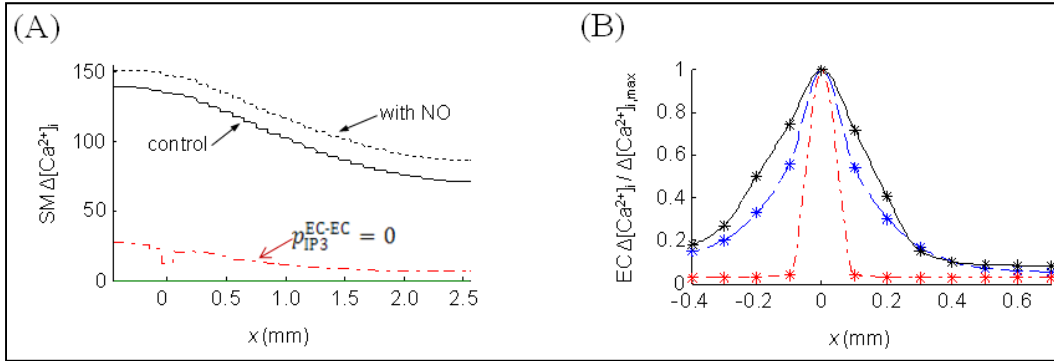


**Figure 3.8. (A) Predicted changes in SM  $[\text{Ca}^{2+}]_i$  during local ACh application in a vessel prestimulated with NE. 100 % change indicates a reduction in  $[\text{Ca}^{2+}]_i$  to the resting value prior to NE application. The figure shows simulations with (dotted line) and without (solid line) contribution from the NO, and after inhibition of endothelial  $\text{IP}_3$  diffusion ( $p_{\text{IP}_3}^{\text{EC-EC}} = 0$ ). (B) Normalized steady-state endothelial  $\text{Ca}^{2+}$  profiles during local stimulation with ACh. Under control conditions (solid line), the  $\text{Ca}^{2+}$  spread was limited to  $\sim 300$   $\mu\text{m}$  (three ECs). Inhibition of axial  $\text{IP}_3$  diffusion ( $p_{\text{IP}_3}^{\text{EC-EC}} = 0$ ) practically abolished the  $\text{Ca}^{2+}$  spread. One hundred-fold greater permeability of the endothelial gap junctions to  $\text{Ca}^{2+}$  extended  $\text{Ca}^{2+}$  spread to  $< 400$   $\mu\text{m}$ .**

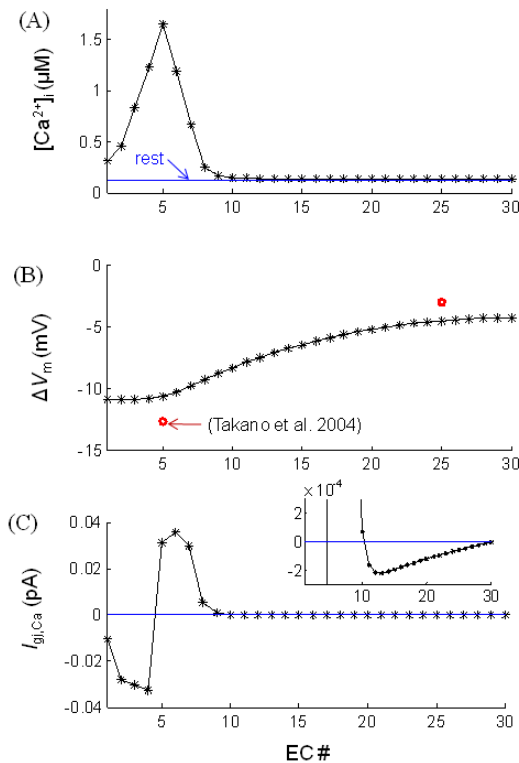
Inhibition of axial  $\text{IP}_3$  diffusion (i.e.,  $p_{\text{IP}_3}^{\text{EC-EC}} = 0$ , *dash-dotted line*) practically abolishes the  $\text{Ca}^{2+}$  spread. In simulation with EC gap junctions impermeable to  $\text{IP}_3$  and hundred times more permeable to  $\text{Ca}^{2+}$  than control (i.e.,  $p_{\text{IP}_3}^{\text{EC-EC}} = 0$ ;  $P_{\text{Ca}}^{\text{EC-EC}} = 100P$ , *dashed line*),  $\text{Ca}^{2+}$  spread is also limited (i.e.,  $< 400$   $\mu\text{m}$ ,  $\lambda_{\text{Ca}}=0.15$  mm).

Figure 3.9 examines the  $\text{IP}_3$ -independent  $\text{Ca}^{2+}$  electrodiffusion through the endothelial gap junctions. Figures 3.9A and B show the post-stimulation steady-state  $\text{Ca}^{2+}$  and  $\Delta V_m$ , respectively, in ECs along the vessel's axis for the simulations presented in Figure 3.7 ( $t = 30$  s). The  $\text{Ca}^{2+}$  flux between neighboring cells is presented as  $\text{Ca}^{2+}$  current (Figure 3.9C). A positive current denotes  $\text{Ca}^{2+}$  ions flowing to the right and a negative current to the left. There is a maximum 500 nM difference in  $[\text{Ca}^{2+}]_i$  and a maximum 0.5 mV difference in  $V_m$  between neighboring ECs at the local site. Under these conditions,

the concentration gradient dominates the electrochemical gradient, and  $\text{Ca}^{2+}$  ions move away from the stimulated EC. The  $\text{Ca}^{2+}$  current through the gap junctions between the fifth and the sixth EC is 0.03 pA. Away from the stimulation site, the concentration difference between neighboring cells decreases and so does the  $\text{Ca}^{2+}$  current. Interestingly, after the tenth EC, a very weak  $\text{Ca}^{2+}$  current flows towards the stimulation site (i.e., the current becomes negative) as the electrical field dominates the electrochemical gradient across the gap junction (Figure 3.9C, *insert*).

### 3.3.3 Effect of stimulus strength on $V_m$ and $\text{Ca}^{2+}$ spread

We investigated if the strength of agonist stimulation can affect the rate of decay of the conducted signal. Figure 3.10 examines the effect of NE prestimulation on the  $\text{Ca}^{2+}$  and electrotonic spread. The model vessel was stimulated uniformly with different concentrations of NE prior to local stimulation of the endothelium with Ach.



**Figure 3.9. Endothelial  $\text{Ca}^{2+}$  electrodiffusion during local Ach stimulation.**  $\text{IP}_3$  release rate is increased in the fifth EC simulating local Ach stimulation. (A) Endothelial  $[\text{Ca}^{2+}]_i$  profile is shown as a function of the number of cells from the inlet of the vessel. (B) Predicted hyperpolarization following stimulation (stars) is presented next to experimental data from [81] (circles). (C) Intercellular  $\text{Ca}^{2+}$  current presenting  $\text{Ca}^{2+}$  flux between neighboring ECs. Positive values denote  $\text{Ca}^{2+}$  flow from the left to the right. Insert shows data at 100-fold higher resolution. Small  $\text{Ca}^{2+}$  fluxes towards the stimulation site appear after the tenth EC.

Figure 3.10 shows the predicted length constants for the endothelial  $\text{Ca}^{2+}$  spread ( $\lambda_{\text{Ca}}$ ) (A) and for the SM  $V_m$  attenuation  $\lambda_{\text{el,Ach}}$  (B), for NE concentrations varying from  $10^{-2}$  to  $10^2$   $\mu\text{M}$ . In Figure 3.10 A the stimulating Ach concentration was either held constant (Figure 3.10, *solid line*) or was modified to produce the same local  $[\text{Ca}^{2+}]_i$  increase at each NE concentration (Figure 3.10, *dotted line*). The  $\lambda_{\text{Ca}}$  can increase significantly with increasing levels of NE prestimulation. This effect is reduced but is not abolished if the same local  $\text{Ca}^{2+}$  transient is preserved at each NE concentration (Figure 3.10, *dotted line*). On the contrary NE prestimulation can reduce  $\lambda_{\text{el,Ach}}$  and thus the electrotonic spread (Figure 3.10 B). The significance of this effect is increased for high myoendothelial gap junction resistance (Figure 3.10, *solid line*). Large NE prestimulation also reduces the magnitude of the SMC  $\Delta V_m$  (data not shown). For endothelium initiated responses, as the concentration of Ach increases so does the local  $\Delta[\text{Ca}^{2+}]_i$ ,  $\Delta V_m$ , and  $\lambda_{\text{Ca}}$ , but not  $\lambda_{\text{el,Ach}}$  (data not shown).

### 3.4 Discussion

#### 3.4.1 Role of gap junctions in $V_m$ spread

Gap junctions composed of specific connexins are central to the propagation of dilations [162, 163]. Electrotonic conduction of  $V_m$  changes through gap junctions is considered to be the major mechanism of spreading responses in a number of vascular beds [133]. The endothelium, rather than the SM, seems to be the major conducting pathway in RMAs, as supported by experiments with disrupted endothelial layer [81]. Model simulations with electrical and agonist stimuli confirm these findings. Simulations demonstrate that the cable length constant,  $\lambda_{\text{el}}$ , is inversely proportional to the square root

of  $R_{gj}^{EC-EC}$ . (Note: in a passive linear cable the length constant exhibits the same dependence on axial resistance). The exact value of  $R_{gj}^{EC-EC}$  in RMA is not known.

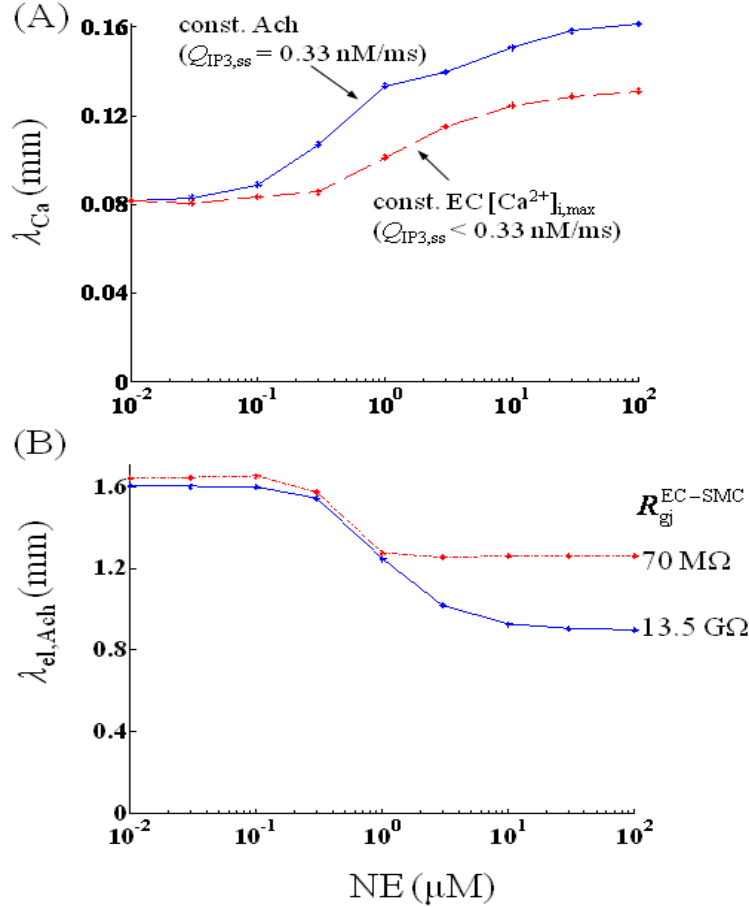


**Figure 3.10 (A)** The length constant ( $\lambda_{Ca}$ ) of  $Ca^{2+}$  decrease from the site of local Ach stimulation is shown for different levels of NE prestimulation. Ach stimulus strength was either held constant ( $Q_{IP3,ss} = 0.33$  nM/ms) (solid line) or was adjusted to produce the same local  $Ca^{2+}$  response at each prestimulation level (dashed line). (B) The length constant of  $V_m$  attenuation ( $\lambda_{el,Ach}$ ) is shown for vessel prestimulation with different NE concentrations. Ach stimulus strength was held constant ( $Q_{IP3,ss} = 0.33$  nM/ms) and simulations were repeated for a weak ( $R_{gj}^{EC-SMC} = 13.5$  G $\Omega$ ) or a strong ( $R_{gj}^{EC-SMC} = 70$  M $\Omega$ ) myoendothelial coupling. NE prestimulation increases the EC  $Ca^{2+}$  spread but reduces  $V_m$  spread.

However, a value of 3.3 M $\Omega$  was estimated by Lidington et al. [155] for rat skeletal muscle. Based on this value, the predicted  $\lambda_{el}$  was in close agreement with the experimental  $\lambda_{el}$  value determined in guinea-pig small intestine arterioles [146], hamster feed arteries [164], and with dilatation data from RMA [81, 133]. After disruption of the endothelial gap junctions, the ability of the model vessel to carry spreading responses was minimized as indicated by a large decrease in  $\lambda_{el}$  (Table 3.3).

Myoendothelial gap junction resistance plays also an important role in the model's behavior. Sandow and Hill [96] provided an estimate for  $R_{\text{gj}}^{\text{EC-SMC}}$  in proximal RMA, based on morphological observations. A resistance value of 70 M $\Omega$  per gap junction and two gap junctions per SMC was reported (corresponding to 35 M $\Omega$  per SMC). The estimate of Yamamoto et al. [98] in guinea pig mesenteric arteries was significantly higher (i.e., 900 M $\Omega$  per single SMC). The incidence of myoendothelial gap junctions may vary between vascular beds and may even be significantly smaller in proximal rather than in distal RMA [96]. For these reasons a wide range of values were utilized in the model (i.e.,  $R_{\text{gj}}^{\text{EC-SMC}} = 70 - 13500$  M $\Omega$  cell to cell resistance or 4.7 - 900 M $\Omega$  total myoendothelial resistance per SMC).

In simulations utilizing high  $R_{\text{gj}}^{\text{EC-SMC}}$ , conduction of a signal initiated in SMCs was limited compared with a signal initiated in ECs (Figures 3.4C vs. 3.5E, F). Such differential electrical communication is consistent with responses seen and simulated in some vascular beds, for example in hamster feed arteries of the retractor muscle [135] and in [123]. Experimental data suggests however, that in RMA the endothelial and smooth muscle layers function as an electrical syncytium and  $V_m$  changes initiated in the ECs and SMCs are conducted similarly [81]. Thus, a value of  $R_{\text{gj}}^{\text{EC-SMC}}$  in the lower range of table 3.2 is more likely in RMA. Indeed, for  $R_{\text{gj}}^{\text{EC-SMC}}$  between 70 and 525 M $\Omega$  similar hyperpolarization/ depolarization appear away from the stimulus site regardless of whether the vessel is stimulated in the endothelium or smooth muscle side (at  $x = 2.5$  mm,  $|\Delta V_m| = \sim 3$  mV in Figures 3.4A, B and Figures 3.5B, D). However, even for low

$R_{gj}^{EC-SMC}$  there is a difference between stimulation in the two sides of the vessel wall. There is a significant local change in  $V_m$  when the current is injected in the SMC(s) that attenuates rapidly over the next few SMCs. This change is more pronounced if the same current is injected in a single versus an array of neighboring cells (Figures 3.5A-D), because in the latter case the effective resistance between the stimulus site and the endothelium is smaller.

### 3.4.2 Current vs. voltage clamp stimulations

Our simulation results are in agreement with model results presented by Diep et al. [123]. This earlier study investigated spreading responses after ECs or SMCs were clamped at a given  $V_m$  ( $|\Delta V_{m,max}| = 15$  mV), rather than current clamp used in the present study. Their model predicted that SM-initiated responses conducted poorly along the vessel, and a substantial voltage response in the endothelium could only be generated when a sufficient number of SMCs were clamped simultaneously. The authors attributed this behavior to poor coupling of the SMC with adjacent cells and their perpendicular orientation to the vessel axis. Our simulations using the same effective myoendothelial resistance (Figures 3.5E and F) show similar trends for SM-initiated responses. Our simulations, however, point out that a larger total injected current is required to clamp an EC versus a SMC or many versus few SMCs, to a given  $V_m$ . When the resistivity with neighboring cells is high, a large change in the  $V_m$  of the stimulated cell can be achieved with a relative small injected current (i.e., the current does not diffuse and causes a larger depolarization/hyperpolarization; Figure 3.5 A vs. 3.5 E). Thus, if the same  $V_m$  clamp is applied to an EC and a SMC, the injected current will be higher in the well coupled endothelium. The two studies combined suggest that distal responses are more sensitive

to the total current injected at the local site and less to the achieved membrane depolarization/hyperpolarization at the local site.

Both the current and the voltage clamp however introduce a bias in evaluating conduction when applied to cells with different gap junction connectivity. A voltage clamp will favor conducted responses in well coupled systems (i.e. a higher stimulating current is introduced). A current clamp will overestimate conduction in poorly coupled systems (i.e. by not accounting for the effect of  $V_m$  on agonist-induced transmembrane currents). Simulations presented in Figure 3.6 are independent of the bias introduced by the choice of the stimulation protocol (i.e., voltage or current clamp). Simulations of agonist-induced reactivity are physiologically more relevant and differ from both voltage and current clamps. They can also be utilized to predict how many cells need to be stimulated in vivo in order to produce an observable effect at distant sites. Simulations show that a saturating concentration of NE applied to three SMCs induces a small response away from the stimulus site (Figure 3.6A). The ability of the SM to initiate a conducted electrotonic signal increases as the myoendothelial coupling increases (Figure 3.6A vs. 3.6B) and when more SMCs are stimulated (Figure 3.6C vs. 3.6A). Interestingly, the local  $V_m$  response to NE depends significantly on the myoendothelial connectivity, and SMCs that are not well coupled produce significantly higher local depolarization to NE. Thus, as coupling *decreases*, the ability of the SMCs to generate a distant signal *decreases*, but the sensitivity of these cells to agonist stimulation locally *increases*.

In vascular beds where SMCs are not well coupled with neighboring ECs and SMCs, the stimulation of a few SMCs can produce large localized changes in arteriolar tone. On the other hand, stimulation of a number of ECs or SMCs has the potential to

generate spreading responses and regulate vasoactivity over larger vascular segments [123]. The physiological importance of the vessel's ability for SMC-initiated localized constriction needs to be further investigated. For example, what is the difference in the regulation of blood supply by a strong local constriction instead of a weaker spreading constriction over a larger vascular segment?

### **3.4.3 Physiological relevance of stimulatory protocols**

Figure 3.6 demonstrates that saturating concentrations of agonist can impose different levels of maximum depolarization depending on the homo- / hetero- cellular connectivity of the cells and the number of the stimulated cells. Thus, the physiological relevance of a voltage clamp stimulation protocol is difficult to assess and should be different in intact vessels from isolated cells. In isolated SMCs saturating NE concentration should depolarize  $V_m$  up to -40 to -30 mV and thus voltage clamps in that range are considered physiological for isolated SMCs. As the homo- and hetero-cellular coupling of the SMC with neighboring cells increases, the maximum physiological value should decrease. In addition, model simulations with saturating concentration of agonist in either layer reveal maximum transmembrane currents in the order of few 10's of pA (i.e. determined mostly by the maximum conductance of  $K_{Ca}$  channels in ECs and the NSC in SMCs). Since the level of homo- and hetero-cellular coupling affects agonist induced changes in  $V_m$ , the maximum transmembrane currents that occur in vivo will be affected as well. Thus, for both the voltage and the current clamp, the maximum physiological magnitude will depend on the connectivity of the stimulated cell.

These considerations suggest supra-physiological current injections per single EC in Figures 3.4 and 3.5 and potentially in the majority of experimental studies of conducted



vasoreactivity that utilize current injection in a single cell with intracellular microelectrodes. The use of a significant intracellular current injection (100's of pA) in experimental studies is necessary in order to evoke robust responses, e.g. 1 – 3 nA in vessels 25 - 60  $\mu\text{m}$  in diameter [146]. Similar total current is predicted by the model. Because of circumferential symmetry, in a vessel with 42  $\mu\text{m}$  diameter, 150 pA per EC will correspond to a total injected current of 3nA (approximately 20 ECs in the circumferential direction). Although such voltage clamps and current injections remain a useful experimental approach to characterize the electrical behavior of a vessel segment, this comparison suggests that in vivo, multiple cells need to be stimulated in order to generate a significant conducted response.

#### **3.4.4 Role of endothelial cell $\text{Ca}^{2+}$ spread**

In hamster feed arteries, the conduction of hyperpolarization was augmented during Ach stimulation compared to electric current stimulation [164]. This augmentation was indicated by an increase in the length constant from  $\lambda_{\text{el}} = 1.2 \text{ mm}$  to  $\lambda_{\text{el,Ach}} = 1.9 \text{ mm}$ . In the model, stimulation with Ach did not significantly increase the length constant, ( $\lambda_{\text{el}} \approx \lambda_{\text{el,Ach}} \approx 1.6 \text{ mm}$ ). This lack of facilitation was due to limited endothelial  $\text{Ca}^{2+}$  spread following Ach stimulation (Figures 3.7 and 3.8 B). However, the limited but considerable Ach-induced  $\text{Ca}^{2+}$  spread amplified significantly the hyperpolarization at the local and distant sites. Elevation of  $\text{Ca}^{2+}$  in ECs near the stimulation site activates  $\text{SK}_{\text{Ca}}$  and  $\text{IK}_{\text{Ca}}$  channels, which contribute to the total current generated at the local site. Because the maximum current generated by individual cells is limited, EC  $\text{Ca}^{2+}$  spread increases the ability of focal stimuli to induce conducted response with physiologically relevant magnitude. The amplification of the current is approximately equal to the ratio of the

distance of  $\text{Ca}^{2+}$  spread to the length of the stimulation site. In the simulations, inhibition of EC  $\text{IP}_3$  and  $\text{Ca}^{2+}$  spread impaired the SMC relaxation (Figure 3.8 *A*) by reducing local hyperpolarization from 10.7 mV to 3 mV. EC  $\text{Ca}^{2+}$  spread can also increase the number of  $\text{BK}_{\text{Ca}}$  channels in SMCs activated by the NO/cGMP pathway (Figure 3. 1), and further enhance the total hyperpolarizing current. However, this may have a small effect on the relaxation in the presence of strong EDHF, and negligible NO effects on conducted responses have been reported in RMAs [165].

The predicted endothelial  $\text{Ca}^{2+}$  spread agrees with experimental studies on RMAs [81, 165] and certain other vessel types [134, 138, 166]. For example, Figure 3.5 in [81] shows that a noticeable EC  $\text{Ca}^{2+}$  increase appears only within a distance of 500  $\mu\text{m}$  from the Ach stimulation site. On the other hand, studies in other vessels reported significant NO- and EDHF-dependent components of the conducted response and suggested EC  $\text{Ca}^{2+}$  increase at remote sites [135, 142, 145, 167]. These findings have been challenged by others [166, 168]. Recently distant EC  $\text{Ca}^{2+}$  waves were observed in hamster feed arteries [143, 144] and transgenic mice cremaster muscle arterioles [139]. Our simulations do not negate the possibility of different signal transduction mechanisms in spreading responses in various vessel types.

#### **3.4.5 $\text{IP}_3$ -mediated $\text{Ca}^{2+}$ spread vs. direct inter endothelial $\text{Ca}^{2+}$ diffusion**

The mechanism responsible for the generation of a propagating  $\text{Ca}^{2+}$  wave along the endothelium remains unclear. In the model, the limited yet noticeable endothelial  $\text{Ca}^{2+}$  spread was mediated by axial  $\text{IP}_3$  diffusion, and subsequent  $\text{Ca}^{2+}$  release from the stores. The relative importance of  $\text{IP}_3$  and  $\text{Ca}^{2+}$  diffusion depends on the assumed values for the gap junction permeability's of the two species ( $\rho_{\text{IP}_3}^{\text{EC-EC}}$  and  $P_{\text{Ca}}^{\text{EC-EC}}$ ). These

parameters have not been experimentally determined and previous theoretical studies have used arbitrary values. In this study,  $P_{Ca}^{EC-EC}$  was inversely related to  $R_{gj}$  (Eq. 3.3).

For the control value of  $R_{gj}$ , direct  $Ca^{2+}$  diffusion ( $< 0.04$  pA in 9 C) was much smaller compared to other transmembrane  $Ca^{2+}$  fluxes ( $\sim 1$  pA) and thus had a negligible effect on the global  $[Ca^{2+}]_i$ .  $P_{Ca}^{EC-EC}$  has to increase 100-fold to result in noticeable direct  $Ca^{2+}$  spread, but even then it was limited to 400  $\mu m$  (Figure 3.8 B). The predicted contributions of  $IP_3$  and  $Ca^{2+}$  agree with the experimental data which indicate that direct  $Ca^{2+}$  communication via homocellular gap junctions is not essential for  $Ca^{2+}$  waves [169]. Some theoretical models of  $IP_3$ -mediated intercellular  $Ca^{2+}$  waves have assumed negligible direct intercellular  $Ca^{2+}$  diffusion [170, 171]. In mice cremaster muscle arterioles,  $Ca^{2+}$  waves were significantly faster than can be accounted for by the diffusion of  $IP_3$  or  $Ca^{2+}$ , suggesting an underlying active mechanism (e.g., a regenerative release of  $IP_3$  triggered by Ach [139]).

### 3.4.6 Effect of intercellular and transmembrane potential gradients

Inhibition of endothelial  $K_{Ca}$  channels unmasked  $Ca^{2+}$ -dependent slow-conducted vasodilatation in hamster feed arteries [143]. We used the model to examine if blocking conducted hyperpolarization can facilitate direct  $Ca^{2+}$  waves along the vessel axis and tested the hypothesis that the physiological  $V_m$  gradient inhibits longitudinal  $Ca^{2+}$  diffusion. The predicted intercellular  $V_m$  gradients (Figure 3. 9) agree with experimental recordings [81]. Near the stimulation site the electrical field across the gap junctions had a minimal effect on the  $Ca^{2+}$  spread and the  $Ca^{2+}$  concentration gradient was the major determinant of a rather limited intercellular  $Ca^{2+}$  flux. The electrical field becomes dominant only far away and can reverse the diffusion of  $Ca^{2+}$  in a direction towards the

stimulus site. The magnitude of this electrically driven intercellular  $\text{Ca}^{2+}$  flux is minimal and cannot affect  $[\text{Ca}^{2+}]_i$ .

In some EC types, hyperpolarization itself can increase  $[\text{Ca}^{2+}]_i$  by increasing the driving force for  $\text{Ca}^{2+}$  entry [19, 172]. Therefore, it was speculated that conducted hyperpolarization could trigger  $\text{Ca}^{2+}$  transients that can activate NO release and dilate the vessel at distant sites [142]. However, there is no direct evidence for the existence of such mechanism in spreading responses. It is also not clear if such hyperpolarization-induced  $\text{Ca}^{2+}$  changes would be adequate for distant dilatation [166]. We have previously investigated the controversial effect of  $V_m$  on  $[\text{Ca}^{2+}]_i$  in the isolated EC model [78] and showed that resting and plateau  $\text{Ca}^{2+}$  levels were rather insensitive to  $V_m$  changes. The magnitude of hyperpolarization associated with conducted responses in the model could not elicit a large  $\text{Ca}^{2+}$  transient. Consequently, conducted hyperpolarization did not trigger an endothelial  $\text{Ca}^{2+}$  wave and did not induce NO release, activation of  $\text{SK}_{\text{Ca}}$  and  $\text{IK}_{\text{Ca}}$  channels or facilitated spreading responses.

### 3.4.7 Effect of stimulus strength

Simulation results (Figure 3. 10) indicate that the length constants of the  $\text{Ca}^{2+}$  and  $V_m$  spread may depend on the concentration of the applied agonist or the presence of other stimuli. These effects cannot be predicted in simplified cable models. The cable length constant depends on axial and radial resistances. Thus, it can be modulated by agents that change the gap junction and cell membrane resistances. In the model, prestimulation with NE reduced  $\lambda_{\text{el,Ach}}$  by opening NSC channels and reducing SM membrane resistance (Figure 3. 10 B). Haug and Segal [148] reported that activation of  $\alpha_1$ - and  $\alpha_2$ -adrenoceptors in feed arteries of the hamster retractor muscle inhibits

conducted vasodilation. Using a cable model, they also showed that decreased SM membrane resistance or increased myoendothelial resistance could account for the inhibition. Gustafsson and Holstein-Rathlou [173] showed experimentally that angiotensin II increased the electrical length constant in RMA. They hypothesized that this was a result of increased cell-to-cell coupling or membrane resistance. Increased membrane resistance could result from agonist-induced inhibition of potassium channels in SMCs, but this mechanism was not incorporated into the model due to lack of appropriate direct experimental evidence. Our data suggests that SM prestimulation can significantly affect the radial resistivity of a vessel which in turn can alter the observed distance of electrical conduction.

Experimentation with hamster feed arteries led Uhrenholt et al. [144] to hypothesize that SM tone could increase basal EC  $[Ca^{2+}]_i$  and sensitize the endothelium for  $Ca^{2+}$  wave propagation. A similar phenomenon was observed in the model by an increase in the length constant of the EC  $Ca^{2+}$  spread following SM prestimulation (Figure 3.10A). NE prestimulation generated  $IP_3$  in the SM, which diffused to the ECs. The presence of a basal, subthreshold concentration of  $IP_3$  sensitized the endothelium to  $IP_3$  and Ach. This is due to the nonlinearity of store  $Ca^{2+}$  release (i.e.,  $Ca^{2+}$  released from the stores is a sigmoidal function of  $IP_3$  concentration). Following NE stimulation and EC sensitization, the same concentration of Ach induces a larger  $Ca^{2+}$  response and an  $IP_3$ -dependent  $Ca^{2+}$  wave with a larger  $\lambda_{Ca}$  (Figure 3.10A, *solid line*). Even imposing the same increase in  $IP_3$  at the local site gives a more dramatic  $Ca^{2+}$  increase in neighboring cells (sensitized by prestimulation). The result is an  $IP_3$ -dependent  $Ca^{2+}$  wave with a larger  $\lambda_{Ca}$  in the presence of NE (Figure 3.10A, *dashed line*). Figure 3.10 A also indicates that at a

given NE concentration,  $\lambda_{Ca}$  increases with stronger Ach stimulation. On the other hand, the electrical length constant,  $\lambda_{el,Ach}$ , does not depend on the concentration of the stimulating agent (i.e., Ach) (data not shown), indicating that the vessel can be approximated from an electrical point of view as a linear cable.

### **3.4.9 Spread of relaxation**

The model does not include at this stage a description for  $Ca^{2+}$ -induced force development and for the resulting changes in vessel diameter. Assuming that constriction and relaxation are proportional to  $Ca^{2+}$  changes in the smooth muscle, a preliminary comparison can be made between our simulation results and experimental data on spreading relaxations. SMC  $Ca^{2+}$  profiles predicted by the model and the actual relaxation profile obtained from RMA [81] show significant responses at distances 1.5 mm away from the stimulus site. The mechanical/dilatation length constant - determined by fitting an exponential to diameter changes - is typically between 1 and 2 mm, depending on the vessel type [133]. The model gives SM  $Ca^{2+}$  and hyperpolarization profiles with length constants in the range of 0.9 - 1.6 mm (Figure 3.10), depending on the NE prestimulation level.

### **3.5 Model limitations**

The model captures the major aspects of conducted responses in RMA and makes predictions about the parameters that can affect the transmission of information along the vessel. However, the study does not account for behavior seen in other vessels, such as  $Ca^{2+}$  waves over considerably greater distances and spreading vasodilation in the absence of change in  $V_m$ . The simulation results do not negate these experimental findings, and they suggest different type and expression levels of ion channels and  $Ca^{2+}$  handling

machinery in those vessels. Spreading vasoreactivity depends also on vessel size. Single and multiple layers of SMCs were incorporated into the model to simulate arterioles and resistance arteries, but quantitative information for the subcellular components at each vessel size is not available.

The predictions are further limited by the uncertainty in a number of parameter values and by a number of simplifying assumptions. The EC length depends on the vessel type and size and a representative value was chosen for this study. More general predictions can be made if the reported distances are normalized with respect to the assumed EC's length. The assumed arrangement of ECs may also influence spreading responses. ECs may overlap and form tortuous conduction pathways. The assumed circumferential symmetry and the regular end-to-end EC coupling may lead to an overestimate of the length constants. (Notice however that the overlapping arrangement of ECs is equivalent to the serial arrangement (both depicted in Figure 3.2) if no current is leaking from the endothelium). Circumferential heterogeneity would also arise from coupling each SMC to different underlying ECs, and it was reported that on average only two ECs are coupled to the same SMC [96]. In [123] this was simulated by randomly connecting each SMC with two out of 16 underlying ECs. However, this heterogeneity in the myoendothelial coupling should have a negligible effect on axial signaling. The number of ECs coupled to each SMC was accounted for in this model by distributing the total gap junction permeability equally to all the underlying cells in contact.

The  $R_{gj}^{EC-EC}$  is a critical parameter for conducted responses, and has not been determined in RMA. Simulation results suggest  $R_{gj}^{EC-EC}$  close to the lower end of

previously reported values. The permeability of gap junctions to  $IP_3$  is not known. In this study,  $p_{IP_3}^{EC-SMC}$ ,  $p_{IP_3}^{EC-EC}$  and  $p_{IP_3}^{SMC-SMC}$  were assumed to be inversely proportional to  $R_{gj}^{EC-SMC}$ ,  $R_{gj}^{EC-EC}$  and  $R_{gj}^{SMC-SMC}$ , respectively. In an earlier study,  $p_{IP_3}^{EC-SMC} = 0.05 \text{ s}^{-1}$  and  $R_{gj}^{EC-SMC} = 900 \text{ M}\Omega$  per SMC were assumed and the same product for these two values was maintained here. Although this parameter does not directly affect the axial communication, the excessive myoendothelial  $IP_3$  diffusion at larger  $p_{IP_3}^{EC-SMC}$  may indicate that the  $p_{IP_3} \times R_{gj}$  product and/or the EC and SMC models are inaccurate.

Limitations in the isolated EC and SMC models have been discussed previously [56, 78]. Uncertainty in parameter values and the absence of spatial resolution in the EC and SMC models present two of the most serious limitations. Parameters that affect transmembrane currents in particular can have an impact on predictions regarding passive and facilitated conduction, while parameters affecting the intracellular balance of  $IP_3$  and  $Ca^{2+}$  can determine the predicted  $Ca^{2+}$  spread. The lack of subcellular resolution may be acceptable from the electrical point of view (real cells are essentially isopotential), but the intercellular  $Ca^{2+}$  waves may depend on spatial distribution of RyRs and/or  $IP_3$ Rs and  $Ca^{2+}$ -induced  $Ca^{2+}$  release from the SR along the cells. A multicellular SM model with intracellular  $Ca^{2+}$  waves was proposed recently to study synchronization [126], but the development of EC and SMC models with  $Ca^{2+}$  waves, sparks, or pulsars is restricted by the absence of relevant tissue-specific parameter values.

### 3.6 Conclusions

A computational model of a vessel segment was developed to investigate spreading responses in RMAs and arterioles. The study advances previous theoretical



work by using detailed models of EC and SMC and by accounting for changes in the concentration of intracellular species. Simulation results corroborate experimental findings that spreading vasorelaxation in RMAs mainly reflects  $\text{Ca}^{2+}$ -independent, passive conduction of hyperpolarization along the endothelium. The model predicts that intercellular  $\text{IP}_3$  diffusion is more important than direct intercellular  $\text{Ca}^{2+}$  diffusion and it can play a role in modulating spreading responses. Endothelial  $\text{IP}_3$  diffusion mediated limited but significant  $\text{Ca}^{2+}$  spread that amplified total current generated at the local site. The length constant of voltage or  $\text{Ca}^{2+}$  propagation depends on the presence and concentrations of stimulating agonists. Simulations demonstrate that intercellular uncoupling attenuates conducted responses but sensitizes cells to local agonist and electrical stimuli. Voltage clamp is a more appropriate experimental analogue of local agonist stimulation in cells that are weakly coupled and current clamp in cells that are well coupled. Overall, the mechanisms that modulate conducted vasoreactivity are complex and are often difficult to assess using a reductionist approach and qualitative syllogisms. The development of detailed computational models holds promise for the elucidation of nonlinear interactions between system components and their potential effect on signal transmission.

## Chapter 4: Myoendothelial Projections

This chapter is to be submitted (with slight modifications) as

Nagaraja,S., A.Kapela, D.G.Welsch and N.Tsoukias, 2011, “Role of myoendothelial projections in feedback response: a theoretical study.” (Manuscript completed, to be submitted)

Abstract:

The theoretical study presented investigates the role of endothelial projections or microprojections (MPs) in EC feedback response to SMC stimulation. A previously developed compartmental EC-SMC model is modified to include MPs as subcellular compartments in the EC. The model is further extended into a 2D continuum model using a FEM approach and electron microscopy images to account for MP geometry. The SMC and EC MP compartments are coupled via nonselective MEGJs and allow exchange of  $\text{Ca}^{2+}$ ,  $\text{K}^+$ ,  $\text{Na}^+$  and  $\text{Cl}^-$  ions and  $\text{IP}_3$ . Models take into consideration recent evidence showing localization of  $\text{IK}_{\text{Ca}}$  and  $\text{IP}_3\text{Rs}$  in MPs. SMC stimulation caused an  $\text{IP}_3$  mediated high  $\text{Ca}^{2+}$  transient in the MPs whose global spread was rather limited. A hyperpolarizing feedback generated by the localized  $\text{IK}_{\text{Ca}}$  channels was transmitted to the SMCs via MEGJs.  $R_{\text{gj}}$  and the density of  $\text{IK}_{\text{Ca}}$  and  $\text{IP}_3\text{R}$  in the projection influence the extent of EC response to SMC stimulation. The predicted feedback response also depended on the volume and geometry of the MP. MPs are required to amplify the SMC initiated signal in the myoendothelial feedback response during SMC stimulation. Simulations suggested that the  $\text{Ca}^{2+}$  transient responsible for feedback generation was mediated by  $\text{IP}_3$  rather than  $\text{Ca}^{2+}$  diffusion and that a localized rather than a global EC  $\text{Ca}^{2+}$  mobilization was more likely following SMC stimulation.

Keywords: myoendothelial feedback, myoendothelial projections, feedback, calcium, IP<sub>3</sub> receptors, IK<sub>Ca</sub>

#### **4.1 Introduction**

MPs are cellular extensions from EC and /or SMC that extend into the internal elastic lamina (IEL) (Figure 4.1C) [114, 174]. MPs vary both in number and size among different vascular beds, age, species, sex and diseased states of animals [83]. The number of MPs has been shown to increase with decrease in vessel size, a feature synonymous with EDHF activity [83, 175]. In spite of their early discovery in 1957 [176], a clear role for MPs remains to be defined. Recent experiments regarding the functional characteristics of MPs suggest that they might be involved in a local feedback mechanism from EC to SMC. Immunohistochemical labeling studies show localization of IP<sub>3</sub>Rs (Figure 4.1B), IK<sub>Ca</sub> (Figure 4.1A) and MEGJs in these MPs [93, 119, 174, 177, 178].

Global and/or local Ca<sup>2+</sup> events [80, 117-119, 121, 122] have been reported in ECs following SMC stimulation and are attributed to the initiation of myoendothelial feedback. Furthermore, the local spontaneous as well as agonist initiated local Ca<sup>2+</sup> events like “pulsars” and “wavelets” have been shown to occur in and around the MPs [117, 119, 120]. Current studies are focused on identifying the major source and propagation of these SMC initiated Ca<sup>2+</sup> events in EC. As myoendothelial coupling is much weaker than homo cellular coupling (which is reflected in the high myoendothelial resistances reported in literature (900MΩ), simple intercellular fluxes of Ca<sup>2+</sup>/IP<sub>3</sub> are unlikely to cause significant Ca<sup>2+</sup> events. However, localized IP<sub>3</sub>Rs in MPs can be activated even by a small amount of IP<sub>3</sub> entering from the stimulated SMC, leading to rapid release of Ca<sup>2+</sup> from the ER stores leading to local Ca<sup>2+</sup> increase observed in the

MPs. [119, 174, 178]. This  $\text{Ca}^{2+}$  transient can activate nearby  $\text{IK}_{\text{Ca}}$  channels and cause hyperpolarization of MP which is transmitted back as feedback to the overlying SMCs via MEGJs (Figure 4.1D).

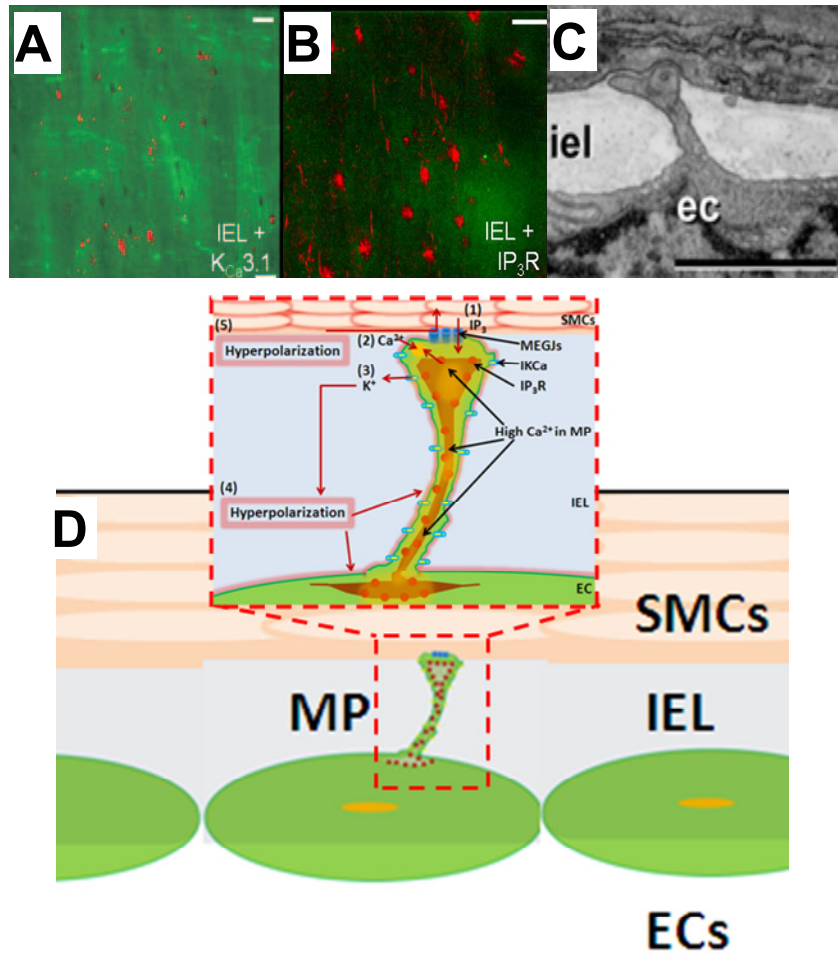


**Figure 4.1:** Figure shows experimental characterization and related hypothesis for the functional presence of MPs. Immunohistochemical labeling study results in rat mesenteric artery showing localization of A)  $\text{IK}_{\text{Ca}}$ , B)  $\text{IP}_3\text{R}$  channels on the projection [119] and C) electron microscopy images of the projection in rat saphenous arteries [87]. D) Hypothesis based on experimental findings suggesting a role for  $\text{IP}_3$  entering the projection during SMC stimulation.

Despite significant experimental efforts in this area, no unified conclusion has been reached regarding the role of MPs because of variation in experimental setups (tissues, species, agonists, techniques) and the lack of a (concrete/theoretical) framework. Mathematical modeling can be a useful tool analyze experimental data and elicit

signaling mechanisms. Models offer a quantitative as well as qualitative assessment of intra and inter cellular fluxes, feedback response under a host of different conditions with assumptions based on experimental findings.

Few theoretical studies have investigated EC-SMC interactions or the presence of local signaling domains inside the EC. In our previously developed EC-SMC model, [129] we integrated our detailed single EC [78] and SMC [56] models with electrical, chemical and NO coupling pathways as described in section 2.4.2. We have extended our EC-SMC model to incorporate a separate compartment within the EC to simulate the presence of MPs (Figure 4.2a). We also developed a 2D finite element method (FEM) model with MPs (Figure 4.3a) to account for spatial localization of  $I_{K_{Ca}}$  and  $IP_3Rs$ . The current models provide theoretical insights into the possible roles of MPs. Facilitation of feedback in terms of SMC  $V_m$  following SMC stimulation appears to be the most prominent role for MPs under the assumed conditions. These models provide a basis for development of future models with the inclusion of MPs in both EC and SMC in normal as well as diseased states where the morphology and number of these MPs have been found to be different [83].

## **4.2 Model development:**

### **4.2.1 Compartmental model**

The current model was based on our previously developed two cell EC-SMC model [129]. The EC was divided into two compartments representing the bulk EC and the MPs as shown in Figure 1a. For most parameters, experimental data obtained from rat mesenteric arteries was used. Where mesenteric data was unavailable, data from other cell types like cardiac, vascular and cerebral rat arteries have been used or we have

assumed physiologically relevant values. In some cases parametric studies were performed to determine influence of certain parameters on model responses.

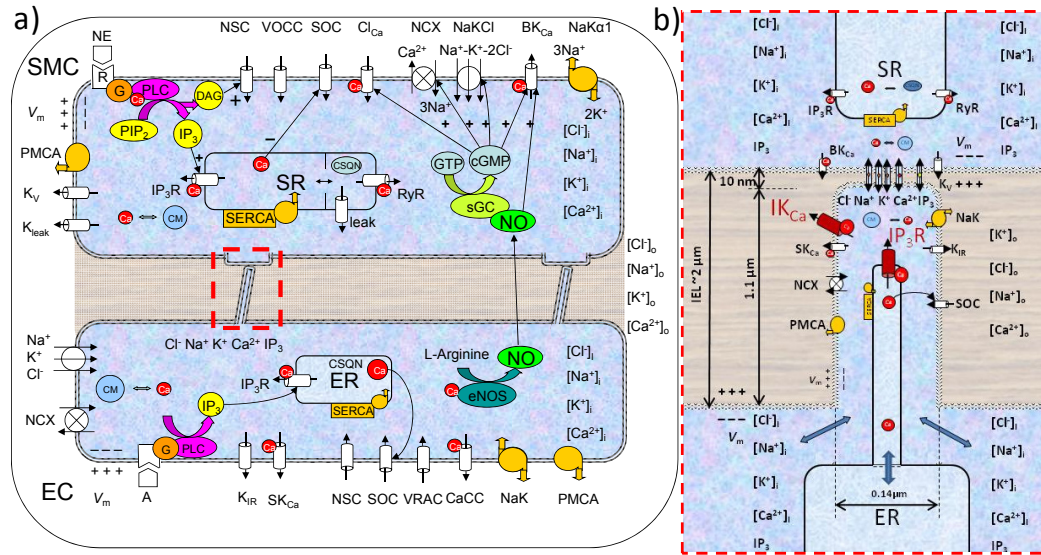


**Figure 4.2 a) Model schematic showing all the channels and pumps incorporated in the EC MP compartmental model. b) Schematic showing the dimensions of the EC microprojections (MP). Blue double sided arrows represent areas of diffusion between the MP and bulk EC compartment.**

**a) Geometric Parameters:** Figure 4.2b shows the dimensions of the EC MPs used in the model. The length and width of MPs were taken from electron microscopy images of rat mesenteric artery by Sandow et al. [174]. The number of MEGJs per endothelial cell has been characterized to be 2.7 by Dora et al. [93]. As MEGJs are localized on MPs, we assumed the number of MPs to be equal to number of MEGJs assuming every projection contains one GJ. The average cell volume of an endothelial cell is approximately 1pL [77]. The total EC volume was divided into bulk EC volume and MP volume. MP volume was calculated by assuming the MP to be cylindrically shaped with dimensions as shown in Figure 4.2b. Membrane area, whole cell capacitance as well as the ER/SR was divided between the two compartments using the ratio of volume of each compartment to the total volume of EC. This allows for appropriate division of

membrane fluxes between the two compartments. Therefore, in all calculations, the total cell volume, capacitances, surface areas and whole cell currents remained the same as in EC-SMC model.

b) Ionic channel distributions: The schematic of our model is shown in Figure 4.2a. The whole cell conductance of the channels and pumps was maintained the same as in the EC-SMC model. The following channels are uniformly distributed across the membrane of EC:  $K_{ir}$ , nonselective cation channel (NSC),  $SK_{Ca}$ , SOC, calcium activated chloride channel (CaCl),  $NaK_{\alpha 1}$ , NCX, PMCA, sarco(endo)plasmic reticulum  $Ca^{2+}$ -ATPase (SERCA) are The following channels are uniformly distributed across the membrane of SMC: voltage dependent L-type calcium channel (VOCC),  $K_v$ , NSC, ATP activated potassium channel ( $K_{ATP}$ ),  $BK_{Ca}$ , SOC, CaCl, NCX, PMCA pump,  $NaK_{\alpha 1}$ , and SERCA are uniformly distributed across the SMC membrane.  $IK_{Ca}$  [93, 119, 174, 177, 179] and  $IP_3R$  [119, 174, 178] are localized to MPs as shown in Figure 1b. Maximum conductance of  $IK_{Ca}$  channel (eGIKCa in the model) has been experimentally characterized in porcine arteries by Bychkov et al. [180], rescaled using rat mesenteric data and implemented in our EC model [78].  $IK_{Ca}$  are localized in MPs by modifying this parameter as listed in Table 4.1. Ten percent of the  $IP_3R$ s are localized inside the MPs and the remaining 90% are uniformly distributed in the bulk of EC.  $IP_3R_{max}$  represents the  $IP_3R$  current at maximum conductance and was used to control this distribution. Most MEGJs are present on the MPs [91, 96]. Permeability of gap junctions is calculated based on the total MEGJ resistance ( $R_{gj}$ ) between an endothelial and SMC cell experimentally estimated in literature [98]. MEGJ are assumed to be non-selective to  $Na^+$ ,  $K^+$ ,  $Ca^{2+}$ ,  $Cl^-$  ions and  $IP_3$ . The EDRF/NO pathway was blocked for all simulations unless mention otherwise.

c) Coupling between MPs and bulk EC: diffusion currents: We have used a simple diffusion equation to describe the flux of the four ions and IP<sub>3</sub>. The Eqs 4.1 and 4.2 incorporate V<sub>m</sub> as well as concentration difference dependence in these two compartments:

EC ions and IP<sub>3</sub>:

$$I_S = \frac{z_S \times F \times D_S \times A_{mp} \times N_{mp}}{L_{mp}} \left( ([S]_{bulk} - [S]_{mp}) + \frac{z_S \times F \times ([S]_{bulk\ ec} + [S]_{mp})}{2 \cdot R \cdot T} (V_{m,bulk} - V_{m,mp}) \right) \quad (4.1)$$

$$I_{IP3} = \frac{D_{IP3} \times A_{mp} \times N_{mp}}{L_{mp}} ([IP_3]_{bulk\ ec} - [IP_3]_{mp}) \quad (4.2)$$

Where 'S' represents Na<sup>+</sup>, K<sup>+</sup>, Ca<sup>2+</sup> and Cl<sup>-</sup>. V<sub>m</sub> is the membrane potential. Suffixes 'mp' and 'bulk' represent the MP and bulk compartments in EC. A parameter was 'fl' was used to control the amount of diffusion between the two compartments. Its control value was 1.75. The values for the rest of the parameters and their description are listed in Table 4.1. The ER in either compartment was coupled using diffusion equation for Ca<sup>2+</sup> transport within the ER as shown in Eq.4.3

$$I_{diff} = z_{Ca} \times F \times D_{Ca} \times A_{mp} \times N_{mp} \frac{([Ca]_{s\ bulk} - [Ca]_{s\ mp})}{L_{mp}} \quad (4.3)$$

Where Ca<sub>s</sub> is the concentration of Ca<sup>2+</sup> in the ER stores. The remaining parameters and their description are listed in Table 4.1.

d) Numerical methods: The equations describing EC and SMC behavior are described in detail in previous studies [56, 78]. The compartmental model EC and SMC are implemented using 40 and 26 differential equations respectively. Unless mentioned otherwise (Table 4.1), the parameter values remain unchanged from the previous EC-



SMC model. The equations are coded in Fortran 90 and solved numerically using Gear's backward differentiation formula method for stiff systems (IMSL Numerical Library routine). The maximum time step was 1ms and the tolerance for convergence was 0.0005.

| <i>Parameter</i> | <i>Value</i>  | <i>Description</i>                         |
|------------------|---|--|
| $eG_{IKCa}$      | Bulk EC: 0.0nS<br>MP: 1.72 nS [129]                                 | Maximum $IK_{Ca}$ channel conductance      |
| $IP_3R_{max}$    | Bulk EC: $1.053 \times 10^3$ pA/mM<br>MP: $0.117 \times 10^3$ pA/mM | Maximum current through $IP_3R$            |
| $D_{Ca}$         | $300 \mu m^2/s$ [181]   | Diffusivity of free calcium in cytosol     |
| $D_K$            | $744 \mu m^2/s$ [171]   | Diffusivity of potassium in cytosol        |
| $D_{Na}$         | $505 \mu m^2/s$ [171]   | Diffusivity of sodium in cytosol           |
| $D_{Cl}$         | $900 \mu m^2/s$ [171]   | Diffusivity of chloride in cytosol         |
| $D_{IP_3}$       | $283 \mu m^2/s$ [181]   | Diffusivity of $IP_3$ in cytosol           |
| $A_{mp}$         | $0.0154 \mu m^2$ [96]   | Area of a single MP (radius $0.07 \mu m$ ) |
| $L_{mp}$         | $3.5 \mu m$ [96]  | Length of diffusion from MP to bulk EC     |
| $N_{mp}$         | 2.7 [93]  | Number of MEGJ/ EC                         |
| F                | 96487.0 C/mol   | Faraday constant                           |
| R                | 8341 mJ/ (mol $\times$ K )  | Universal gas constant                     |
| T                | 293 K   | Temperature                                |

|               |   |  |
|---------------|---|--|
| $Z_K, Z_{Na}$ | 1   | Ion valence of $K^+$ and $Na^+$  |
| $Z_{Ca}$      | 2   | Ion valence of $Ca^{2+}$   |
| $Z_{Cl}$      | -1  | Ion valence of $Cl^-$  |
| f1            | Control: 1.75,<br>No MP scenario: $1.75 \times 10^{-3}$ | Factor controlling degree of diffusion between MP and bulk EC in compartmental model |

**Table 4.1: List of parameters describing dimensions of MPs and microdomains along with values of diffusion constants of ions and  $IP_3$  in the cytosol.**

#### 4.2.2 Finite element method (FEM) model

The calculation of flux between two unequal compartments (MP and bulk EC) needs to take into account the difference in area and length of diffusion, boundary fluxes, <sup>a)</sup> buffering of  $Ca^{2+}$  and <sup>b)</sup> degradation of  $IP_3$  which is a complex process. In the compartmental model, we had to make certain assumptions for surface area and length of diffusion between the bulk EC and MP compartments. We developed a FEM model to study the spatial gradients of  $Ca^{2+}$  inside the EC MP and to better characterize the diffusion from the MP to the bulk EC. A 2D model also allowed for import of MP images from experimental studies and also account for spatial localizations of  $IK_{Ca}$  and  $IP_3Rs$  in the MPs. The model was developed using the chemical engineering module of COMSOL. EC and SMC were represented as rectangular structures with the dimensions as shown in Figure 4.3a. The model implemented only half of the EC and SMC. The results in the remaining half are assumed to be symmetrical. The shape of the projection was imported from experimental electron microscopy images of the projection in rat mesenteric arteries by [174]. Volume of MP was calculated assuming the MP to be cylindrical with diameter and length as shown in Figure 4.3b.

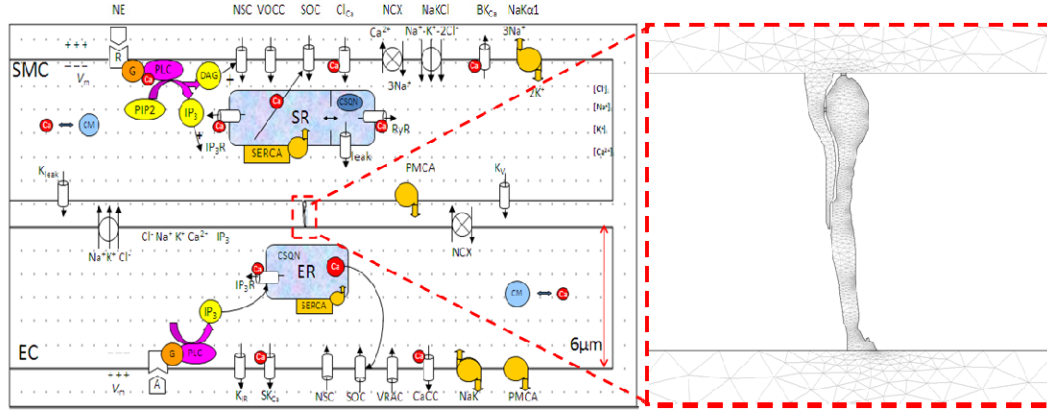


**Figure 4.3 2D FEM. a)** shows the model geometry with SMC, EC as rectangular segments with a microprojection whose shape is imported from an electron microscopy image by Sandow et al. Ion channel currents are uniformly distributed along the top and bottom boundaries of each cell. **b)** shows the EC projection with finite element mesh.  $IK_{Ca}$  channels and  $IP_3R$ s are localized in the microprojection.

Two rectangular domains connected the SMC and EC MPs to represent MEGJs. Nernst-Planck equation (Eq. 4.4) was used describe the motion of ions in the EC, SMC and MEGJ domains.

$$\frac{\partial C_i}{\partial t} + \nabla \cdot (-D_i \times \nabla C_i) - (z_i \times u_i \times F \times C_i \times \nabla V + C_i \times u) = R_i \quad (4.4)$$

Where ‘ $C_i$ ’ represents the concentration four ions ( $Ca^{2+}$ ,  $K^+$ ,  $Na^+$ ,  $Cl^-$ ),  $D_i$  represents their respective intracellular diffusivities,  $\nabla V$  and  $\nabla C_i$  are the respective  $V_m$  and ionic concentration derivatives of the 4 ions with respect to 2D spatial coordinates ‘x’ and ‘y’ and ‘u’ represents convective flux which was zero in our model.

Diffusion of  $IP_3$  and ER/SR  $Ca^{2+}$  as well as buffered  $Ca^{2+}$  was implemented using simple diffusion equations inside the EC, SMC and MEGJ (only for  $IP_3$ ).

$$\frac{\partial C_i}{\partial t} + \nabla \cdot (-D_i \times \nabla C_i) = R_i \quad (4.5)$$

where ‘ $C_i$ ’ is concentration of  $IP_3$  and the remaining quantities are the same as in Eq.4.4 with respect to  $IP_3$ . Membrane currents are defined under flux boundary conditions across the top and bottom boundaries of the EC and SMC. The left and right boundaries of the

cells are insulated. Whole cells currents are calculated in the same way as in the compartmental model. The currents are divided between the MP and bulk EC by ratio of volume of MP/ bulk EC to total volume of EC which was maintained the same as in the compartmental model. The current density at each boundary was determined by its respective surface area. PIP2, DAG and G protein are described by an embedded weak boundary equation.  $900\text{M}\Omega$  was used as control  $R_{\text{gj}}$  unless stated otherwise. 10%  $\text{IP}_3\text{R}$  and 100%  $\text{IK}_{\text{Ca}}$  localization in the MP are used in the control model. Localization of  $\text{IP}_3\text{R}$  and  $\text{IK}_{\text{Ca}}$  in the FEM model was done using the same parameters as in the compartmental model ( $\text{IK}_{\text{Ca}}$  conductance and  $\text{IP}_3\text{R}$  max). Differences in height of the EC and the MPs have been accounted for by appropriate scaling of fluxes at the boundaries between MEGJ and MP and at boundary between MP and bulk EC using the current and flux discontinuity condition (See Appendix 2). The equations were solved using the SPOOLES direct solver with absolute and relative tolerance of  $10^{-3}$  and  $10^{-2}$  respectively. The solution time was 30s with a time stepping of 0.1 s. The model geometry was divided into a total of 1025 (Sandow et al. figure) and 880 (Herberlin et al. figure) elements and solved for approximately 20000 degrees of freedom. Unless stated otherwise, the NO pathway was blocked.

## **4.3 Results**

### **4.3.1 Global vs. local $\text{Ca}^{2+}$ and $\text{IP}_3$ changes**

Figure 4.4 shows global as well as MP  $\text{Ca}^{2+}$  and  $\text{IP}_3$  transients during SMC and EC stimulation. Ach stimulation of bulk EC compartment increases the EC  $\text{Ca}^{2+}$  concentration as observed experimentally [80, 122, 182].

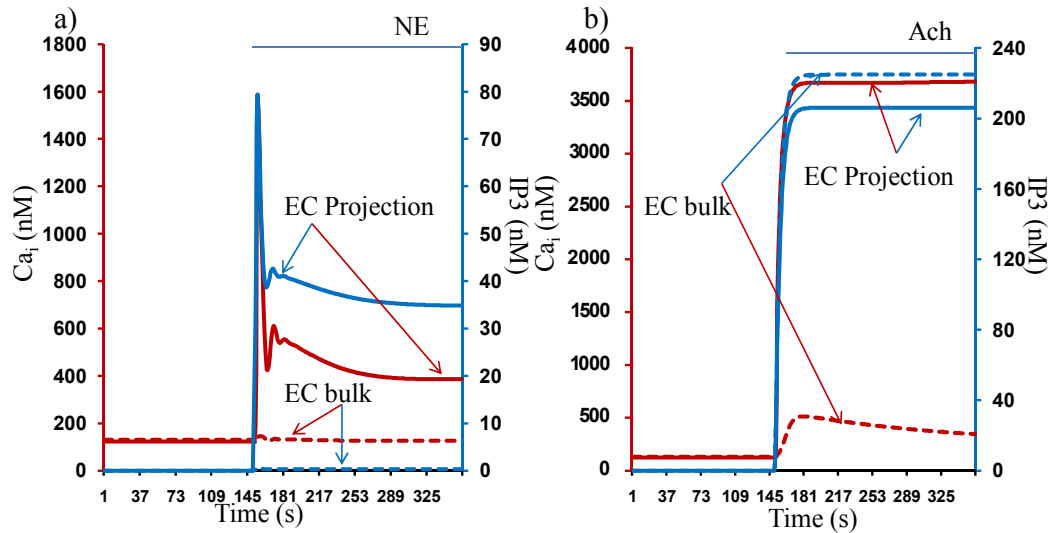


**Figure 4.4** Compartmental model results showing  $\text{Ca}^{2+}$  (red lines) and  $\text{IP}_3$  (blue lines) concentration in the EC microprojection (solid lines) and EC bulk (dashed lines) during  $1\mu\text{M}$  NE stimulation of SMC (a) at 150s and Ach stimulation of EC (b) at 150s. MEGJ resistance is maintained as  $900\text{ M}\Omega$  with restricted diffusion between the projection and bulk EC. 10% of  $\text{IP}_3\text{R}$  receptors are concentrated in the MP compartment.  $\text{Ca}^{2+}$  transients in the EC microprojection during NE stimulation is almost 4 times that of the EC bulk during Ach stimulation.

The concentration of  $\text{IP}_3$  (4.4b, *blue solid line*) in the MP was slightly lesser than in the bulk (4.4b, *blue dashed line*) because of luminal stimulation of EC with Ach, but  $\text{Ca}^{2+}$  transient in MP (4.4b, *red solid line*) was  $\sim 6$  times higher than in bulk EC because of the localization of  $\text{IP}_3\text{R}$ s channels. On the other hand, during bulk SMC stimulation with NE (4.4a), the  $\text{IP}_3$  diffusing into the EC MP (4.4a, *blue solid line*) causes a high  $\text{IP}_3$  transient in the MP which does not spread into the bulk of EC (4.4a, *blue dashed line*). Like  $\text{IP}_3$ ,  $\text{Ca}^{2+}$  in the MP (4.4a, *red solid line*), does not spread much into the EC bulk (4.4a, *red dashed line*). The transient and sustained increase of  $\text{Ca}^{2+}$  in EC MP during NE stimulation is equivalent to global  $\text{Ca}^{2+}$  in bulk EC compartment during Ach stimulation

(4.4a *red solid line* and 4.4b, *red dashed lines*). The high  $\text{Ca}^{2+}$  and  $\text{IP}_3$  transients in the MP after NE stimulation of SMC can be attributed to the small volume of the MP, localization of  $\text{IP}_3\text{Rs}$  and restricted diffusion between the MP and bulk EC as other channels and pumps.

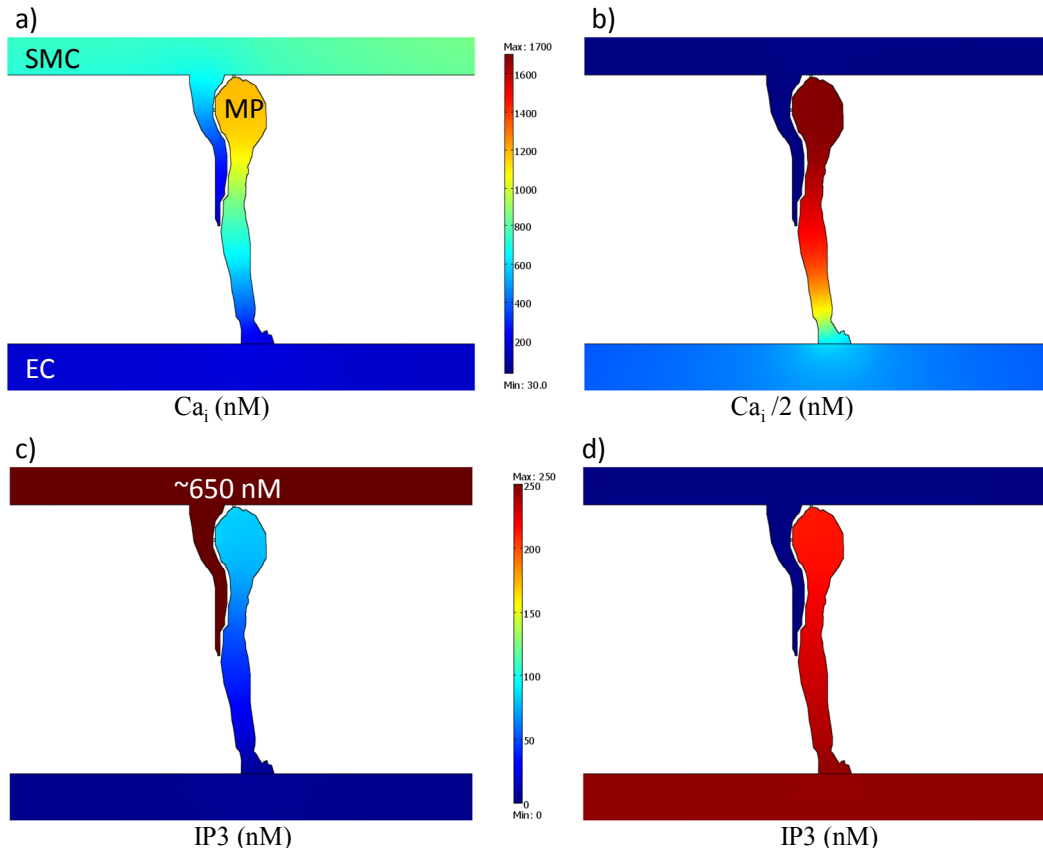
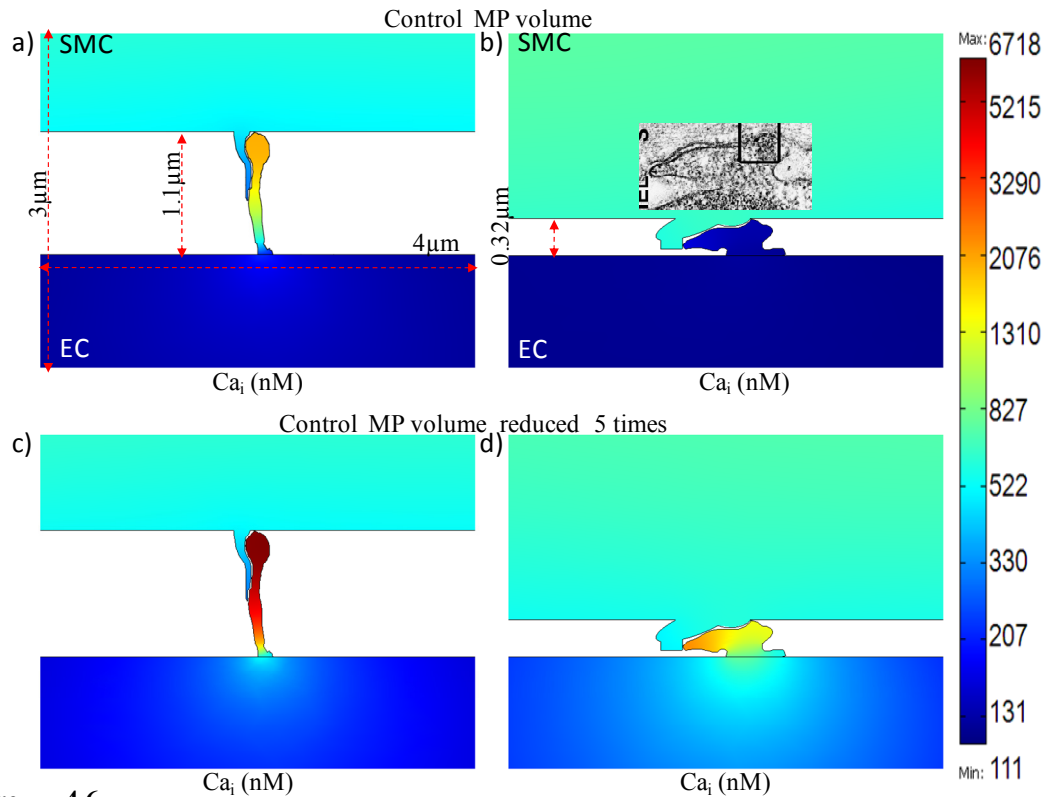


Figure 4.5 2D FEM model results for NE (a,c) and Ach stimulation(b,d) of the SMC and EC respectively. Colour bar shows the concentration of  $\text{Ca}^{2+}$  and  $\text{IP}_3$  in nM. Figure shows predicted  $\text{Ca}^{2+}$  concentration inside the MP after NE stimulation of SMC (a) bulk EC stimulation with Ach (b). c and d show the predicted  $\text{IP}_3$  transients in the MP for SMC and EC stimulation respectively.  $\text{Ca}^{2+}$  and  $\text{IP}_3$  concentration profiles are shown at time 7.5s after  $1\mu\text{M}$  NE stimulation of SMC and Ach stimulation of EC at 2s respectively.

Results are supported by the 2D FEM model which also predicted high  $\text{IP}_3$  and  $\text{Ca}^{2+}$  transients inside the MP after NE stimulation of SMC with minimal spread into the bulk EC (Figure 4.5a and 4.5c and Figure 4.7).



**Figure 4.6** Predicted  $\text{Ca}^{2+}$  concentration inside the MP after NE stimulation of SMC under control volume (a,b) and a 5 times smaller volume (c,d) for different MP shapes. Color bar shows the  $\text{Ca}^{2+}$  concentration in nM. Inset in 5b shows the experimental electron microscopy image of the projection by Herberlin et al. [114].

We also examined if differently shaped (length and surface area) MPs had any effect on the global spread of  $\text{Ca}^{2+}$  in the bulk EC (Figure 4.6). The two shapes examined were from the electron microscopy studies of Sandow et al. [174] and [114] in rat mesenteric arteries and mouse cremaster arterioles respectively. Under control MP volume, the long MP with comparatively smaller area in the Sandow et al. study had significantly higher  $\text{Ca}^{2+}$  transient which did not spread much into the bulk of EC (Figure 4.6a) while the smaller height MP with larger surface area did not have a significant  $\text{Ca}^{2+}$  transient even in the MP (Figure 4.6b). If the volume of both MPs was reduced 5 times, effectively making them flatter, the predicted  $\text{Ca}^{2+}$  transients in the MPs increased significantly in

both cases (Figure 4.6c&d), but the MP with small length and higher surface area (Figure 4.6d) allowed for a bigger spread of  $\text{Ca}^{2+}$  into the bulk of EC.

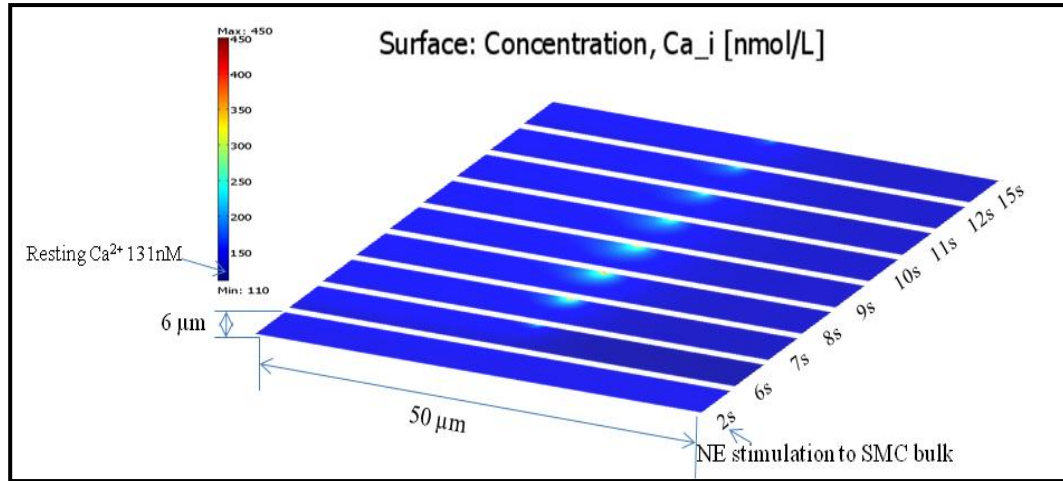


**Figure 4.7** Predicted global spread of the  $\text{Ca}^{2+}$  gradients in the EC bulk after NE stimulation of SMC

#### 4.3.2 Effect of microprojections

We examined the effect of MPs on  $\text{Ca}^{2+}$  in the EC (Figure 4.8b) and corresponding feedback in terms of SMC  $V_m$  (Figure 4.8a). The presence of MP could generate a feedback of  $\sim 3$  mV in terms of SMC  $V_m$  as compared to model with no MPs. which is apparent by the low  $\text{Ca}^{2+}$  transient in the single EC compartment model (Figure 4.8b, *dashed vs. solid lines*) as well as SMC  $V_m$  (Figure 4.8a, *dashed vs. solid*). We also examined if increasing the gap junction permeability ( $\sim 10^2$  fold  $R_{gj} = 9 \text{ M}\Omega$ ), and  $\text{IP}_3\text{R}$  current ( $\sim 10^3$  fold) in the single EC compartment model could compensate for the absence of MPs (Figure 4.8a & 4.8b, *dotted line*). Without MPs, the global EC  $\text{Ca}^{2+}$  decreased and caused EC depolarization. The compensatory measures for the absence of projection have not been reported in literature and most surprisingly are not sufficient to generate as much feedback as MPs with restricted diffusion. From the simulations, it was evident that presence of MPs facilitates the production of feedback.



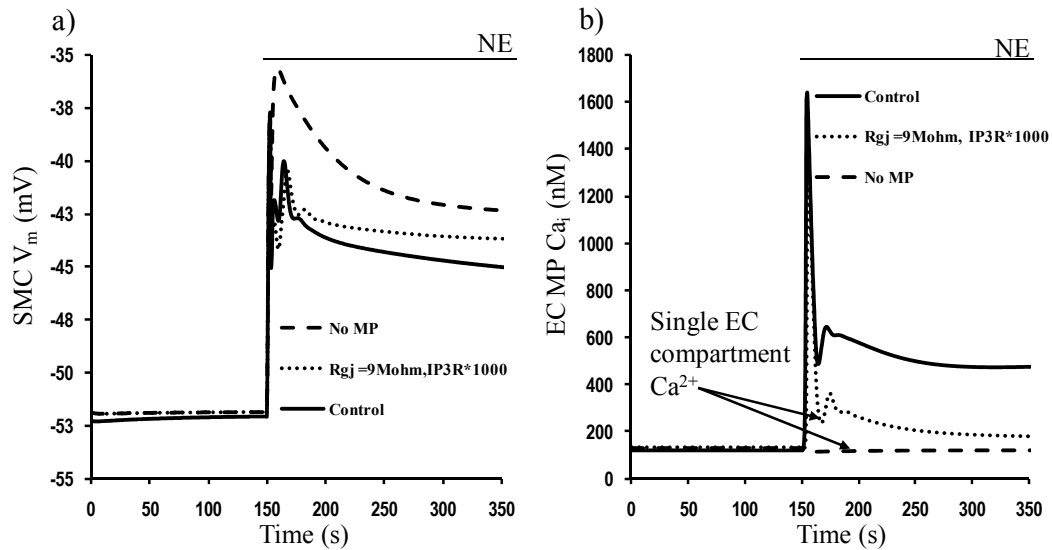


**Figure 4.8** SMC  $V_m$  (a) and EC microprojection  $Ca^{2+}$  (b) under three scenarios: No MP (dashed lines), control (solid line) and No MP with MEGJ resistance = 9 MΩ and IP<sub>3</sub>R increased 10<sup>3</sup> fold (dotted lines)

#### 4.3.3 IP<sub>3</sub> vs. Ca<sup>2+</sup> signaling

To examine the relative contributions of IP<sub>3</sub> and Ca<sup>2+</sup> diffusion to the MP Ca<sup>2+</sup>, we tested the 2D FEM model under control (Figure 4.9a) and IP<sub>3</sub> blocked (Figure 4.9b) scenarios. Figure 4.9 shows the average Ca<sup>2+</sup> transient in the MP. Under control R<sub>gj</sub> (900MΩ), IP<sub>3</sub> diffusion appears to be the major signaling molecule (Figure 4.9a, *solid line*) as Ca<sup>2+</sup> transient during IP<sub>3</sub> blockade (Figure 4.9b, *solid line*) was not significant enough to cause a feedback response. For low R<sub>gj</sub> (< 250 MΩ), Ca<sup>2+</sup> transients predicted by the control model cause very high Ca<sup>2+</sup> in MP (~ few μM) and supraphysiological SMC hyperpolarization (Figure 4.9a), however, Ca<sup>2+</sup> transient arising purely from diffusion of Ca<sup>2+</sup> (Figure 4.9b, *dashed lines*) might cause a minor feedback. The size of the predicted Ca<sup>2+</sup> transient in MP increases with decrease in R<sub>gj</sub>.

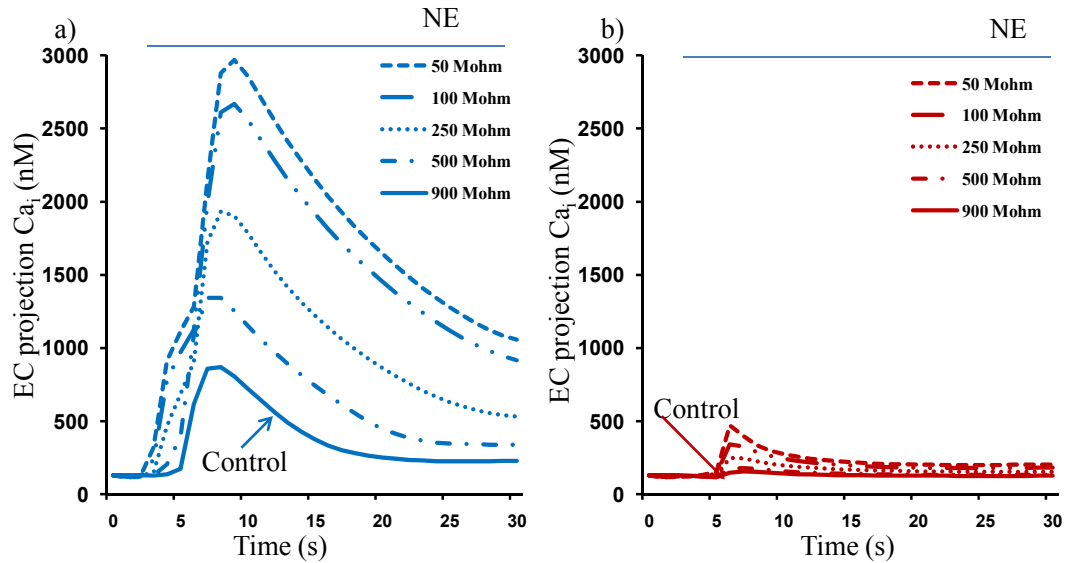


Figure 4.9 2D FEM results shows  $Ca^{2+}$  transients in the MP under control conditions (a) and with  $IP_3$  diffusion across GJ blocked (b) for different MEGJ resistances after NE stimulation of SMC at 2s. Control MEGJ resistance is 900  $M\Omega$ .

#### 4.3.4 Parametric studies

We performed parametric studies on three factors on which might determine the degree of feedback:

##### a) $IK_{Ca}$ distribution

The ability of MPs to generate feedback may depend on the degree of localization of  $IK_{Ca}$  channels on the MP. To test this we examined the compartmental model with different distribution of  $IK_{Ca}$  channels between MP and bulk EC. The amount of  $IK_{Ca}$  channels in the MP does not affect the  $Ca^{2+}$  transient in the MP (Figure 4.10b) but increases feedback with increased localization in MP (2 – 3 mV) (Figure 4.10a). The maximum feedback was achieved under control conditions with 100%  $IK_{Ca}$  channels present in the MP (Figure 4.10a, *solid line*). With uniform distribution of  $IK_{Ca}$  channels (Figure 4.10a, *dashed line*), the model loses its ability to generate feedback and resembles the output of the model with no MP (Figure 4.8a, *dashed line*).

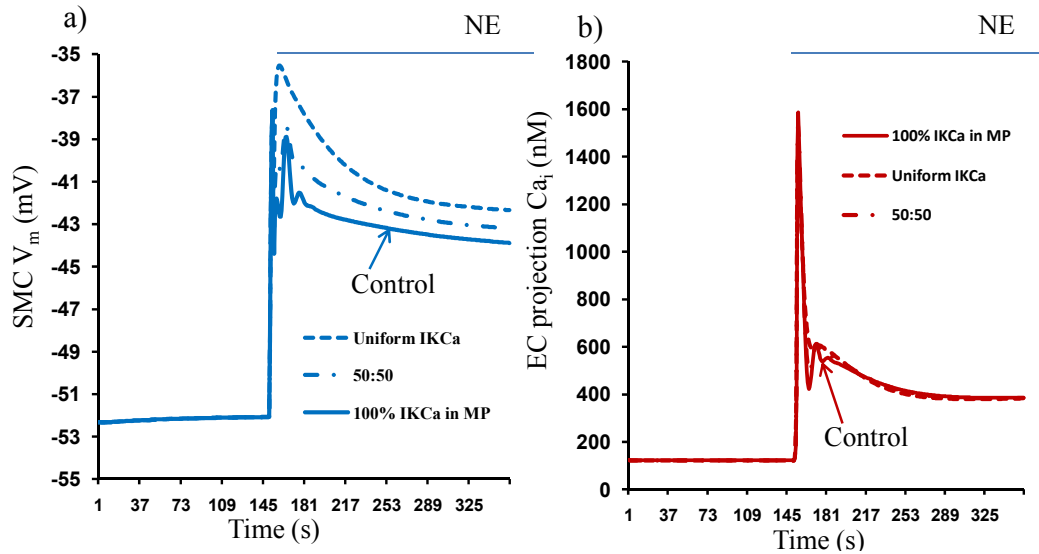


**Figure 4.10** Compartmental model results showing a) SMC  $V_m$  and b)  $Ca^{2+}$  concentration in the EC microprojection after stimulation with  $1\mu M$  NE at 150 s under different  $IK_{Ca}$  distribution in EC.

#### b) $R_{gj}$ resistance

The compartmental model predicted the effect of different  $R_{gj}$  on feedback. As the  $R_{gj}$  was reduced, the feedback in terms of SMC  $V_m$  (Figure 4.11a) and SMC  $Ca^{2+}$  (Figure 4.11b) increased. For certain values of MEGJ resistances (below  $500M\Omega$ ), with control  $IK_{Ca}$  and  $IP_3R$  localization, MP  $Ca^{2+}$  increased in concentrations high enough (Figure 4.9a) to overcome SMC depolarization and induce a hyperpolarizing response to SMC stimulation. Sustained MP  $Ca^{2+}$  levels were close  $Ca^{2+}$  transients in MP during Ach stimulation (Figure 3b, *solid line*). Feedback in terms of SMC  $V_m$  and SMC  $Ca^{2+}$  vs.  $R_{gj}$  is shown in Figure 4.11c and 4.11d respectively. Feedback was calculated as the difference in  $V_m$  between the current model and the model with no MP.

#### c) $IP_3R$ localization

As no quantitative information regarding  $IP_3R$  localization is available in the literature, the model examined feedback in terms of SMC  $V_m$  (Figure 4.12a) and SMC  $Ca^{2+}$  (Figure 4.12b) for a range of  $IP_3R$  localization in the MP. As expected, greater

feedback was achieved with higher IP<sub>3</sub>R density in the MP. Around 6 mV of hyperpolarizing feedback can be achieved with 30% IP<sub>3</sub>R localization in MP (Figure 4.12c, *long dashed line*). Under control conditions (10% IP<sub>3</sub>Rs in MP), the maximum feedback achieved was around 3 mV (Figure 4.12a, *solid vs. dashed line*). The feedback is calculated as the difference in  $V_m$  of the current model with the model with no MPs. The  $R_{gj}$  for these simulations was 900 M $\Omega$  with restricted diffusion between the projection and bulk EC.

#### 4.4 Discussion

The primary aim of this study was to understand the role of MPs in myoendothelial signaling. With the proposed models we examined the effect of MPs on intracellular Ca<sup>2+</sup> in EC and SMC and the resulting NO-independent feedback response from EC to SMC. For this purpose, the NO signaling pathway has been blocked in all simulations. We also tested parameters ( $R_{gj}$ , IP<sub>3</sub>R density and IK<sub>Ca</sub> distribution) that might affect the functionality of MPs.

Endothelial control of vascular tone is attributed to an increase in EC Ca<sup>2+</sup> followed by activation of vasodilatory pathways like EDRF, prostacyclin (PGI<sub>2</sub>) and EDHF [80, 99, 100]. Consistent with experimental findings, both the compartmental and 2D FEM control models show global IP<sub>3</sub> and Ca<sup>2+</sup> increase in EC when stimulated by saturating concentrations of Ach (Figure 4.4a and 4.4b) leading to EC and subsequently SMC hyperpolarization [80, 121, 122, 182]. After SMC stimulation, however, there was a high Ca<sup>2+</sup> transient of local nature present in and around the MP as compared to the bulk EC (~ 5 times). In contrast to some experiments [80, 121], in both the models, the IP<sub>3</sub> and Ca<sup>2+</sup> increase in EC after SMC stimulation was confined to the MPs and its global

spread was rather limited (Figure 4.5a and Figure 4.7). IP<sub>3</sub> mediated spontaneous as well as initiated local Ca<sup>2+</sup> events have been observed in MPs and SMC stimulation has been shown to affect the frequency of these events in rat mesenteric arteries [117, 119].

#### 4.4.2 Feedback

The local Ca<sup>2+</sup> transients present in the EC MP after SMC stimulation generated a hyperpolarizing feedback in SMC of around 3mV (Figure 4.8a, *solid line*) under control conditions of equal gap junction permeability ( $R_{gj} = 900 \text{ M}\Omega$ ) to Ca<sup>2+</sup> and IP<sub>3</sub> and localization of IP<sub>3</sub>Rs and IK<sub>Ca</sub> in EC MP. In fact, when there is no restricted diffusion between the MPs and bulk EC (effectively implementing EC as a single compartment), the IP<sub>3</sub> and Ca<sup>2+</sup> entering the MPs from the stimulated SMC rapidly diffuse into the entire cell and fail to produce a local or global Ca<sup>2+</sup> increase (Figure 4.8b, *dashed line*) in spite of localized IP<sub>3</sub>R still present near the MEGJs. This is not surprising as the movement of both IP<sub>3</sub> and Ca<sup>2+</sup> in the cytoplasm is limited. Ca<sup>2+</sup> is rapidly sequestered by intracellular buffering proteins (Forward rate constant for Ca<sup>2+</sup> binding to cytosolic proteins: 100.0 mM<sup>-1</sup>·ms<sup>-1</sup>) and IP<sub>3</sub> degraded by 1-5 phosphatases present in the cytosol (IP<sub>3</sub> degradation rate: 2×10<sup>3</sup> ms<sup>-1</sup>) [129]. Along with the Ca<sup>2+</sup> transient, the feedback generated in the presence of MPs (~3 mV) is also lost (Figure 4.8a, *dashed line*) in the well mixed model in spite of the IK<sub>Ca</sub> localization still present near the MEGJs. Even an increase in gap junction IP<sub>3</sub> permeability (10<sup>2</sup> times) and IP<sub>3</sub>R current (10<sup>3</sup> times) in the effectively single EC compartment failed to evoke a global Ca<sup>2+</sup> increase and feedback similar to the control model with MPs (Figure 4.8a and b, *dotted line*). Thus, it appears that in conjunction with the localization of IK<sub>Ca</sub> and IP<sub>3</sub>Rs, the presence of MP with restricted diffusion to bulk of EC was essential for facilitation of EC feedback following SMC

stimulation. The presence of a regenerative mechanism in the EC might allow for passive spread of MP  $\text{Ca}^{2+}$  into the bulk EC as simple diffusion of  $\text{IP}_3$  or  $\text{Ca}^{2+}$  did not appear to account for experimentally observed global  $\text{Ca}^{2+}$  events. It is important to note here that the differences in  $\text{Ca}^{2+}$  and  $\text{IP}_3$  concentration between the MPs and bulk EC as well as the spread of MP  $\text{Ca}^{2+}$  into the bulk EC were dependent on the relative size, shape and volume of the MP with respect to the bulk of EC (Figure 4.5 and 4.6). Despite differences in the feedback capacities of differently shaped MPs, their presence seem to be imperative for experimentally observed feedback.

#### **4.4.3 Parametric studies**

$\text{Ca}^{2+}$  elevation in EC (local or global) is the key determinant of endothelial feedback. Our results predicted high local  $\text{Ca}^{2+}$  transient in the MPs was responsible for generating a hyperpolarizing feedback of  $\sim 3\text{mV}$  in the SMCs. We also examined factors which control the amount of  $\text{Ca}^{2+}$  transient in the MP. MEGJ are the primary  $\text{NO}^-$  independent pathway used to describe transfer of agonist induced EC hyperpolarization to SMC [90, 117, 183]. Gap junctions are believed to be nonselective in nature with similar permeability for all ions and  $\text{IP}_3$  [82, 95]. Literature values of  $R_{\text{gj}}$  are spread over a large range of 70 – 900  $\text{M}\Omega$  depending on the particular tissue and experimental conditions [96-98]. The value of  $R_{\text{gj}}$  will affect the permeability to different ions and  $\text{IP}_3$  and in turn affect the amount  $\text{Ca}^{2+}$  in MPs.  $\text{Ca}^{2+}$  in the EC MP (Figure 4.11b) increased as the  $R_{\text{gj}}$  was decreased. This in turn leads to higher feedback in terms of SMC  $\text{Ca}^{2+}$  and SMC  $V_m$  (Figure 4.11c & d). Resistances below 500  $\text{M}\Omega$  caused supraphysiological SMC hyperpolarization of  $\sim 10\text{-}15\text{ mV}$  (Figure 4.11d) to NE stimulation of SMC under control model conditions. This hyperpolarizing feedback would differ for different localization of  $\text{IP}_3\text{Rs}$  and  $\text{IK}_{\text{Ca}}$  but

showed the potential of local  $\text{Ca}^{2+}$  transients to generate feedback as large as agonist induced hyperpolarization of the EC.

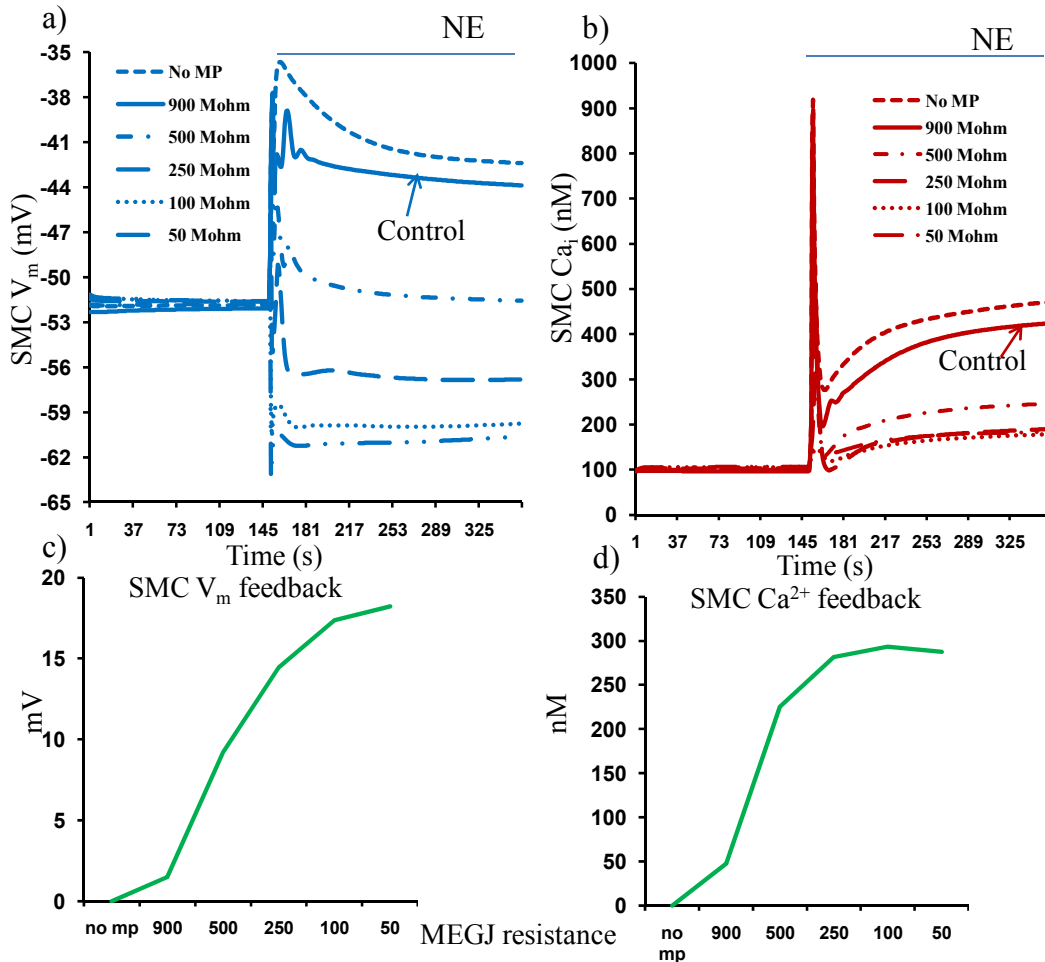


**Figure 4.11**  $\text{Ca}^{2+}$  transients in the SMC (b) and the corresponding changes in SMC  $V_m$  (a) after SMC stimulation with  $1\mu\text{M}$  NE at 150s for different myoendothelial gap junction resistances. (c) and (d) show the cumulative feedback with respect to SMC  $V_m$  and SMC  $\text{Ca}^{2+}$ .

The co-localization of  $\text{IP}_3\text{Rs}$  and  $\text{IK}_{\text{Ca}}$  is crucial for MP generated feedback mechanism [122, 174, 177, 178]. While most of  $\text{IP}_3\text{R}$  clusters seem to be present along the projections [119], their presence in the rest of the EC cannot be neglected as they are responsible for experimentally observed  $\text{Ca}^{2+}$  increase in EC after Ach stimulation which is most likely initiated from the luminal side of the EC opposite to the location of MPs. We tested a range of  $\text{IP}_3\text{R}$  receptor densities (uniform-30%) inside the MP (Figure 4.12)

for the same  $R_{gj}$  ( $900M\Omega$ ) and  $IK_{Ca}$  distribution. A hyperpolarizing feedback of  $\sim 6mV$  could be achieved with 30%  $IP_3R$  localization (Figure 4.12c). ER is a dynamic and flexible structure spread throughout the EC undergoing constant change. ER provides a single continuous space for the movement of  $Ca^{2+}$  ions and can direct  $Ca^{2+}$  movement in the cell by concentrating  $IP_3Rs$  in a particular cellular region[184, 185]. Perhaps, for this reason, ER localizes at the base and inside of some projections so as to increase the density of  $IP_3R$  in the projection to form a local regulating module to enhance the feedback of EC to SMC.

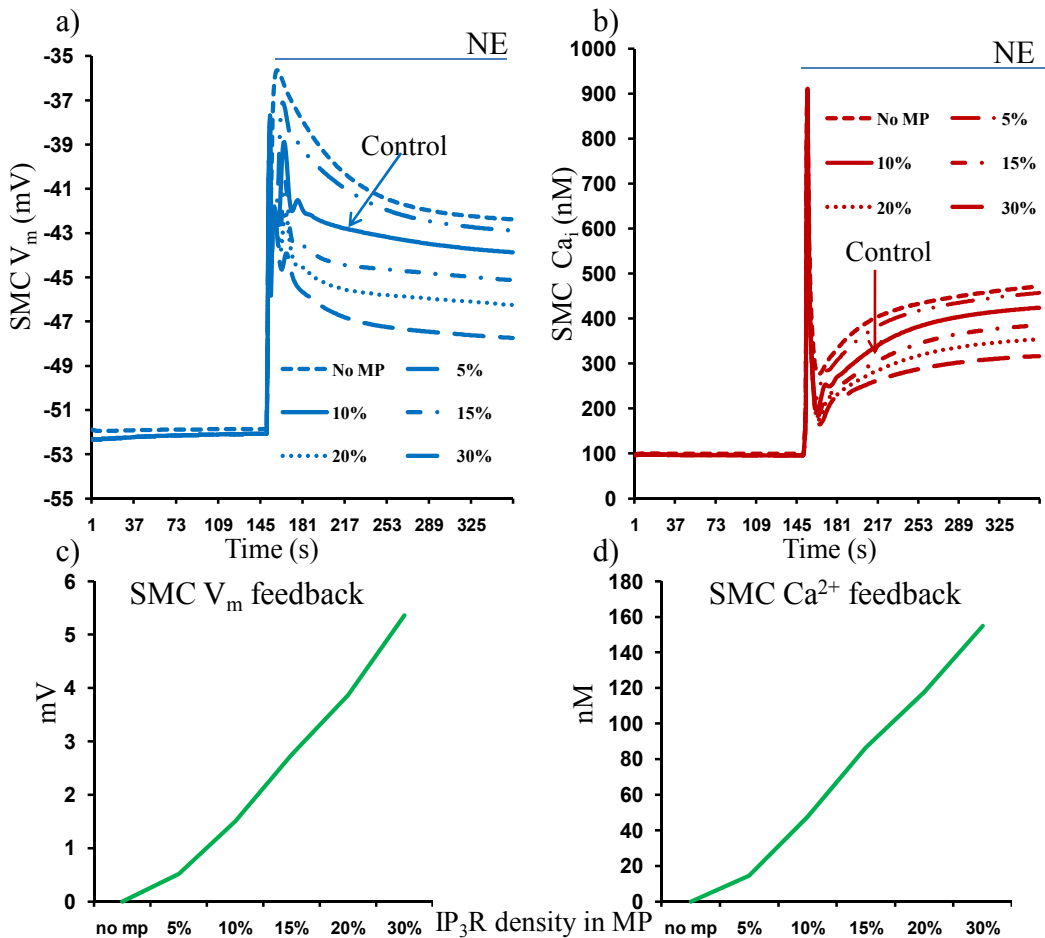


Figure 4.12 SMC  $V_m$  (a) and SMC  $Ca^{2+}$  transients (b) for different  $IP_3R$  density inside the projection. Cumulative feedback in the form of SMC  $V_m$  (c) and SMC  $Ca^{2+}$  (d) is as shown.



Experimental studies have shown a spatial separation of  $IK_{Ca}$  channels in and around the projections while  $SK_{Ca}$  channels are mostly confined to the bulk of EC near EC-EC tight junctions [177, 179]. This is important as MPs contain most of the  $IK_{Ca}$  channels which along with  $SK_{Ca}$  channels are responsible for EC hyperpolarization during EC stimulation [179, 186]. Segregation of  $IK_{Ca}$  and  $SK_{Ca}$  channels might be a way to engage the  $IK_{Ca}$  channels in local feedback through MP  $Ca^{2+}$ . In the model predictions, during SMC stimulation, the concentration of  $Ca^{2+}$  in the MPs was similar to global  $Ca^{2+}$  concentration in EC during Ach (a potent vasodilator) stimulation of EC (Figure 4.4a *red solid line* vs. Figure 4.4b, *red dashed line*). Therefore, the unique orientation of  $IK_{Ca}$  channels might dismiss the need of a global response for feedback as now, most of the  $IK_{Ca}$  channels can be activated by a local  $Ca^{2+}$  increase in MP. This was also reflected in the fact that for the same  $Ca^{2+}$  transient in the MP (Figure 4.10b), the feedback generated in terms of SMC  $V_m$  with the control model (100%  $IK_{Ca}$  localized to MP) was lost with uniform distribution of these channels (Figure 4.10a, *dashed line*). The feedback progressively decreased with decrease in the amount of  $IK_{Ca}$  channels localized in the MP.  $R_{gj}$  and  $IP_3R$  concentration are maintained at their respective control values. Therefore, it is important to find a way to quantify the amount of  $IP_3Rs$  and  $IK_{Ca}$  channels in the MP to accurately describe its role in endothelial feedback to SMC stimulation.

#### 4.4.4 $IP_3$ vs. $Ca^{2+}$ diffusion

The importance of EC MP  $Ca^{2+}$  transient has been emphasized by previous results; however, the source of this transient has not been discussed.  $Ca^{2+}$  mobilization in EC after SMC stimulation has been attributed to the diffusion  $Ca^{2+}$  ions [80, 121] and/or  $IP_3$  [122, 183] down their concentration gradient as electrical coupling of SMC to EC

alone would cause EC depolarization and EC  $\text{Ca}^{2+}$  reduction. The buffering of  $\text{Ca}^{2+}$  by cytosolic proteins and metabolization of  $\text{IP}_3$  by 1-5 phosphatases in the cytosol are both unfavourable to their respective movement inside the cell [181, 183]. Theoretically, both,  $\text{Ca}^{2+}$  and  $\text{IP}_3$  can diffuse down their concentration gradient into the EC MP during SMC stimulation with equal permeability and activate the  $\text{IP}_3\text{R}$  which is known to exhibit  $\text{IP}_3$  and  $\text{Ca}^{2+}$  dependent activation as well as  $\text{Ca}^{2+}$  dependent inhibition for higher range of  $\text{Ca}^{2+}$  concentration. However,  $\text{Ca}^{2+}$  diffusion alone cannot activate  $\text{IP}_3\text{R}$  unless some basal quantities of  $\text{IP}_3$  are present in the EC. Vascular cell co culture studies by Isakson et al. [178, 183] suggest that  $\text{Ca}^{2+}$  diffusion might contribute to the initial rise in the EC  $\text{Ca}^{2+}$  and movement of  $\text{IP}_3$  into the cell leads to the sustained rise in the cell as the blockade of  $\text{Ca}^{2+}$  across MEGJ causes a delayed rise in EC  $\text{Ca}^{2+}$ . Also, the diffusing  $\text{IP}_3$  can rapidly activate the localized  $\text{IP}_3\text{Rs}$  and the  $\text{Ca}^{2+}$  released from the store might be sufficient to cause calcium induced calcium release in the receptor without the need of additional  $\text{Ca}^{2+}$  diffusion from the SMC. No such favorable localization of  $\text{RyR}$  has been reported for  $\text{Ca}^{2+}$  to have a direct role in inducing  $\text{Ca}^{2+}$  transients present in the EC MP. Blocking any component of the  $\text{IP}_3$  signaling pathway (PLC inhibition in SMC,  $\text{IP}_3\text{R}$  blocking in EC) leads to reduction in  $\text{Ca}^{2+}$  transients in the EC. Recent experimental data in hamster skeletal muscle arterioles provides evidence for  $\text{IP}_3$  mediated feedback and corroborate the theoretical predictions. When the SMC was stimulated with an  $\text{IP}_3$  releasing vasoconstrictor (PE) a feedback response could be inhibited by blocking of EC  $\text{IP}_3\text{Rs}$  (Xestospongine C). In contrast, depolarization and vasoconstriction with a voltage dependent potassium channels ( $\text{K}_v$ ) blocker, 4-aminopyridine (4-AP) remain unchanged after similar blockade of  $\text{IP}_3\text{Rs}$  in the endothelium[120]. 2D FEM model results under

control (Figure 4.9a) and blocked IP<sub>3</sub> diffusion (Figure 4.9b) condition for different R<sub>gj</sub>s predict significant reduction in Ca<sup>2+</sup> transients during IP<sub>3</sub> blockade (~4 times) which suggests that the majority of Ca<sup>2+</sup> transient can be attributed to the diffusion of IP<sub>3</sub> and not Ca<sup>2+</sup>. Results are in agreement with our previous EC- SMC model where IP<sub>3</sub> contribution to EC feedback was more significant than Ca<sup>2+</sup> [129]. In the previous model, the lack of MPs was compensated by higher IP<sub>3</sub>R density in EC and higher IP<sub>3</sub> GJ permeability. Ca<sup>2+</sup> diffusion independent of IP<sub>3</sub> appeared to be significant only at very low values of R<sub>gj</sub> (< 250 MΩ) (Figure 4.11b). Thus, despite the small volume of MP and restricted diffusion between MP and bulk EC and due to the lack of favorable localization of RyRs and/or a regenerative mechanism, Ca<sup>2+</sup> diffusion alone did not contribute significantly towards Ca<sup>2+</sup> transients in the EC MP. In contrast, the localization of IP<sub>3</sub>R receptors in the EC MP allowed even a small IP<sub>3</sub> diffusion to amplify the Ca<sup>2+</sup> transient in the MP. It should be noted, however, that the relative contribution of Ca<sup>2+</sup> and IP<sub>3</sub> depends also, on their rate of buffering and metabolization respectively. A range of time constants for IP<sub>3</sub> degradation has been used across literature depending on the type of cells modeled, and the choice of this parameter might affect the local and global Ca<sup>2+</sup> responses. Considering all the above factors, it appears that contribution of Ca<sup>2+</sup> diffusion to feedback is unlikely but cannot be neglected altogether.

#### **4.5 Limitations**

Consistency was maintained with the previous two cell model with respect to parameter values and whole cell currents. Wherever available, we have used values from rat mesenteric artery data. The model's behavior could change qualitatively and quantitatively with better tissues-specific parameter values, such as plasma membrane

channel conductance, myoendothelial IP<sub>3</sub> permeability, dimension and number of MPs. Localization of IP<sub>3</sub>Rs, IK<sub>Ca</sub> and MEGJs inside the MPs has been shown in the literature. However, because of the lack of quantitative measurements, we have assumed reasonable values for these variables or tested for a range of parameters defining these quantities. The compartmental models do not incorporate this level of detail but approximate well the electrical properties of the nearly iso-potential endothelial and smooth muscle cells. The 2D model captures well the behavior of Ca<sup>2+</sup> inside the MP and can account for spatial localization of channels or receptors. The present model does not generate global EC Ca<sup>2+</sup> responses during feedback. A regenerative mechanism of IP<sub>3</sub> generation by Ca<sup>2+</sup> in ECs might be able to produce global Ca<sup>2+</sup> increase which is absent in the current models but can be tested in future models. The biological variability of the vessels and different experimental conditions may contribute to the discrepancies and are difficult to take into account in a theoretical model.

#### **4.6 Conclusion**

The models developed in this study were a first attempt to capture the role of MPs in small arteries. Both models showed high Ca<sup>2+</sup> transients in the MP which do not spread into the bulk of the ECs. Under control R<sub>gj</sub> and IP<sub>3</sub>R localization, IP<sub>3</sub> rather than Ca<sup>2+</sup> appears to be the SMC initiated signal mainly responsible for the Ca<sup>2+</sup> transients in the EC MPs after SMC stimulation. The models predicted that even in the absence of NO signaling pathway, the high Ca<sup>2+</sup> in the EC MP was able to hyperpolarize the SMC (~2-3mV) by a local feedback mechanism which was lost in the absence of MPs under experimentally suggested R<sub>gj</sub> values. Along with R<sub>gj</sub>, the amount of Ca<sup>2+</sup> transient in the MP as and the subsequent feedback depended on the degree of IP<sub>3</sub>R and IK<sub>Ca</sub> localization

in the MPs respectively as well as the volume of the MP and restricted diffusion of ions and IP<sub>3</sub> between the two compartments. Based on this study, it is evident that MPs are important for amplification of SMC initiated signals and cause an IP<sub>3</sub> mediated feedback during SMC stimulation.

**Acknowledgments:** This author is supported by the dissertation year fellowship from the University Graduate School, Florida International University

## Chapter 5: Endothelium derived hyperpolarizing factor

This chapter is to be submitted (with slight modifications) as

Nagaraja,S., A.Kapela and N.Tsoukias, 2011, "EDHF pathways in the microcirculation: a theoretical analyses."

Abstract:

This study investigates the role of  $K^+$  accumulation and MEGJ coupling in EDHF mediated SMC hyperpolarization. A previously developed compartmental EC-SMC model with MPs is modified to include a subcompartment in the SMC to represent a microdomain with localized  $NaK_{\alpha 2}$ . The extracellular space is also divided into two compartments to represent a cleft and bulk to account for accumulation of  $K^+$  in the extracellular space. A 2D continuum model is developed to account for MP geometry and spatial heterogeneity of channels and receptors in the endothelium and is extended to include the spatial heterogeneity in  $NaK$  pumps on SMC. Simulations predict accumulation of  $K^+$  in the extracellular space between the EC and SMC following both Ach and NE stimulation. However, accumulation of  $K^+$  significantly alters the Nernst potential of  $K^+$  and affects EC hyperpolarization and future release of  $K^+$  via  $IK_{Ca}$ . Blockade of MEGJ coupling severely inhibits EDHF action and cannot be restored by increasing the contribution of  $NaK_{\alpha 2}$ . Thus, under most scenarios, purely  $K^+$  mediated EDHF was small and transient in nature.

Keywords: myoendothelial signaling, sodium –potassium pump,  $K^+$  accumulation, EDHF feedback, MEGJ coupling.

## 5.1 Introduction

Since its discovery, EDHF signaling has been extensively experimented and reviewed and many factors have been considered for the role of EDHF such as  $K^+$  ions, hydrogen peroxide ( $H_2O_2$ ), carbon monoxide (CO), C-type natriuretic peptide (CNP), epoxyeicosatrienoic acids (EETs) and the  $V_m$  transfer via the physical coupling of EC and SMC by MEGJs but no one single universal pathway is agreed upon [99, 100, 112-114, 174, 187]. The classical action of EDHF necessitates an increase in the EC  $Ca^{2+}$  concentration followed by the opening of endothelial  $SK_{Ca}$  and  $IK_{Ca}$  and subsequent EC hyperpolarization. The resulting SMC hyperpolarization can be blocked by a combination of apamin and TRAM but not by apamin and iberiotoxin which blocks  $BK_{Ca}$  [93, 179, 186, 188-192]. Recent evidence shows that these channels are spatially segregated in different areas of the EC and can be selectively activated by local  $Ca^{2+}$  gradients in the EC [177, 179]. After the initial mandatory action of EC hyperpolarization, the classical EDHF action can be propagated to the SMC in two ways:

### a) MEGJ

MEGJ proteins are expressed all along the vasculature [82]. Electrical change measurements and dye transfer studies have established the ability of these junctions to transfer electrical and ionic changes between the two cell types along with the transport of small second messenger molecules such as  $IP_3$  [84-86]. There is now a sizeable amount of evidence that EDHF is simply the electrotonic spread of hyperpolarization from EC to SMC via gap junctions [88-91, 116]. MEGJ expression has been shown to increase with decrease in vessel size which is coincidental with regards to EDHF action [89]. The main difficulties in confirming the role of MEGJs in EDHF are technical difficulties in

measuring EC to SMC communication in vivo [193] because of their location and the unavailability of specific blockers for myoendothelial gap junction proteins. Also, inhibition of EDHF by gap junction blocking experiments need to be treated with caution because gap junction blocking peptides do not necessarily block only MEGJs but can block the action of homocellular gap junction present between individual ECs and SMCs which might block other conductive responses in those arteries. Mather et al performed an experiment by loading connexin 40 antibodies in the ECs to study the effect of GJ in EDHF which showed that contribution of GJ signaling to EDHF depended on level of constriction of the arteries [94]. EDHF was inhibited in these arteries devoid of connexin 40 when precontracted with high PE concentrations while ineffective for low stimulatory PE concentrations. This suggests possibility for a complimentary pathways acting simultaneously or subsequently with MEGJ signaling.

#### b) $K^+$ ions

Some studies support that a diffusible factor like  $K^+$  ion could in fact be EDHF. This theory has received attention because in many arteries, an extracellular increase in  $K^+$  has shown to hyperpolarize and relax SMCs which is inhibited in presence of NaK blocking ouabain [192, 194]. Moreover, there is evidence for the presence of  $NaK_{\alpha 2}$  and  $NaK_{\alpha 3}$  isoform or ouabain independent isoform of NaK pumps on SMCs in addition to the ubiquitously expressed  $NaK_{\alpha 1}$  [34]. These additional isoforms are sensitive to an extracellular increase in  $K^+$  unlike the  $NaK_{\alpha 1}$  which is saturated at resting levels of extracellular  $K^+$ . The presence of cellular extensions from EC/SMC (microprojections) in the internal elastic lamina allow the creation of highly restricted spaces between the EC and SMC where the  $K^+$  exiting from the EC can accumulate. Emergence of these



microprojections might occur to promote accumulation of  $K^+$  ions in the restricted space (10-30 nm) [174]. However, in many preparations from different species including rat mesenteric,  $K^+$  increase does not evoke consistent relaxations and hyperpolarization in SMCs [116, 195-197] and in some like the mouse aorta, extracellular  $K^+$  increase produced depolarization in SMCs [198].

The second pathway described for EDHF also necessitates an increase in  $Ca^{2+}$  in EC but it doesn't require EC hyperpolarization and is not abolished by blockade of  $IK_{Ca}$  and  $SK_{Ca}$  channels. It depends on the production of other  $Ca^{2+}$  dependent factors like EETs, CNP,  $H_2O_2$  and CO which are known to promote SMC hyperpolarization by activating SMC  $BK_{Ca}$  and/or  $K_{ATP}$  channels [88, 99, 112, 113, 122, 199]. However, the action these factors are not strongly seen in many vessel types.

Current research is focused on establishing a standard protocol for EDHF action and resolving the role of  $K^+$  as an efficient EDHF. As the efflux of  $K^+$  from  $IK_{Ca}$  and  $SK_{Ca}$  channels is responsible for both  $K^+$  accumulation as well as EC hyperpolarization, it has been challenging to experimentally isolate the two effects. Mathematical modeling can be an effective tool in analyzing the suggested pathways for EDHF. There have been few theoretical models to describe EDHF mechanisms. Schuster et al predicted the amount of  $K^+$  that can accumulate (10-17 mM) in the myoendothelial space (1-6  $\mu$ m) based on the  $IK_{Ca}$  and  $SK_{Ca}$  currents measured in cultured ECs in response to bradykinin stimulation[77]. However, these calculations can be extended to include the effect of  $K^+$  accumulation on EC  $V_m$ ,  $IK_{Ca}$  and  $SK_{Ca}$  currents and its effect on subsequent release of  $K^+$ . The different suggested pathways can be easily tested in a model for a wide range of conditions free from the ambiguity of experimental scenarios. The current study describes

two models (compartmental and 2D FEM) based on rat mesenteric data including appropriate features needed to predict role of  $K^+$  and GJ coupling in the classical EDHF action.

## 5.2 Model development

### 5.2.1 Compartmental model

This model was based on our previously developed EC-SMC model with MPs (Figure 4.2). An sub compartment was added in the SMC to act as microdomains with dimensions described by Ledoux et al. [119] for MPs. Studies confirm the presence of  $NaK_{\alpha 2}$  isoform on SMC membrane in addition to the ubiquitous  $NaK_{\alpha 1}$  isoform [32, 34, 200, 201]. We assumed  $NaK_{\alpha 2}$  isoform to be present exclusively on the surface of the microdomains which is in contact with the extracellular cleft where  $K^+$  accumulates whereas  $NaK_{\alpha 1}$  isoform was confined to the membrane lying above the bulk SMC. This was done in the model by altering the maximum current through the pump and the half activation parameters of  $K^+$  and  $Na^+$ . We used values reported by Blanco et al. [32] for these parameters as listed in Table 5.1. The total NaK current was maintained the same as in previous models and was divided between the two compartments.

| <i>Parameter</i> | <i>Value</i>          | <i>Description</i>                                    |
|------------------|-----------------------|---|
| $K_{mK}$         | SMC bulk: 1.6[mM]     | Half saturation $K^+$ constant for $NaK_{\alpha 1}$   |
|                  | SMC MD: 4.8[mM] [34]  | Half saturation $K^+$ constant for $NaK_{\alpha 2}$   |
| $K_{mNa}$        | Bulk SMC: 22[mM]      | Half saturation $Na^+$ constant for $NaK_{\alpha 2}$  |
|                  | MD: 8.8[mM]           | Half saturation $Na^+$ constant for $NaK_{\alpha 2}$  |
| $NaK2\_1$        | 0.1-0.9 (depending on | Ratio of $NaK_{\alpha 2}$ current to $NaK_{\alpha 1}$ |

|                    | simulation)            |   |
|--------------------|------------------------|---|
| $A_{\text{cleft}}$ | $0.0352 \mu\text{m}^2$ | Area of extracellular cleft between EC MP and SMC MD ( $2\pi rh$ ) (radius of MP and height of projection from table 4.1) |
| $L_{\text{cleft}}$ | $1\mu\text{m}$         | Length of diffusion from cleft to bulk  |
| $N_{\text{md}}$    | 2.7 [93]               | Number of MEGJ/ EC  |

**Table 5.1: List of parameters changed from the EC-SMC model**

**a) Cleft and bulk**

The extracellular space in the internal elastic lamina (IEL) was divided into two compartments the cleft and bulk. The cleft was the volume of the IEL between the EC microprojection and SMC microdomain while bulk was the extracellular space surrounding the rest of the cell. The height of the cleft was assumed to be 10nm as suggested by Sandow et al. [174]. Electrodiffusive flux equations account for the flow of ions from cleft to bulk. Suffixes ‘cleft’ and ‘bulk’ represent the respective concentrations in the cleft and bulk compartments of the IEL as shown in Eq. 5.1

$$I_{\text{cleft}_S} = \frac{z_S F D_S A_{\text{cleft}} ([S]_{\text{cleft}} - [S]_{\text{bulk}})}{L_{\text{cleft}}} \quad (5.1)$$

where ‘S’ is the concentration of  $\text{Na}^+$   $\text{K}^+$   $\text{Ca}^{2+}$  and  $\text{Cl}^-$  and values of the remaining parameters and their description are listed in Table 5.1

**5.2.2 2D finite element model**

We have previously developed 2D finite element model for studying the role of MPs in myoendothelial feedback. The model was modified to include  $\text{NaK}_{\alpha 2}$  pumps on the boundary of SMC facing the microprojections where they can be exposed to any

concentration increase in  $K^+$  (Figure 5.1). This was done by modifying the equation of NaK current along the boundaries facing the myoendothelial space. As in the compartmental model, the total NaK current was maintained the same and was divided between the two sets of boundaries containing either NaK isoform.

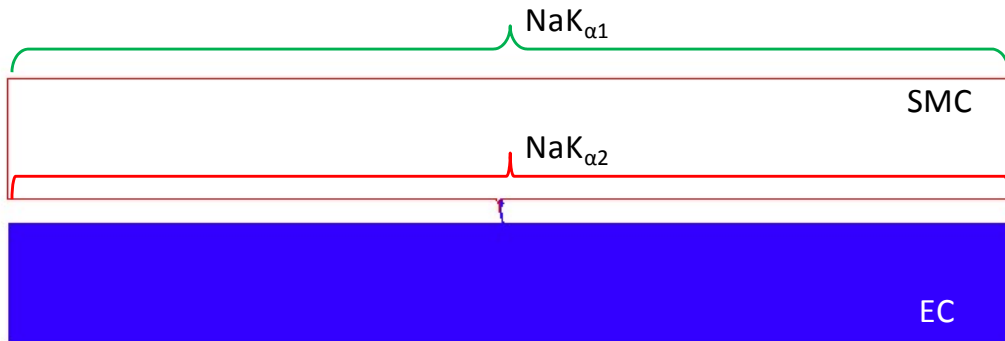


**Figure 5.1**  $NaK_{\alpha 2}$  is defined over the lower boundaries of SMC facing the extracellular space where  $K^+$  can accumulate

## 5.3 Results

### 5.3.1 Potassium accumulation with leaky extracellular space

Figure 5.2 shows the increase in  $K^+$  in the small extracellular regions between the EC MPs and SMCs during both (a) EC and (b) SMC stimulation in the 2D FEM. The concentration of  $K^+$  was higher during NE stimulation because of the higher gradient for  $K^+$  leakage as well as contribution from  $BK_{Ca}$  channels in SMCs.

### 5.3.2 Potassium accumulation with no leak into extracellular space

Accumulation of  $K^+$  after Ach stimulation also depends upon the leakiness of the extracellular space. If  $K^+$  was not allowed to leak outside the area between the EC and SMC, the accumulation of  $K^+$  with localized  $IK_{Ca}$  on MPs was almost double (Figure 5.3a) than when leak was allowed (Figure 5.2a). Even a uniform  $IK_{Ca}$  channel distribution can generate an increase in extracellular  $K^+$  (Figure 5.3b) in the 2D FEM model with no extracellular  $K^+$  leak.

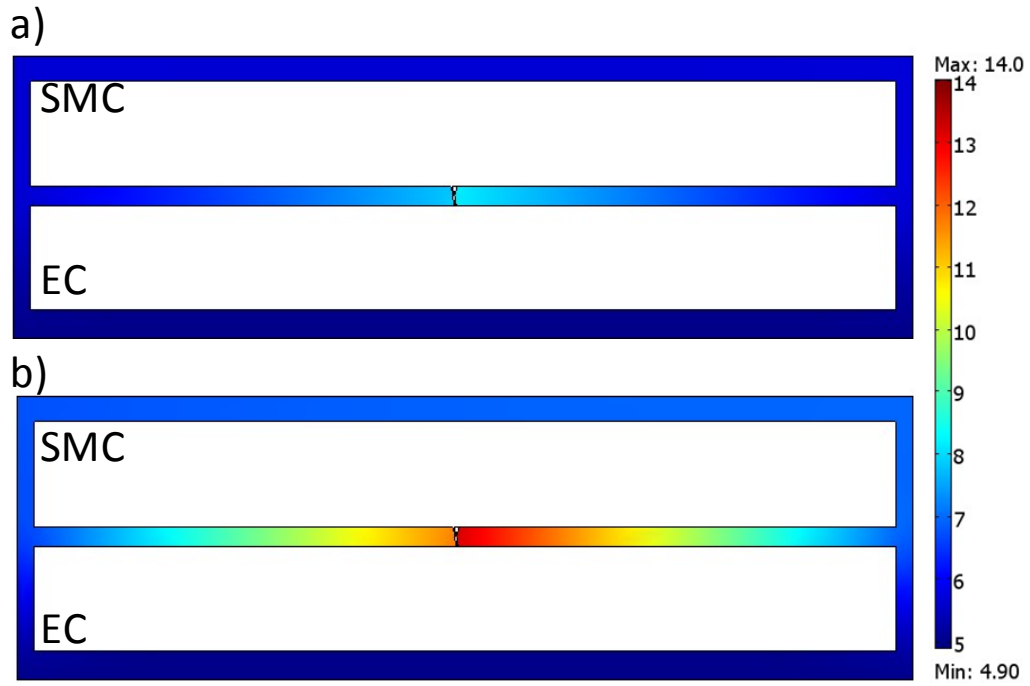


Figure 5.2 Extracellular  $K^+$  (mM) accumulation during a) Ach stimulation of EC and b) NE stimulation of the SMC.



Figure 5.3  $K^+$  accumulation (mM)(color bar) in the extracellular spaces during Ach stimulation with no leak into space beyond the EC and SMC area with a) localized  $IK_{Ca}$  channels on the MP and b) uniform  $IK_{Ca}$  channels distribution across whole EC.

### 5.3.3 Effect of potassium accumulation during Ach stimulation

To examine the effect of extracellular on  $K^+$  on the Nernst potential,  $IK_{Ca}$  current and EC  $V_m$ , we examined them in three different scenarios after Ach stimulation of EC. Figure 5.4 shows (a) extracellular  $K^+$ , (b)  $K^+$  Nernst potential ( $E_K$ ), (c)  $IK_{Ca}$  current and (d) EC  $V_m$  for uniform  $IK_{Ca}$  channels with leaky extracellular (Figure 5.4, *dashed lines*), localized  $IK_{Ca}$  channels with leaky extracellular (Figure 5.4, *solid lines*) and localized  $IK_{Ca}$  channels with no extracellular leak (Figure 5.4, *dotted lines*). As is evident, when higher  $K^+$  was present in the extracellular space, it depolarized the  $E_K$  for  $K^+$  and reduced  $IK_{Ca}$  current and the resulting EC hyperpolarization. However, even with low extracellular potassium and high  $IK_{Ca}$  current, a uniform distribution of  $IK_{Ca}$  channels (low  $IK_{Ca}$  current density) resulted in comparatively lower EC hyperpolarization (Figure 5.4d, *solid vs. dashed line*) than when the  $IK_{Ca}$  channels were localized with  $K^+$  leak.

### 5.3.4 Effect of potassium accumulation on pre stimulated arteries

Figure 5.5 shows the compartmental model results of SMC  $V_m$  (a) and SMC  $Ca^{2+}$  (b) to Ach stimulation of EC with prior SMC stimulation with NE during control (*solid lines*), no  $K^+$  accumulation (*dash-dot lines*), control with 50 %  $NaK_{\alpha 2}$  current (*dashed lines*) and higher extracellular  $K^+$  accumulation (*dotted lines*) created by less leaky extracellular volume. Figure 5.5c and d summarize the change in SMC  $V_m$  and SMC  $Ca^{2+}$  after EC stimulation with Ach for the different extracellular  $K^+$ . As is evident from the results, higher extracellular  $K^+$  reduced SMC hyperpolarization as well as SMC  $Ca^{2+}$  reduction whereas removal of  $K^+$  from the extracellular by increasing  $NaK_{\alpha 2}$  current or increasing extracellular  $K^+$  diffusivity, increased change in SMC  $V_m$  and SMC  $Ca^{2+}$ .

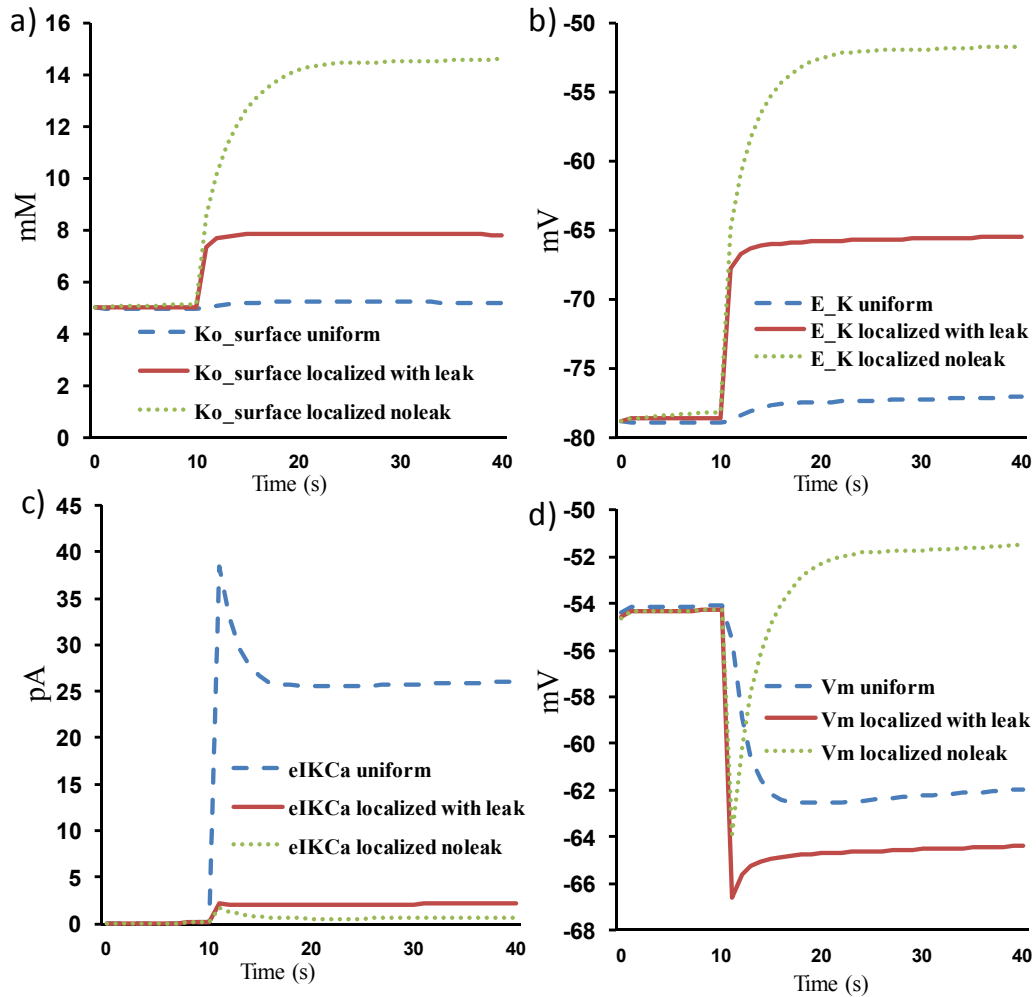


Figure 5.4 Extracellular  $K^+$  (a), Nernst potential of  $K^+$  (b),  $IK_{Ca}$  current (c) and  $V_m$  (d) for uniform  $IK_{Ca}$  channels with extracellular leak (dashed), localized  $IK_{Ca}$  with extracellular leak (solid) and localized  $IK_{Ca}$  with no leak (dotted) during Ach stimulation of EC in the 2D FEM.

### 5.3.5 Gap junction coupling vs. $K^+$ accumulation

To understand the relative importance of MEGJ coupling and  $K^+$  accumulation in EDHF action, Figure 5.6 shows SMC  $V_m$  (a), SMC  $Ca^{2+}$  (b) after EC stimulation in pressurized (prestimulated with NE) conditions for different levels of  $K^+$  accumulation and MEGJ blockade. When GJ coupling between EC and SMC was blocked (Figure 5.6, *dotted lines*), it cause an almost inhibition of EDHF action when stimulated by Ach. However,

due to the hyperpolarizing currents through SMC  $K_v$ ,  $K_{leak}$  and  $K_{ir}$  channels at resting stage, the resting potential of SMC was significantly lower ( $\sim 14mV$ ) than cases in which GJ coupling was present.

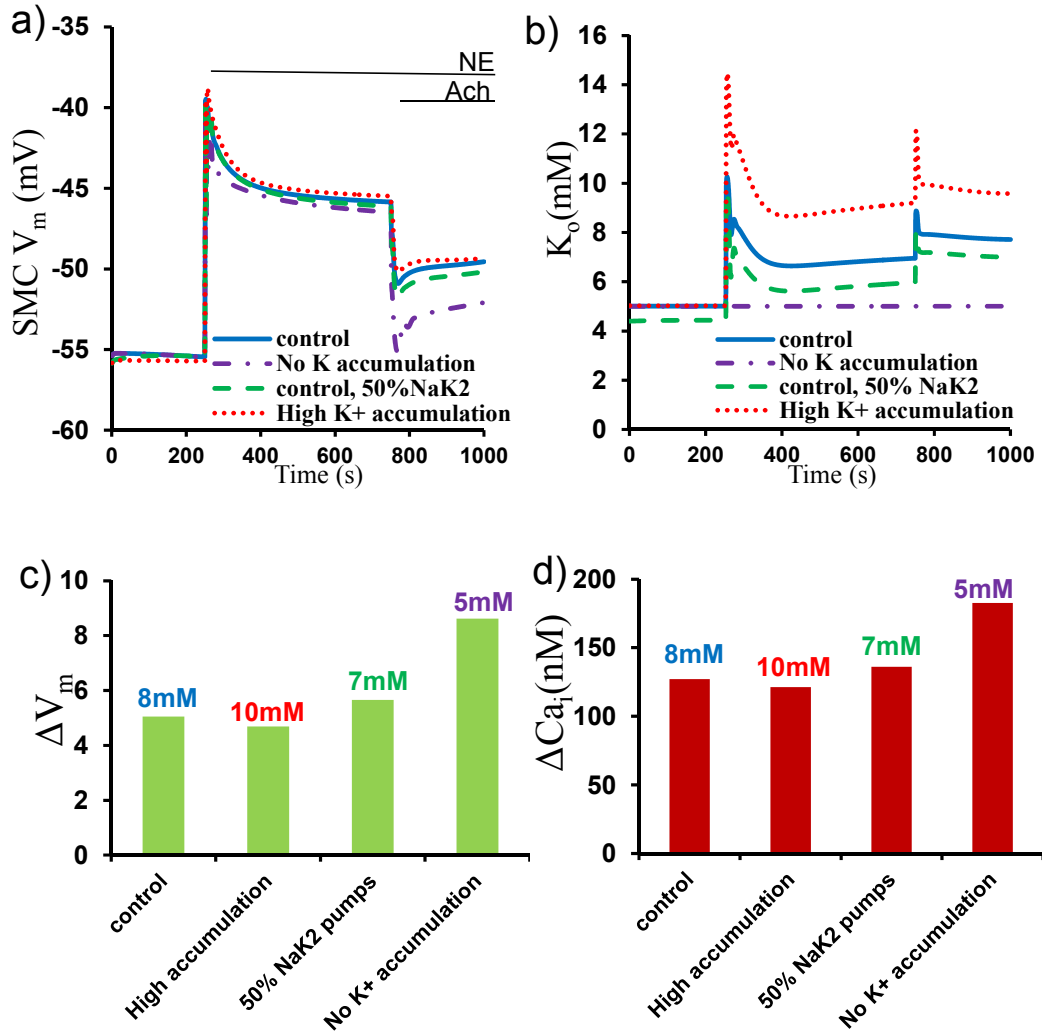


Figure 5.5 SMC  $V_m$  (a) , and extracellular  $K^+$  accumulation (b) for Ach stimulation of EC in prestimulated SMC for control (solid lines), No  $K^+$  accumulation (dash-dot lines), High  $K^+$  accumulation (less leaky extracellular)(dotted lines) and control with 50%  $NaK_{o2}$  current (dashed lines). Summary of change in SMC  $V_m$  (c) and SMC  $Ca^{2+}$  (d) after stimulation of EC with Ach is presented for different values of extracellular  $K^+$



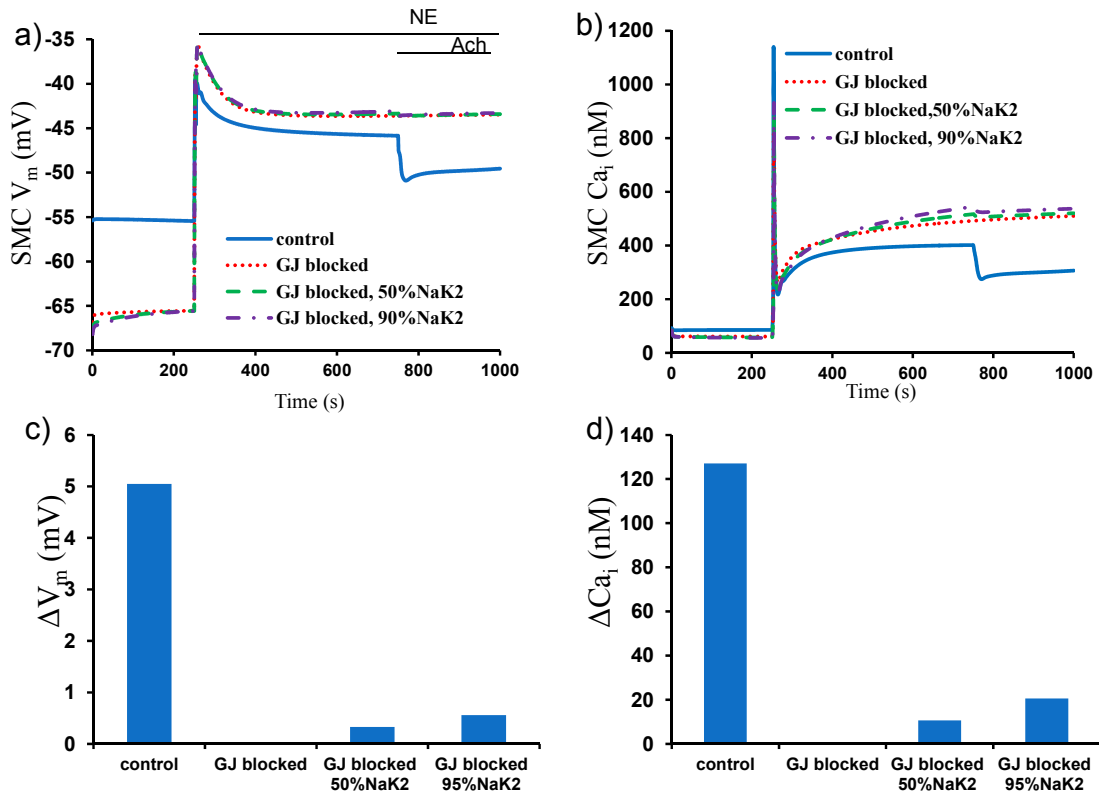


Figure 5.6 SMC  $V_m$  (a) and SMC  $Ca^{2+}$  (b) for Ach stimulation of EC in prestimulated SMC (d-f) for control (solid lines), MEGJ blocked (dotted lines), MEGJ blocked 50%  $NaK_{a2}$  current (dashed lines) and MEGJ coupling with 90%  $NaK_{a2}$  current (dash-dot lines).

Control simulation which has the combined action of MEGJ and  $K^+$  (Figure 5.6, *solid lines*) produce hyperpolarization and relaxation of SMC. However, during gap junction block conditions, increasing  $NaK_{a2}$  current by 50% (Figure 5.6, *dashed lines*) or 90% (Figure 5.6, *dash-dot lines*) of the total  $NaK$  current, did not cause any significant hyperpolarization to stimulation of EC. Results show that, while MEGJ coupling was necessary for EDHF action, the  $K^+$  accumulation actually opposed EC hyperpolarization and interfered with propagation of EDHF through MEGJs. The maximum EDHF action achieved in the absence of GJ coupling was less than 2mV of transient nature and only when the entire conductance of the  $NaK$  pumps was applied to the localized  $NaK_{a2}$  in the

SMC microdomain. Collectively, these results suggest a minor role for  $K^+$  accumulation to act as EDHF.

## **5.4 Discussion**

The primary aim of this study was to elucidate the mechanism of the essential EDHF action and the role of  $K^+$  accumulation in it. From the results, it appears that MEGJ is the major pathway for the propagation of EC hyperpolarization to SMC while  $K^+$  accumulation plays a minor role and in some concentrations inhibits the MEGJ pathway by reducing EC hyperpolarization.

### **5.4.1 Accumulation of $K^+$**

The first criterion for  $K^+$  to be a EDHF is the viability of its accumulation. Previous studies both experimental [192, 202] and theoretical [77, 203] have shown and predicted that following EC stimulation,  $K^+$  released by EC  $IK_{Ca}$  and  $SK_{Ca}$  channels can accumulate in the extracellular space in concentrations sufficient enough to activate  $NaK$  and  $K_{ir}$  in SMCs and cause SMC hyperpolarization in certain concentrations ranges. In both our models, we see that following Ach stimulation of ECs, both in resting as wells as arteries prestimulated with NE,  $K^+$  did accumulate in the small extracellular spaces between the EC MP and SMC MD and was governed by the leakiness of the extracellular space and other elements that remove  $K^+$  like  $NaK$  on both EC and SMCs (Figure 5.3 and 5.4b). In the presence of a leaky extracellular space,  $K^+$  accumulation requires the localization of  $IK_{Ca}$  channels very close to the extracellular spaces without which  $K^+$  accumulation of  $K^+$  was not feasible even with extremely small volumes of extracellular spaces and restricted diffusion to the bulk (Figure 5.3, Figure 5.4a).

#### 5.4.2 Role of myoendothelial gap junctions

After EC hyperpolarization, EDHF can be conducted to the SMCs by two means. Many studies have supported MEGJs as being EDHF [88-91, 116] although in some arterial beds, hyperpolarization is transferred from EC to SMC even in the presence of gap junction uncouplers like 18GA [93]. MEGJs provide a low resistance pathway for ionic communication between the two cell types. In fact, experiments have shown the absence of EDHF action itself in femoral arteries that do not express MEGJs [92]. Consistent with experimental observations, both the models showed a near abolishment of SMC hyperpolarization when gap junction communication was blocked (Figure 5.6a, dotted line). In many experiments,  $K^+$  elicited EDHF type responses required the presence of endothelium [116] suggesting that the relaxation responses cannot be attributed purely to  $K^+$  increase and opening of  $NaK$  and  $K_{ir}$ . The distribution of  $K_{ir}$  varies among different species and size of artery in the same species and has been shown to be functionally inactive in rat mesenteric arteries.

#### 5.4.3 Effect of potassium accumulation

The presence of high  $K^+$  (no extracellular leak) depolarized the  $K^+$  Nernst potential and reduced the potential gradient for  $K^+$  efflux which was evident from the reduction in  $IK_{Ca}$  current (Figure 5.4c, *solid vs. dashed line*) and subsequent reduction in EC  $V_m$  (Figure 5.4d, *solid vs. dashed line*). Interestingly,  $K^+$  efflux with uniform  $IK_{Ca}$  density caused the least extracellular accumulation of  $K^+$  and had the least inhibited  $IK_{Ca}$  current but its hyperpolarizing capacity was not as pronounced as when  $IK_{Ca}$  current was localized to MP (Figure 5.4d). There appears to be a window of  $K^+$  (rate of efflux from EC balanced by uptake from extracellular space) levels for which optimum

hyperpolarization was achieved (Figure 5.4d, *solid* line). This kind of effect has been seen in model for neurovascular coupling by Farr et al [204] where the effect of extracellular  $K^+$  change on SMC  $K_{ir}$  channels was accounted for. The  $E_K$  of  $K^+$  increased linearly with increase in extracellular  $K^+$  and for a small range (~10-12mM) it leads to hyperpolarization and relaxation by the activation of  $K_{ir}$ . Our models are more detailed and incorporated the change in  $E_K$  on all the  $K^+$  channels both in EC and SMC.

The reduction in EC  $V_m$  due to extracellular accumulation of  $K^+$  reduced SMC  $V_m$  (Figure 5.5a) due to the electrical coupling between the EC and SMC. In fact, as observed in EC, the removal of  $K^+$  from the extracellular space by either increasing the current of  $NaK_{\alpha 2}$  pumps (Figure 5.5, *dashed lines*) or by increasing the extracellular diffusivity of  $K^+$  (Figure 5.5, *dash-dot lines*), the hyperpolarization in the SMC as well as decrease in SMC  $Ca^{2+}$  could be restored close to control model values (Figure 5.5c and d). Immunofluorescence studies on rat arteries confirm the presence of both  $\alpha 1$  and  $\alpha 2$  isoforms of NaKATPase on SMCs. The  $\alpha 2$  isoform of NaKATPase is sensitive to low concentration of ouabain and high affinity for potassium ( $K_d = 4.8$  mM) [34]. Studies have shown that the  $NaK_{\alpha 2}$  pumps localize in certain locations on the SMC which facilitate the uptake of any increase in extracellular  $K^+$  [205-207]. The presence of these isoforms can make it more likely for any accumulating  $K^+$  to act as EDHF because the ubiquitous  $NaK_{\alpha 1}$  isoform found in most cells is saturated at the basal physiological concentration of extracellular  $K^+$  ( $K_d = 1.6$  mM) and therefore should be rather insensitive to any further increase in extracellular concentration of  $K^+$  [201]. However, the presence of high density  $NaK_{\alpha 2}$  hyperpolarized the resting potential during MEGJ blockade (Figure 5.5a) and reduced the intracellular SMC  $Na^+$  concentration (not shown) which inhibits the

increase of this current by any subsequent extracellular increase of  $K^+$ . Increasing  $NaK_{\alpha 2}$  density (50%) along with MEGJ coupling reduced the extracellular accumulation of potassium and led to slight greater EDHF action than control simulation (10%  $NaK_{\alpha 2}$  density) (Figure 5.5 a, *dashed vs. solid* line). However, 50%  $NaK_{\alpha 2}$  current alone (with MEGJ blocked) was not sufficient to produce a significant EDHF action (Figure 5.6, *dashed line*). The increase in EDHF action in terms of SMC  $V_m$  and SMC  $Ca^{2+}$  during 50% NaK with MEGJ (Figure 5.5 a, *dashed vs. solid* line) suggested that the presence of higher  $NaK_{\alpha 2}$  strengthened the MEGJ coupling between EC and SMC by removing  $K^+$  from the extracellular space and allowing more EC hyperpolarization (Figure 5.4d, *solid vs. dotted line*). Thus, again, it appears to be a balancing act to have higher  $NaK_{\alpha 2}$  in the IEL to reduce  $K^+$  accumulation to promote MEGJ pathway rather than cause EDHF through NaK current.

## 5.5 Limitations

Consistency was maintained with the previous two cell model with respect to parameter values and whole cell currents. Wherever available, we have used values from rat mesenteric artery data. The models behavior could change qualitatively and quantitatively with better tissues-specific parameter values, such as plasma membrane channel conductance, myoendothelial  $IP_3$  permeability, dimension and number of MPs. Expression of  $NaK_{\alpha 2}$  in the SMCs has been shown in the literature. However, because of the lack of quantitative measurements, we have assumed reasonable values for these variables or tested for a range of parameters defining these quantities. The compartmental models approximate well the electrical properties of the nearly iso potential endothelial and smooth muscle cells. The 2D model captures well the behavior

of  $\text{Ca}^{2+}$  inside the MP and  $\text{K}^+$  outside the cells and can account for spatial localization of channels or receptors. The biological variability of the vessels and different experimental conditions may contribute to the discrepancies and are difficult to take into account in a theoretical model.

## **5.6 Conclusion**

We have developed models to study the effect of  $\text{K}^+$  accumulation on SMC and EC  $V_m$  and  $\text{Ca}^{2+}$  and assess its role as EDHF. We find that even with high density of  $\text{NaK}_{\alpha 2}$  isoform localization to the microdomains in SMC,  $\text{K}^+$  alone was not able to produce significant SMC hyperpolarization. In addition, accumulation of  $\text{K}^+$  around EC reduces further release of  $\text{K}^+$  ions from the EC by its effect on  $E_K$  and inhibits  $\text{IK}_{\text{Ca}}$  current. It interferes with the transfer of hyperpolarization via MEGJ by reducing EC hyperpolarization. The blocking of MEGJ nearly abolished any SMC hyperpolarization. Purely  $\text{K}^+$  mediated EDHF action was very small and transient in nature.

**Acknowledgments:** This author is supported by the dissertation year fellowship from the University Graduate School, Florida International University

## **Chapter 6: Summary and future work**

### **6.1 Summary**

Movement of ions ( $\text{Ca}^{2+}$ ,  $\text{K}^+$ ,  $\text{Na}^+$  and  $\text{Cl}^-$ ) and second messenger molecules like inositol 1,4,5-trisphosphate inside and in between different cells is the basis of many signaling mechanisms in the microcirculation. In spite of the vast experimental efforts directed towards evaluation of these fluxes, it has been a challenge to establish their roles in many essential microcirculatory phenomena. A major limitation in investigations is the quantification of these intercellular fluxes experimentally. Thus, alternative hypotheses have often been proposed regarding the actual signaling mediator that contributes to a coordinated vessel behavior. Theoretical analyses and mathematical models can contribute in this discussion by providing estimates for the magnitude of these fluxes and their potential contribution in signaling. Recently, detailed theoretical models of calcium dynamics and plasma membrane electrophysiology have emerged to assist in the quantification of these intra and intercellular fluxes and enhance understanding of their physiological importance. The importance of gap junction communication in multicellular coordination has been established by the models in this dissertation. Ionic ( $\text{Ca}^{2+}$ ,  $\text{Na}^+$ ,  $\text{K}^+$ , and  $\text{Cl}^-$ ) and  $\text{IP}_3$  fluxes between cells have been estimated by the models. These fluxes can communicate changes upon mechanical or agonist stimulation in neighboring cells and their contribution to a variety of signaling phenomena have been examined.

#### **6.1.1 Conducted responses**

Rapid, long-range communication of local vasodilation or vasoconstriction (i.e. conducted responses) has been observed in many vascular beds and species. This

phenomenon is critical for matching blood perfusion to local metabolic demand. At this stage, most evidence suggests that conducted responses depend primarily on passive electrotonic spread. Theoretical [123] and experimental studies [81] have provided evidence for the importance of the endothelial layer in longitudinal signal transmission.

Through our model for conducted responses, we have examined the potential of intercellular  $\text{Ca}^{2+}$  and  $\text{IP}_3$  diffusion in conducted responses utilizing a multi cellular mathematical model. In the model, electrical coupling was the only signal strong enough to spread over long distances. Local  $\text{Ca}^{2+}$  transients did not propagate significantly along the vessel and were restricted to only a couple of cells away from the stimulus site. The limited  $\text{Ca}^{2+}$  spread was actually a result of  $\text{IP}_3$  rather than  $\text{Ca}^{2+}$  diffusion. This limited  $\text{IP}_3$  mediated  $\text{Ca}^{2+}$  mobilization in neighboring cells could amplify the total current generated at the local site thus contributing to the strength of the electrical signal spreading along the ECs. Thus, model simulations suggested a limited passive  $\text{Ca}^{2+}$  and  $\text{IP}_3$  spread which cannot facilitate signal transmission along the vessel but under some conditions can enhance distant responses by increasing local stimulus strength.

### **6.1.2 Myoendothelial projections**

Theoretical considerations suggest small gap junction fluxes for  $\text{Ca}^{2+}$  and  $\text{IP}_3$  and a limited role in spreading responses. The effect of these fluxes may, however, be amplified through a CICR mechanism. For example, weak  $\text{Ca}^{2+}$  and/or  $\text{IP}_3$  fluxes may be amplified and cause significant  $\text{Ca}^{2+}$  events near the gap junctions in the presence of localized ryanodine receptors (RyRs) and /or  $\text{IP}_3$ Rs. Although such microdomains have not been reported around homocellular gap junctions, MEGJs are usually colocalized with  $\text{IP}_3$ Rs on MPs. Using our model, we were able to show the importance of localized



MP domains inside the EC by predicting feedback achieved in terms of SMC  $V_m$  and SMC  $Ca^{2+}$  under physiological values of MEGJ resistance and suitable assumptions of  $IP_3R$  and  $IK_{Ca}$  localizations. Furthermore, the SMC originating signal that initiates  $Ca^{2+}$  mobilization in the MP has not been determined. Both  $Ca^{2+}$  and  $IP_3$  diffusion have been suggested to initiate this response. Although  $Ca^{2+}$  ions and  $IP_3$  have similar MEGJ permeability's the intercellular  $Ca^{2+}$  flux is probably not sufficient to mediate the feedback response. Our model simulations suggest that  $IP_3$  is more likely to be the mediator because of the localization of  $IP_3Rs$  in the MP (i.e. feedback is lost after blockade of intercellular  $IP_3$  diffusion but not of  $Ca^{2+}$ ).

### **6.1.3 Endothelium derived hyperpolarizing factor**

Using our models, we predicted the possibility of a locally initiated EC feedback during SMC stimulation. This feedback in the model is mediated via a non- nitric oxide, EDHF mechanism. Since its discovery, EDHF has been a topic of intense investigation. Being the dominant mode of vasorelaxation in the microcirculation, there is a lot of interest in the identity of this pathway. As is evident from the experiments and reviews, EDHF can operate via different pathways and/or factors in different tissues and species like EETs, CNP, CO,  $H_2O_2$ , NO,  $K^+$  ions, MEGJ coupling. However, the classical EDHF action which mandates the activation of  $IK_{Ca}$  and  $SK_{Ca}$  channel and EC hyperpolarization was studied by the models developed in this study. Two strong candidates for this form of EDHF action are electrical coupling through MEGJs and accumulation of  $K^+$  in the extracellular space and subsequent activation of SMC  $K_{ir}$  and both  $\alpha 1$  and  $\alpha 2$  isoforms of NaK pumps. It is difficult to isolate the two pathways in an experimental setup as  $K^+$  efflux is required for both EC hyperpolarization and activation of NaK pumps. Models

showed that  $K^+$  accumulation does occur but its effect is not as straightforward as it appears. The effect of  $K^+$  on various different entities (EC and SMC  $V_m$ ,  $E_K$ ,  $IK_{Ca}$ ,  $NaK_{\alpha 2}$ , SMC  $Na^+$ ) is explored in the models. 2D models offer the advantage of looking at spatial gradients of potassium in the extracellular space with/without leak outside of EC-SMC area. Model simulations showed that while  $K^+$  efflux was necessary for EDHF action, its accumulation, however, can inhibit its own future release by altering electrochemical gradients in both cells.

Experiments as well as theoretical modeling ascertain that intercellular communication is essential for the coordination of microcirculatory reactivity. Continuous electrical and ionic movement occurs between coupled cells which affects resting cell states and enables transmission of signals. Based on available measurements for gap junction resistances and expected intercellular gradients of different ions and  $IP_3$ , we have estimated the magnitudes of these fluxes in different scenarios. Electrical current through gap junctions (carried predominantly by  $K^+$  ions) is the primary signal that enables spreading responses.  $Ca^{2+}$  and  $IP_3$  fluxes are small and thus, their passive diffusion should have a limited effect on  $Ca^{2+}$  mobilization at distant sites. These weak fluxes may be adequate, however, to amplify local current in conducted responses. The effect of  $Ca^{2+}$  and  $IP_3$  diffusion can be amplified by the presence of molecular components like RyRs,  $IP_3$ Rs and  $IK_{Ca}$  channels in microdomains close to the gap junctions. Such localized signaling machinery exists in myoendothelial projections and enables an endothelial feedback response that moderates SMC constriction. Myoendothelial  $IP_3$  diffusion is more likely than  $Ca^{2+}$  to mediate this response. The models developed as a part of this dissertation are novel attempts designed to address

conducted responses in micro vessels, local EDHF mediated myoendothelial feedback and EDHF mechanisms. A strategy of integrative modeling in the vasculature is outlined that will allow linking macro scale pathophysiological responses to the underlying cellular mechanisms. The theoretical predictions from the models can give experimentalists a direction to design experiments around the more important aspects of these signaling pathways. Theoretical analyses can assist experimentation in elucidation of the complex mechanisms that regulate microcirculatory reactivity. These models can be modified as and when new data is presented with progress in experimentation and build more robust models with better predictive abilities. The current models can also be modified to examine different tissue and/or different state for e.g. hypertensive for which certain channel or receptor expression are altered.

#### **6.1.4 Compartmental methods vs. Finite element methods**

The two techniques used to develop the models in this dissertation are compartmental or lumped modeling and finite element modeling. Both modeling techniques offer their own advantages, therefore, microprojections and EDHF models were developed using both methods and the predictions compared to ensure the accuracy of model predictions. While the compartmental models are point model and do not provide information about spatial movement of ionic components, they approximate well the electrical properties of the nearly iso potential endothelial and smooth muscle cells. Nonlinear differential equations, which were coded in solved numerically using Gear's backward differentiation formula method for stiff differential equation systems (IMSL Numerical Library routine). The maximum time step was 4 ms, and tolerance for convergence was 0.0005. Finite element models provide spatial information about ions

and other second messengers and its accuracy is dependent on the size of mesh (level of discretization) used. Finer discretization required large computer memory space as well as long time for execution. Due to this, a larger time step (100ms) with lower error tolerance (0.0001) had to be used in the finite element model in order to obtain a convergence for the mesh size used in the model with the available computer memory limits. The accuracy of the model predictions is often a tradeoff between the model geometry and mesh size vs. the time step and error tolerance limit that can be used. In the present models, we used adaptive meshing which allows us to define finer meshes for small areas such as gap junctions and MP and coarse setting for meshes in EC and SMC blocks. We tried three different mesh sizes and finally used the least coarse setting. However, the result from coarser mesh sizes was not significantly different from the final setting chosen. To ascertain the accuracy of our results from the 2D model, they were compared at every stage to the compartmental model (using average values over a 2D space) and found to be in agreement with each other.

## **6.2 Future work**

Some of the current limitations of our models are being addressed in the next stage of our modeling efforts.

### **6.2.1 Calcium induced calcium release in IP<sub>3</sub> receptor**

In our current EC model [78], IP<sub>3</sub>R open probability is described using the probability curve shown in Figure 6.1. It has an IP<sub>3</sub> dependent activation and Ca<sup>2+</sup> dependent inactivation. However, many studies have shown that IP<sub>3</sub>R activation also depends on the Ca<sup>2+</sup> concentration in the cytosol and the IP<sub>3</sub>R receptor exhibits a bell shaped probability curve (Figure 6.2).

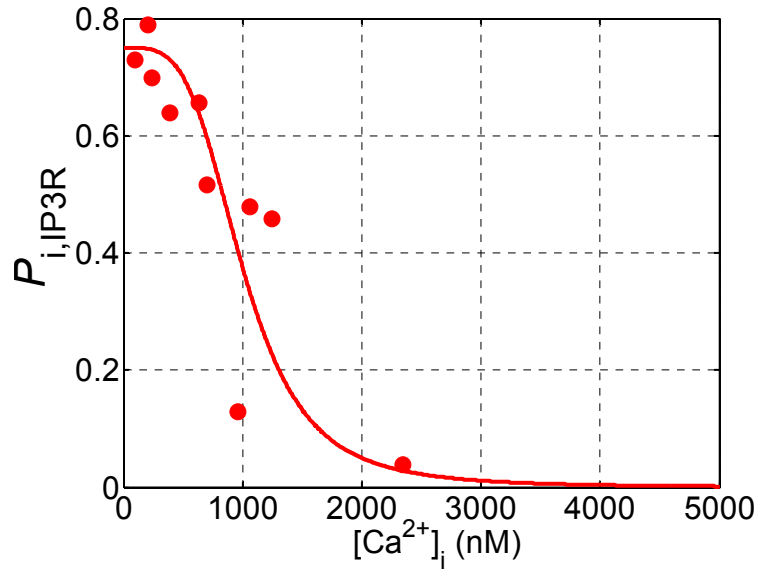


Figure 6.1 IP<sub>3</sub>R inactivation probability ( $P_{i,IP_3R}$ ) model fit (solid line) as a function of  $[Ca^{2+}]_i$  to experimental data (circles) from porcine aortic ECs [208]

As EC do not have RyRs which are traditionally known for their CICR response, incorporation of a  $Ca^{2+}$  dependent activation term in the IP<sub>3</sub>R will induce CICR in EC via these receptors which might amplify the role of  $Ca^{2+}$  diffusion in the SMC initiated EC mobilization which in the current models is fairly weak.

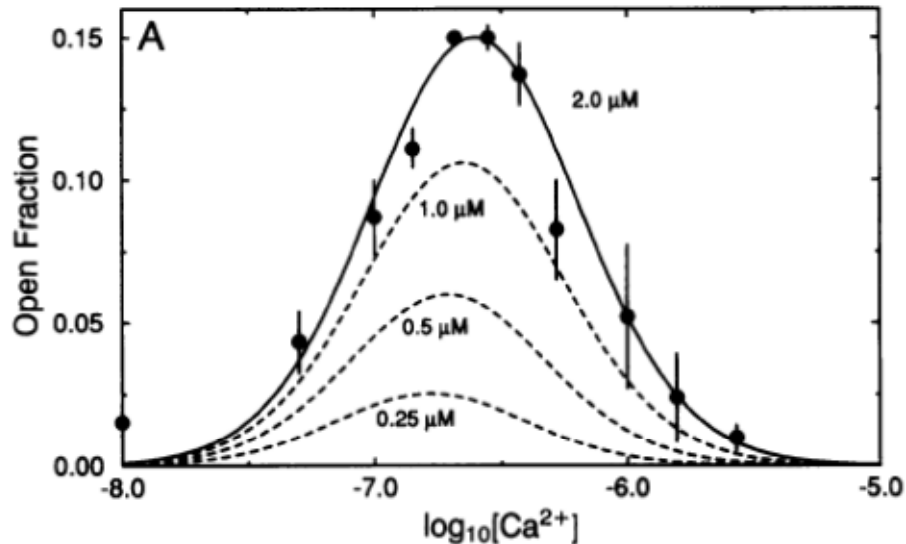


Figure 6.2 : Predicted open probability for IP<sub>3</sub>R with the inclusion of  $Ca^{2+}$  dependent activation [70]. The data for  $2\mu M$  IP<sub>3</sub>R is taken from Bezprozvanny et al [209].

We have modified the IP<sub>3</sub>R current in the model to account for Ca<sup>2+</sup> dependent activation. Initial results show that at low K<sub>d\_act</sub> ~ 130nM shows no effect for control conditions (0 nM basal IP<sub>3</sub>) because resting Ca<sup>2+</sup> in EC at resting is 130nM therefore the receptor is half saturated at resting Ca<sup>2+</sup> and very small effect for basal IP<sub>3</sub> concentrations between 30-40 nM. Using a higher K<sub>d\_act</sub> of 350 nM shows the effect of having CICR for higher basal levels (>30 nM) of IP<sub>3</sub>. However, it reduces the control feedback (from ~1.7 mV to ~0.5mV) (Figure 1a and 1b, pink dot) because now a higher stimulus is required to activate the IP<sub>3</sub>R. A careful parametric study of K<sub>d\_act</sub> values needs to be performed before selecting an optimum value for Ca<sup>2+</sup> activation which induced CICR without significantly affecting agonist activation.

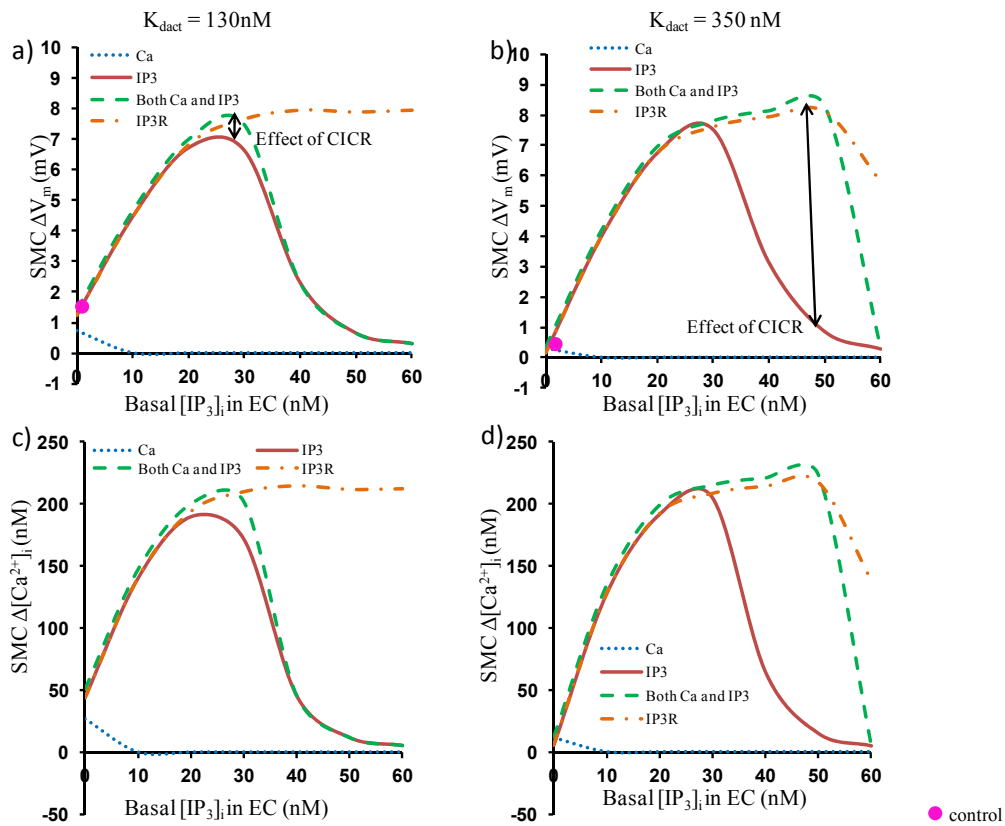
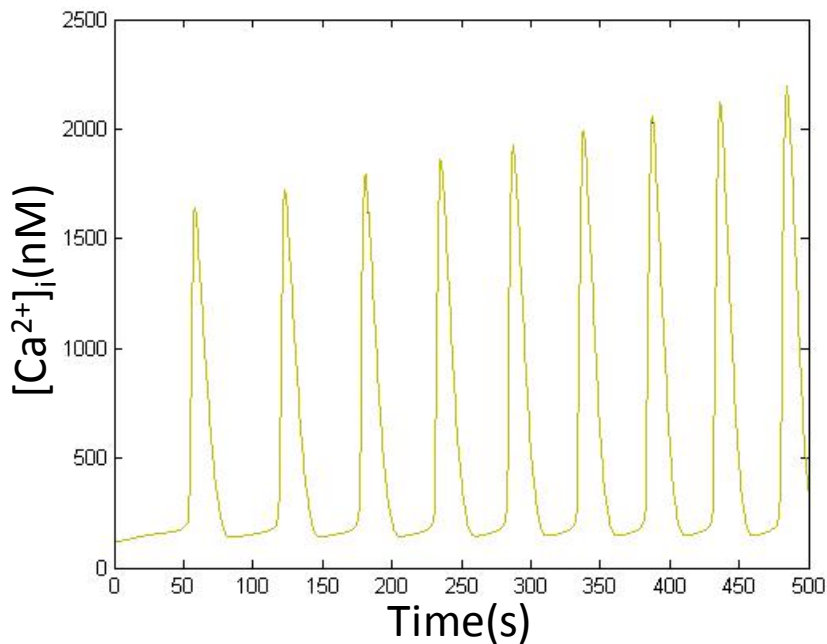


Figure 6.3 a) and b) show Ca<sup>2+</sup> mediated (or Ca<sup>2+</sup> diffusion from SMC to EC blocked, blue dotted), IP<sub>3</sub> mediated (or IP<sub>3</sub> diffusion from SMC to EC blocked, red solid), both Ca<sup>2+</sup> and IP<sub>3</sub> mediated (or

both  $IP_3$  and  $Ca^{2+}$  from SMC to EC blocked, green dashed) and  $IP_3R$  mediated (or  $IP_3R$  blocked, orange dash-dot) feedback for  $K_{d\_act}$  of 130 nM and 350nM respectively. Figure c and d show the respective SMC  $Ca^{2+}$  feedback.

### 6.2.2 Calcium oscillations and waves in endothelial and smooth muscle cells

After incorporating CICR in EC via  $IP_3Rs$  (section 6.2.1), we tried to see if this formalization can induce oscillations the EC. We divided our single EC model into several intracellular compartments and using a  $K_{d\_act}$  of 350 nM we can observe agonist induced oscillations in the EC as shown in Figure 6.4



**Figure 6.4**  $Ca^{2+}$  oscillations in the EC compartmental model after incorporation of CICR in the  $IP_3R$ . Spatial heterogeneity of receptors or differences in receptor activation can be introduced in the compartments to see if  $Ca^{2+}$  and/or  $IP_3$  diffusion along with CICR in  $IP_3Rs$  can generate waves in EC. Preliminary results show that when the receptor activation  $K_{d\_act}$  was varied linearly (350nM-450nM) across the 20 compartments from left to right in the EC, a wave like movement of  $Ca^{2+}$  is observed in the cells (Figure 6.5).

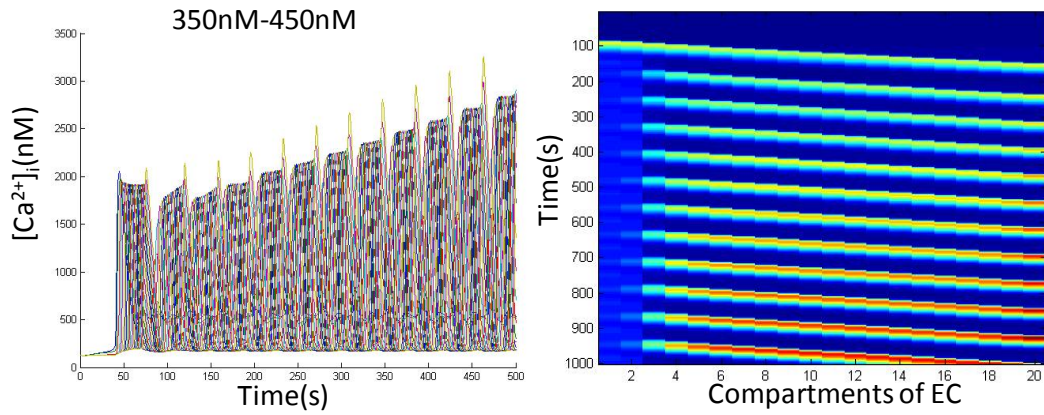


**Figure 6.5 Intracellular  $Ca^{2+}$  propagation in EC compartmental model**

We use the term ‘wavelike’ because this movement could also be the result of the different compartments oscillating with a phase difference causing a wavelike effect. However, more simulations need to be carried out to understand the mechanism behind these  $Ca^{2+}$  movements.



## 7. REFERENCES

1. Lloyd-Jones, D., et al., Heart disease and stroke statistics--2010 update: a report from the American Heart Association. *Circulation*, 2010. 121(7): p. e46-e215.
2. Silverthorn, D.U., *Human physiology : an integrated approach*. 3rd ed. 2004, San Francisco: Pearson/Benjamin Cummings. xxxii, 878 p.
3. Luo, C.H. and Y. Rudy, A dynamic model of the cardiac ventricular action potential. I. Simulations of ionic currents and concentration changes. *Circ Res*, 1994. 74(6): p. 1071-96.
4. Jafri, M.S., J.J. Rice, and R.L. Winslow, Cardiac Ca<sup>2+</sup> dynamics: the roles of ryanodine receptor adaptation and sarcoplasmic reticulum load. *Biophys J*, 1998. 74(3): p. 1149-68.
5. Saucerman, J.J. and A.D. McCulloch, Mechanistic systems models of cell signaling networks: a case study of myocyte adrenergic regulation. *Prog Biophys Mol Biol*, 2004. 85(2-3): p. 261-78.
6. ten Tusscher, K.H., et al., A model for human ventricular tissue. *Am J Physiol Heart Circ Physiol*, 2004. 286(4): p. H1573-89.
7. Shannon, T.R., et al., A mathematical treatment of integrated Ca dynamics within the ventricular myocyte. *Biophys J*, 2004. 87(5): p. 3351-71.
8. Nickerson, D., N. Smith, and P. Hunter, New developments in a strongly coupled cardiac electromechanical model. *Europace*, 2005. 7 Suppl 2: p. 118-27.
9. Noble, D., Modeling the heart--from genes to cells to the whole organ. *Science*, 2002. 295(5560): p. 1678-82.
10. Hunter, P. and P. Nielsen, A strategy for integrative computational physiology. *Physiology (Bethesda)*, 2005. 20: p. 316-25.
11. Hunter, P.J., A.J. Pullan, and B.H. Smaill, Modeling total heart function. *Annu Rev Biomed Eng*, 2003. 5: p. 147-77.
12. McCulloch, A.D., Modeling the human cardiome in silico. *J Nucl Cardiol*, 2000. 7(5): p. 496-9.

13. Winslow, R.L., et al., Electrophysiological modeling of cardiac ventricular function: from cell to organ. *Annu Rev Biomed Eng*, 2000. 2: p. 119-55.
14. Rudy, Y., From genome to physiome: integrative models of cardiac excitation. *Ann Biomed Eng*, 2000. 28(8): p. 945-50.
15. Saucerman, J.J., et al., Proarrhythmic consequences of a KCNQ1 AKAP-binding domain mutation: computational models of whole cells and heterogeneous tissue. *Circ Res*, 2004. 95(12): p. 1216-24.
16. Kapela, A., N. Tsoukias, and A. Bezerianos, New aspects of vulnerability in heterogeneous models of ventricular wall and its modulation by loss of cardiac sodium channel function. *Med Biol Eng Comput*, 2005. 43(3): p. 387-94.
17. Noble, D., Modeling the heart. *Physiology (Bethesda)*, 2004. 19: p. 191-7.
18. van Breemen, C. and K. Saida, Cellular mechanisms regulating  $[Ca^{2+}]_i$  smooth muscle. *Annu Rev Physiol*, 1989. 51: p. 315-29.
19. Nilius, B., F. Viana, and G. Droogmans, Ion channels in vascular endothelium. *Annu Rev Physiol*, 1997. 59: p. 145-70.
20. Carafoli, E., Calcium signaling: a tale for all seasons. *Proc Natl Acad Sci U S A*, 2002. 99(3): p. 1115-22.
21. Nilius, B. and G. Droogmans, Ion channels and their functional role in vascular endothelium. *Physiol Rev*, 2001. 81(4): p. 1415-59.
22. Sanders, K.M., Invited review: mechanisms of calcium handling in smooth muscles. *J Appl Physiol*, 2001. 91(3): p. 1438-49.
23. Berridge, M.J., Smooth muscle cell calcium activation mechanisms. *J Physiol*, 2008. 586(Pt 21): p. 5047-61.
24. Nilsson, H., M. Goldstein, and O. Nilsson, Adrenergic innervation and neurogenic response in large and small arteries and veins from the rat. *Acta Physiol Scand*, 1986. 126(1): p. 121-33.
25. Berridge, M.J., P. Lipp, and M.D. Bootman, The versatility and universality of calcium signalling. *Nat Rev Mol Cell Biol*, 2000. 1(1): p. 11-21.

26. Gollasch, M., et al., Ca<sup>2+</sup> channels, Ca<sup>2+</sup> sparks, and regulation of arterial smooth muscle function. *Z Kardiol*, 2000. 89 Suppl 2: p. 15-9.
27. Jaggar, J.H., et al., Ca<sup>2+</sup> channels, ryanodine receptors and Ca(2+)-activated K<sup>+</sup> channels: a functional unit for regulating arterial tone. *Acta Physiol Scand*, 1998. 164(4): p. 577-87.
28. Yuan, X.J., et al., Ionic currents in rat pulmonary and mesenteric arterial myocytes in primary culture and subculture. *Am J Physiol*, 1993. 264(2 Pt 1): p. L107-15.
29. Mistry, D.K. and C.J. Garland, Characteristics of single, large-conductance calcium-dependent potassium channels (BKCa) from smooth muscle cells isolated from the rabbit mesenteric artery. *J Membr Biol*, 1998. 164(2): p. 125-38.
30. Carrier, G.O., et al., Nitrovasodilators relax mesenteric microvessels by cGMP-induced stimulation of Ca-activated K channels. *Am J Physiol*, 1997. 273(1 Pt 2): p. H76-84.
31. Nakamura, Y., et al., Sodium-potassium pump current in smooth muscle cells from mesenteric resistance arteries of the guinea-pig. *J Physiol*, 1999. 519 Pt 1: p. 203-12.
32. Blanco, G. and R.W. Mercer, Isozymes of the Na-K-ATPase: heterogeneity in structure, diversity in function. *Am J Physiol*, 1998. 275(5 Pt 2): p. F633-50.
33. Juhaszova, M. and M.P. Blaustein, Distinct distribution of different Na<sup>+</sup> pump alpha subunit isoforms in plasmalemma. Physiological implications. *Ann N Y Acad Sci*, 1997. 834: p. 524-36.
34. Weston, A.H., et al., K<sup>+</sup>-induced hyperpolarization in rat mesenteric artery: identification, localization and role of Na<sup>+</sup>/K<sup>+</sup>-ATPases. *Br J Pharmacol*, 2002. 136(6): p. 918-26.
35. Leblanc, N. and J.R. Hume, Sodium current-induced release of calcium from cardiac sarcoplasmic reticulum. *Science*, 1990. 248(4953): p. 372-6.
36. Wier, W.G., Calcium transients during excitation-contraction coupling in mammalian heart: aequorin signals of canine Purkinje fibers. *Science*, 1980. 207(4435): p. 1085-7.
37. Jackson, W.F., Ion channels and vascular tone. *Hypertension*, 2000. 35(1 Pt 2): p. 173-8.
38. O'Donnell, M.E. and N.E. Owen, Regulation of ion pumps and carriers in vascular smooth muscle. *Physiol Rev*, 1994. 74(3): p. 683-721.

39. Arnon, A., J.M. Hamlyn, and M.P. Blaustein, Na<sup>(+)</sup> entry via store-operated channels modulates Ca<sup>(2+)</sup> signaling in arterial myocytes. *Am J Physiol Cell Physiol*, 2000. 278(1): p. C163-73.
40. Miller, J. and M. Carsten, Calcium homeostasis in smooth muscle., in *Cellular aspects of smooth muscle function.*, C. Kao and M. Carsten, Editors. 1997, Cambridge University Press.
41. Dedkova, E.N., et al., Mitochondrial calcium uptake stimulates nitric oxide production in mitochondria of bovine vascular endothelial cells. *Am J Physiol Cell Physiol*, 2004. 286(2): p. C406-15.
42. Volpe, P., et al., Calsequestrin is a component of smooth muscles: the skeletal- and cardiac-muscle isoforms are both present, although in highly variable amounts and ratios. *Biochem J*, 1994. 301 ( Pt 2): p. 465-9.
43. Wong, A.Y. and G.A. Klassen, A model of calcium regulation in smooth muscle cell. *Cell Calcium*, 1993. 14(3): p. 227-43.
44. Wong, A.Y. and G.A. Klassen, Endothelin-induced electrical activity and calcium dynamics in vascular smooth muscle cells: a model study. *Ann Biomed Eng*, 1996. 24(5): p. 547-60.
45. Gonzalez-Fernandez, J.M. and B. Ermentrout, On the origin and dynamics of the vasomotion of small arteries. *Math Biosci*, 1994. 119(2): p. 127-67.
46. Fink, C.C., B. Slepchenko, and L.M. Loew, Determination of time-dependent inositol-1,4,5-trisphosphate concentrations during calcium release in a smooth muscle cell. *Biophys J*, 1999. 77(1): p. 617-28.
47. Bennett, M.R., L. Farnell, and W.G. Gibson, A quantitative description of the contraction of blood vessels following the release of noradrenaline from sympathetic varicosities. *J Theor Biol*, 2005. 234(1): p. 107-22.
48. Parthimos, D., D.H. Edwards, and T.M. Griffith, Minimal model of arterial chaos generated by coupled intracellular and membrane Ca<sup>2+</sup> oscillators. *Am J Physiol*, 1999. 277(3 Pt 2): p. H1119-44.
49. Koenigsberger, M., et al., Ca<sup>2+</sup> dynamics in a population of smooth muscle cells: modeling the recruitment and synchronization. *Biophys J*, 2004. 87(1): p. 92-104.

50. Koenigsberger, M., R. Sauser, and J.J. Meister, Emergent properties of electrically coupled smooth muscle cells. *Bull Math Biol*, 2005. 67(6): p. 1253-72.
51. Jacobsen, J.C., et al., Activation of a cGMP-sensitive calcium-dependent chloride channel may cause transition from calcium waves to whole cell oscillations in smooth muscle cells. *Am J Physiol Heart Circ Physiol*, 2007. 293(1): p. H215-28.
52. Parthimos, D., D.H. Edwards, and T.M. Griffith, Shil'nikov homoclinic chaos is intimately related to type-III intermittency in isolated rabbit arteries: role of nitric oxide. *Phys Rev E Stat Nonlin Soft Matter Phys*, 2003. 67(5 Pt 1): p. 051922.
53. Parthimos, D., et al., Dynamics of a three-variable nonlinear model of vasomotion: comparison of theory and experiment. *Biophys J*, 2007. 93(5): p. 1534-56.
54. Yang, J., et al., The myogenic response in isolated rat cerebrovascular arteries: smooth muscle cell model. *Med Eng Phys*, 2003. 25(8): p. 691-709.
55. Edwards, A. and T.L. Pallone, Modification of cytosolic calcium signaling by subplasmalemmal microdomains. *Am J Physiol Renal Physiol*, 2007. 292(6): p. F1827-45.
56. Kapela, A., A. Bezerianos, and N.M. Tsoukias, A mathematical model of Ca<sup>2+</sup> dynamics in rat mesenteric smooth muscle cell: agonist and NO stimulation. *J Theor Biol*, 2008. 253(2): p. 238-60.
57. Hill, A.J., et al., A TRPC-like non-selective cation current activated by alpha 1-adrenoceptors in rat mesenteric artery smooth muscle cells. *Cell Calcium*, 2006. 40(1): p. 29-40.
58. Yang, J., et al., The myogenic response in isolated rat cerebrovascular arteries: vessel model. *Med Eng Phys*, 2003. 25(8): p. 711-7.
59. Yang, J., et al., Mathematical modeling of the nitric oxide/cGMP pathway in the vascular smooth muscle cell. *Am J Physiol Heart Circ Physiol*, 2005. 289(2): p. H886-97.
60. Adams, D.J. and M.A. Hill, Potassium channels and membrane potential in the modulation of intracellular calcium in vascular endothelial cells. *J Cardiovasc Electrophysiol*, 2004. 15(5): p. 598-610.
61. Tran, Q.K., K. Ohashi, and H. Watanabe, Calcium signalling in endothelial cells. *Cardiovasc Res*, 2000. 48(1): p. 13-22.

62. McSherry, I.N., et al., Endothelial cell  $\text{Ca}^{2+}$  increases are independent of membrane potential in pressurized rat mesenteric arteries. *Cell Calcium*, 2005. 38(1): p. 23-33.
63. Ahn, S.C., et al., Characteristics and a functional implication of  $\text{Ca}^{2+}$ -activated  $\text{K}^{+}$  current in mouse aortic endothelial cells. *Pflugers Arch*, 2004. 447(4): p. 426-35.
64. Coleman, H.A., M. Tare, and H.C. Parkington, Endothelial potassium channels, endothelium-dependent hyperpolarization and the regulation of vascular tone in health and disease. *Clin Exp Pharmacol Physiol*, 2004. 31(9): p. 641-9.
65. Chauhan, S., et al., NO contributes to EDHF-like responses in rat small arteries: a role for NO stores. *Cardiovasc Res*, 2003. 57(1): p. 207-16.
66. Chen, G. and D.W. Cheung, Modulation of endothelium-dependent hyperpolarization and relaxation to acetylcholine in rat mesenteric artery by cytochrome P450 enzyme activity. *Circ Res*, 1996. 79(4): p. 827-33.
67. Clark, S.G. and L.C. Fuchs, Role of nitric oxide and  $\text{Ca}^{++}$ -dependent  $\text{K}^{+}$  channels in mediating heterogeneous microvascular responses to acetylcholine in different vascular beds. *J Pharmacol Exp Ther*, 1997. 282(3): p. 1473-9.
68. Korngreen, A., V. Gold'shtein, and Z. Priel, A realistic model of biphasic calcium transients in electrically nonexcitable cells. *Biophys J*, 1997. 73(2): p. 659-73.
69. Goldbeter, A., G. Dupont, and M.J. Berridge, Minimal model for signal-induced  $\text{Ca}^{2+}$  oscillations and for their frequency encoding through protein phosphorylation. *Proc Natl Acad Sci U S A*, 1990. 87(4): p. 1461-5.
70. De Young, G.W. and J. Keizer, A single-pool inositol 1,4,5-trisphosphate-receptor-based model for agonist-stimulated oscillations in  $\text{Ca}^{2+}$  concentration. *Proc Natl Acad Sci U S A*, 1992. 89(20): p. 9895-9.
71. Jafri, M.S., et al., A membrane model for cytosolic calcium oscillations. A study using *Xenopus* oocytes. *Biophys J*, 1992. 63(1): p. 235-46.
72. Winston, F.K., L.E. Thibault, and E.J. Macarak, An analysis of the time-dependent changes in intracellular calcium concentration in endothelial cells in culture induced by mechanical stimulation. *J Biomech Eng*, 1993. 115(2): p. 160-8.
73. Wong, A.Y. and G.A. Klassen, A model of cytosolic calcium regulation and autacoids production in vascular endothelial cell. *Basic Res Cardiol*, 1992. 87: p. 317-332.

74. Wong, A.Y. and G.A. Klassen, A model of electrical activity and cytosolic calcium dynamics in vascular endothelial cells in response to fluid shear stress. *Ann Biomed Eng*, 1995. 23(6): p. 822-32.
75. Wiesner, T.F., B.C. Berk, and R.M. Nerem, A mathematical model of cytosolic calcium dynamics in human umbilical vein endothelial cells. *Am J Physiol*, 1996. 270(5 Pt 1): p. C1556-69.
76. Vu, T.K., et al., Molecular cloning of a functional thrombin receptor reveals a novel proteolytic mechanism of receptor activation. *Cell*, 1991. 64(6): p. 1057-68.
77. Schuster, A., J.L. Beny, and J.J. Meister, Modelling the electrophysiological endothelial cell response to bradykinin. *Eur Biophys J*, 2003. 32(4): p. 370-80.
78. Silva, H.S., A. Kapela, and N.M. Tsoukias, A mathematical model of plasma membrane electrophysiology and calcium dynamics in vascular endothelial cells. *Am J Physiol Cell Physiol*, 2007. 293(1): p. C277-93.
79. Hong, D., et al., Transport-dependent calcium signaling in spatially segregated cellular caveolar domains. *Am J Physiol Cell Physiol*, 2008. 294(3): p. C856-66.
80. Dora, K.A., M.P. Doyle, and B.R. Duling, Elevation of intracellular calcium in smooth muscle causes endothelial cell generation of NO in arterioles. *Proc Natl Acad Sci U S A*, 1997. 94(12): p. 6529-34.
81. Takano, H., et al., Spreading dilatation in rat mesenteric arteries associated with calcium-independent endothelial cell hyperpolarization. *J Physiol*, 2004. 556(Pt 3): p. 887-903.
82. Christ, G.J., et al., Gap junctions in vascular tissues. Evaluating the role of intercellular communication in the modulation of vasomotor tone. *Circ Res*, 1996. 79(4): p. 631-46.
83. Sandow, S.L., D.J. Gzik, and R.M. Lee, Arterial internal elastic lamina holes: relationship to function? *J Anat*, 2009. 214(2): p. 258-66.
84. Beny, J., Electrical coupling between smooth muscle cells and endothelial cells in pig coronary arteries. *Pflugers Arch*, 1997. 433(3): p. 364-7.
85. Emerson, G.G. and S.S. Segal, Electrical coupling between endothelial cells and smooth muscle cells in hamster feed arteries: role in vasomotor control. *Circ Res*, 2000. 87(6): p. 474-9.

86. Little, T.L., J. Xia, and B.R. Duling, Dye tracers define differential endothelial and smooth muscle coupling patterns within the arteriolar wall. *Circ Res*, 1995. 76(3): p. 498-504.
87. Sandow, S.L., et al., Developmental changes in myoendothelial gap junction mediated vasodilator activity in the rat saphenous artery. *J Physiol*, 2004. 556(Pt 3): p. 875-86.
88. Goto, K., et al., Critical role of gap junctions in endothelium-dependent hyperpolarization in rat mesenteric arteries. *Clin Exp Pharmacol Physiol*, 2002. 29(7): p. 595-602.
89. Hill, C.E., H. Hickey, and S.L. Sandow, Role of gap junctions in acetylcholine-induced vasodilation of proximal and distal arteries of the rat mesentery. *J Auton Nerv Syst*, 2000. 81(1-3): p. 122-7.
90. Sokoya, E.M., et al., Evidence for the involvement of myoendothelial gap junctions in EDHF-mediated relaxation in the rat middle cerebral artery. *Am J Physiol Heart Circ Physiol*, 2006. 291(1): p. H385-93.
91. Dora, K.A., et al., Myoendothelial gap junctions may provide the pathway for EDHF in mouse mesenteric artery. *J Vasc Res*, 2003. 40(5): p. 480-90.
92. Sandow, S.L., et al., Involvement of myoendothelial gap junctions in the actions of endothelium-derived hyperpolarizing factor. *Circ Res*, 2002. 90(10): p. 1108-13.
93. Dora, K.A., et al., Modulation of endothelial cell KCa3.1 channels during endothelium-derived hyperpolarizing factor signaling in mesenteric resistance arteries. *Circ Res*, 2008. 102(10): p. 1247-55.
94. Mather, S., et al., Rapid endothelial cell-selective loading of connexin 40 antibody blocks endothelium-derived hyperpolarizing factor dilation in rat small mesenteric arteries. *Circ Res*, 2005. 97(4): p. 399-407.
95. Brink, P.R., J. Ricotta, and G.J. Christ, Biophysical characteristics of gap junctions in vascular wall cells: implications for vascular biology and disease. *Braz J Med Biol Res*, 2000. 33(4): p. 415-22.
96. Sandow, S.L. and C.E. Hill, Incidence of myoendothelial gap junctions in the proximal and distal mesenteric arteries of the rat is suggestive of a role in endothelium-derived hyperpolarizing factor-mediated responses. *Circ Res*, 2000. 86(3): p. 341-6.
97. de Wit, C. and T.M. Griffith, Connexins and gap junctions in the EDHF phenomenon and conducted vasomotor responses. *Pflugers Arch*. 459(6): p. 897-914.



98. Yamamoto, Y., et al., Intercellular electrical communication among smooth muscle and endothelial cells in guinea-pig mesenteric arterioles. *J Physiol*, 2001. 535(Pt 1): p. 181-95.
99. Sandow, S.L., Factors, fiction and endothelium-derived hyperpolarizing factor. *Clin Exp Pharmacol Physiol*, 2004. 31(9): p. 563-70.
100. Feletou, M. and P.M. Vanhoutte, Endothelium-derived hyperpolarizing factor: where are we now? *Arterioscler Thromb Vasc Biol*, 2006. 26(6): p. 1215-25.
101. Sandow, S.L., et al., Structure, function, and endothelium-derived hyperpolarizing factor in the caudal artery of the SHR and WKY rat. *Arterioscler Thromb Vasc Biol*, 2003. 23(5): p. 822-8.
102. Luksha, L., S. Agewall, and K. Kublickiene, Endothelium-derived hyperpolarizing factor in vascular physiology and cardiovascular disease. *Atherosclerosis*, 2009. 202(2): p. 330-44.
103. Furchgott, R.F. and J.V. Zawadzki, The obligatory role of endothelial cells in the relaxation of arterial smooth muscle by acetylcholine. *Nature*, 1980. 288(5789): p. 373-6.
104. Angus, J.A. and T.M. Cocks, Vasodilatation and the discovery of endothelium-derived relaxing factor. *Med J Aust*, 1987. 146(5): p. 250-3.
105. Furchgott, R.F., Endothelium-derived relaxing factor: discovery, early studies, and identification as nitric oxide. *Biosci Rep*, 1999. 19(4): p. 235-51.
106. Proud, D., Nitric oxide and the common cold. *Curr Opin Allergy Clin Immunol*, 2005. 5(1): p. 37-42.
107. Vanhoutte, P.M., Vascular biology. Old-timer makes a comeback. *Nature*, 1998. 396(6708): p. 213, 215-6.
108. Zhao, Y., et al., A molecular basis for nitric oxide sensing by soluble guanylate cyclase. *Proc Natl Acad Sci U S A*, 1999. 96(26): p. 14753-8.
109. Bunting, S., et al., Arterial walls generate from prostaglandin endoperoxides a substance (prostaglandin X) which relaxes strips of mesenteric and coeliac arteries and inhibits platelet aggregation. *Prostaglandins*, 1976. 12(6): p. 897-913.
110. Smith, W.L., D.L. DeWitt, and R.M. Garavito, Cyclooxygenases: structural, cellular, and molecular biology. *Annu Rev Biochem*, 2000. 69: p. 145-82.

111. Chen, G., H. Suzuki, and A.H. Weston, Acetylcholine releases endothelium-derived hyperpolarizing factor and EDRF from rat blood vessels. *Br J Pharmacol*, 1988. 95(4): p. 1165-74.
112. Edwards, G., M. Feletou, and A.H. Weston, Endothelium-derived hyperpolarising factors and associated pathways: a synopsis. *Pflugers Arch*. 459(6): p. 863-79.
113. Busse, R., et al., EDHF: bringing the concepts together. *Trends Pharmacol Sci*, 2002. 23(8): p. 374-80.
114. Heberlein, K.R., A.C. Straub, and B.E. Isakson, The myoendothelial junction: breaking through the matrix? *Microcirculation*, 2009. 16(4): p. 307-22.
115. Shimokawa, H., et al., The importance of the hyperpolarizing mechanism increases as the vessel size decreases in endothelium-dependent relaxations in rat mesenteric circulation. *J Cardiovasc Pharmacol*, 1996. 28(5): p. 703-11.
116. Edwards, G., et al., Role of gap junctions in the responses to EDHF in rat and guinea-pig small arteries. *Br J Pharmacol*, 1999. 128(8): p. 1788-94.
117. Kansui, Y., C.J. Garland, and K.A. Dora, Enhanced spontaneous Ca<sup>2+</sup> events in endothelial cells reflect signalling through myoendothelial gap junctions in pressurized mesenteric arteries. *Cell Calcium*, 2008. 44(2): p. 135-46.
118. Ledoux J, T.M., Boney AD, Hannah RM, Tallini YN, Kotlikoff MI and Nelson MT, Ca<sup>2+</sup> pulsars: spatially restricted, IP3R-mediated Ca<sup>2+</sup> release important for endothelial function. *J. Vasc. Res.*, 2008. 45(3).
119. Ledoux, J., et al., Functional architecture of inositol 1,4,5-trisphosphate signaling in restricted spaces of myoendothelial projections. *Proc Natl Acad Sci U S A*, 2008. 105(28): p. 9627-32.
120. Tran, C.H.T., et al., Endothelial Ca<sup>2+</sup> wavelets and the induction of myoendothelial feedback. *Am J Physiol Cell Physiol*, 2011. (In review C-00418-2011).
121. Schuster, A., et al., Simultaneous arterial calcium dynamics and diameter measurements: application to myoendothelial communication. *Am J Physiol Heart Circ Physiol*, 2001. 280(3): p. H1088-96.
122. Lamboley, M., et al., Evidence for signaling via gap junctions from smooth muscle to endothelial cells in rat mesenteric arteries: possible implication of a second messenger. *Cell Calcium*, 2005. 37(4): p. 311-20.

123. Diep, H.K., et al., Defining electrical communication in skeletal muscle resistance arteries: a computational approach. *J Physiol*, 2005. 568(Pt 1): p. 267-81.
124. Christ, G.J., P.R. Brink, and S.V. Ramanan, Dynamic gap junctional communication: a delimiting model for tissue responses. *Biophys J*, 1994. 67(3): p. 1335-44.
125. Hille, B., Ionic channels of excitable membranes. 2nd ed. 2001, Sunderland, Mass.: Sinauer Associates. xiii, 607 p.
126. Jacobsen, J.C., et al., A model of smooth muscle cell synchronization in the arterial wall. *Am J Physiol Heart Circ Physiol*, 2007. 293(1): p. H229-37.
127. Koenigsberger, M., et al., Role of the endothelium on arterial vasomotion. *Biophys J*, 2005. 88(6): p. 3845-54.
128. Kapela, A., S. Nagaraja, and N.M. Tsoukias, A mathematical model of vasoreactivity in rat mesenteric arterioles. II. Conducted vasoreactivity. *Am J Physiol Heart Circ Physiol*, 2010. 298(1): p. H52-65.
129. Kapela, A., A. Bezerianos, and N.M. Tsoukias, A mathematical model of vasoreactivity in rat mesenteric arterioles: I. Myoendothelial communication. *Microcirculation*, 2009. 16(8): p. 694-713.
130. Krogh, A., G.A. Harrop, and P.B. Rehberg, Studies on the physiology of capillaries: III. The innervation of the blood vessels in the hind legs of the frog. *J Physiol*, 1922. 56(3-4): p. 179-89.
131. Duling, B.R. and R.M. Berne, Propagated vasodilation in the microcirculation of the hamster cheek pouch. *Circ Res*, 1970. 26(2): p. 163-70.
132. Segal, S.S., Microvascular recruitment in hamster striated muscle: role for conducted vasodilation. *Am J Physiol*, 1991. 261(1 Pt 2): p. H181-9.
133. Gustafsson, F. and N. Holstein-Rathlou, Conducted vasomotor responses in arterioles: characteristics, mechanisms and physiological significance. *Acta Physiol Scand*, 1999. 167(1): p. 11-21.
134. Dora, K.A., J. Xia, and B.R. Duling, Endothelial cell signaling during conducted vasomotor responses. *Am J Physiol Heart Circ Physiol*, 2003. 285(1): p. H119-26.

135. Segal, S.S., D.G. Welsh, and D.T. Kurjiaka, Spread of vasodilatation and vasoconstriction along feed arteries and arterioles of hamster skeletal muscle. *J Physiol*, 1999. 516 ( Pt 1): p. 283-91.
136. Segal, S.S., Regulation of blood flow in the microcirculation. *Microcirculation*, 2005. 12(1): p. 33-45.
137. Pries, A.R., T.W. Secomb, and P. Gaehtgens, Structural adaptation and stability of microvascular networks: theory and simulations. *Am J Physiol*, 1998. 275(2 Pt 2): p. H349-60.
138. Takano, H., K.A. Dora, and C.J. Garland, Spreading vasodilatation in resistance arteries. *J Smooth Muscle Res*, 2005. 41(6): p. 303-11.
139. Tallini, Y.N., et al., Propagated endothelial Ca<sup>2+</sup> waves and arteriolar dilation in vivo: measurements in Cx40BAC GCaMP2 transgenic mice. *Circ Res*, 2007. 101(12): p. 1300-9.
140. Hermsmeyer, R.K. and T.L. Thompson, Vasodilator coordination via membrane conduction. *Am J Physiol Heart Circ Physiol*, 2007. 293(3): p. H1320-1.
141. Crane, G.J., T.O. Neild, and S.S. Segal, Contribution of active membrane processes to conducted hyperpolarization in arterioles of hamster cheek pouch. *Microcirculation*, 2004. 11(5): p. 425-33.
142. Budel, S., I.S. Bartlett, and S.S. Segal, Homocellular conduction along endothelium and smooth muscle of arterioles in hamster cheek pouch: unmasking an NO wave. *Circ Res*, 2003. 93(1): p. 61-8.
143. Domeier, T.L. and S.S. Segal, Electromechanical and pharmacomechanical signalling pathways for conducted vasodilatation along endothelium of hamster feed arteries. *J Physiol*, 2007. 579(Pt 1): p. 175-86.
144. Uhrenholt, T.R., T.L. Domeier, and S.S. Segal, Propagation of calcium waves along endothelium of hamster feed arteries. *Am J Physiol Heart Circ Physiol*, 2007. 292(3): p. H1634-40.
145. Figueroa, X., et al., Are voltage-dependent ion channels involved in the endothelial cell control of vasomotor tone? *Am J Physiol Heart Circ Physiol*, 2007.
146. Hirst, G.D. and T.O. Neild, An analysis of excitatory junctional potentials recorded from arterioles. *J Physiol*, 1978. 280: p. 87-104.

147. Crane, G.J., M.L. Hines, and T.O. Neild, Simulating the spread of membrane potential changes in arteriolar networks. *Microcirculation*, 2001. 8(1): p. 33-43.
148. Haug, S.J. and S.S. Segal, Sympathetic neural inhibition of conducted vasodilatation along hamster feed arteries: complementary effects of alpha1- and alpha2-adrenoreceptor activation. *J Physiol*, 2005. 563(Pt 2): p. 541-55.
149. Haas, T.L. and B.R. Duling, Morphology favors an endothelial cell pathway for longitudinal conduction within arterioles. *Microvasc Res*, 1997. 53(2): p. 113-20.
150. Sandow, S.L., et al., Expression of homocellular and heterocellular gap junctions in hamster arterioles and feed arteries. *Cardiovasc Res*, 2003. 60(3): p. 643-53.
151. Koenigsberger, M., et al., Effects of arterial wall stress on vasomotion. *Biophys J*, 2006. 91(5): p. 1663-74.
152. Figueroa, X.F., B.E. Isakson, and B.R. Duling, Connexins: gaps in our knowledge of vascular function. *Physiology (Bethesda)*, 2004. 19: p. 277-84.
153. Moore, L.K. and J.M. Burt, Gap junction function in vascular smooth muscle: influence of serotonin. *Am J Physiol*, 1995. 269(4 Pt 2): p. H1481-9.
154. Van Rijen, H., et al., Gap junctions in human umbilical cord endothelial cells contain multiple connexins. *Am J Physiol*, 1997. 272(1 Pt 1): p. C117-30.
155. Lidington, D., Y. Ouellette, and K. Tyml, Endotoxin increases intercellular resistance in microvascular endothelial cells by a tyrosine kinase pathway. *J Cell Physiol*, 2000. 185(1): p. 117-25.
156. Blatter, L.A., et al., Simultaneous measurements of Ca<sup>2+</sup> and nitric oxide in bradykinin-stimulated vascular endothelial cells. *Circ Res*, 1995. 76(5): p. 922-4.
157. Mizuno, O., et al., Stimulus-specific alteration of the relationship between cytosolic Ca(2+) transients and nitric oxide production in endothelial cells ex vivo. *Br J Pharmacol*, 2000. 130(5): p. 1140-6.
158. Dong, X.H., et al., Nanomolar level of ouabain increases intracellular calcium to produce nitric oxide in rat aortic endothelial cells. *Clin Exp Pharmacol Physiol*, 2004. 31(5-6): p. 276-83.

159. Ayajiki, K., et al., Intracellular pH and tyrosine phosphorylation but not calcium determine shear stress-induced nitric oxide production in native endothelial cells. *Circ Res*, 1996. 78(5): p. 750-8.
160. Tsoukias, N.M. and A.S. Popel, A model of nitric oxide capillary exchange. *Microcirculation*, 2003. 10(6): p. 479-95.
161. Crane, G.J. and T.O. Neild, An equation describing spread of membrane potential changes in a short segment of blood vessel. *Phys Med Biol*, 1999. 44(10): p. N217-21.
162. Figueroa, X.F., et al., Central role of connexin40 in the propagation of electrically activated vasodilation in mouse cremasteric arterioles in vivo. *Circ Res*, 2003. 92(7): p. 793-800.
163. Wolfle, S.E., et al., Connexin45 cannot replace the function of connexin40 in conducting endothelium-dependent dilations along arterioles. *Circ Res*, 2007. 101(12): p. 1292-9.
164. Emerson, G.G., T.O. Neild, and S.S. Segal, Conduction of hyperpolarization along hamster feed arteries: augmentation by acetylcholine. *Am J Physiol Heart Circ Physiol*, 2002. 283(1): p. H102-9.
165. Winter, P. and K.A. Dora, Spreading dilatation to luminal perfusion of ATP and UTP in rat isolated small mesenteric arteries. *J Physiol*, 2007. 582(Pt 1): p. 335-47.
166. Fleming, I., Bobbing along on the crest of a wave: NO ascends hamster cheek pouch arterioles. *Circ Res*, 2003. 93(1): p. 9-11.
167. Doyle, M.P. and B.R. Duling, Acetylcholine induces conducted vasodilation by nitric oxide-dependent and -independent mechanisms. *Am J Physiol*, 1997. 272(3 Pt 2): p. H1364-71.
168. Welsh, D.G., et al., Are voltage-dependent ion channels involved in the endothelial cell control of vasomotor tone? *AJP Heart and Circulatory Physiology*, 2007.
169. Sanderson, M.J., et al., Mechanisms and function of intercellular calcium signaling. *Mol Cell Endocrinol*, 1994. 98(2): p. 173-87.
170. Sneyd, J., A.C. Charles, and M.J. Sanderson, A model for the propagation of intercellular calcium waves. *Am J Physiol*, 1994. 266(1 Pt 1): p. C293-302.
171. Keener, J.P. and J. Sneyd, *Mathematical physiology. Interdisciplinary applied mathematics*. 1998, New York: Springer. viii, 766 p.

172. Luckhoff, A. and R. Busse, Calcium influx into endothelial cells and formation of endothelium-derived relaxing factor is controlled by the membrane potential. *Pflugers Arch*, 1990. 416(3): p. 305-11.
173. Gustafsson, F. and N.H. Holstein-Rathlou, Angiotensin II modulates conducted vasoconstriction to norepinephrine and local electrical stimulation in rat mesenteric arterioles. *Cardiovasc Res*, 1999. 44(1): p. 176-84.
174. Sandow, S.L., et al., What'S where and why at a vascular myoendothelial microdomain signalling complex. *Clin Exp Pharmacol Physiol*, 2009. 36(1): p. 67-76.
175. Hwa, J.J., et al., Comparison of acetylcholine-dependent relaxation in large and small arteries of rat mesenteric vascular bed. *Am J Physiol*, 1994. 266(3 Pt 2): p. H952-8.
176. Moore, D.H. and H. Ruska, The fine structure of capillaries and small arteries. *J Biophys Biochem Cytol*, 1957. 3(3): p. 457-62.
177. Sandow, S.L., et al., Spatial separation of endothelial small- and intermediate-conductance calcium-activated potassium channels (K(Ca)) and connexins: possible relationship to vasodilator function? *J Anat*, 2006. 209(5): p. 689-98.
178. Isakson, B.E., Localized expression of an Ins(1,4,5)P3 receptor at the myoendothelial junction selectively regulates heterocellular Ca<sup>2+</sup> communication. *J Cell Sci*, 2008. 121(Pt 21): p. 3664-73.
179. Crane, G.J., et al., Small- and intermediate-conductance calcium-activated K<sup>+</sup> channels provide different facets of endothelium-dependent hyperpolarization in rat mesenteric artery. *J Physiol*, 2003. 553(Pt 1): p. 183-9.
180. Bychkov, R., et al., Characterization of a charybdotoxin-sensitive intermediate conductance Ca<sup>2+</sup>-activated K<sup>+</sup> channel in porcine coronary endothelium: relevance to EDHF. *Br J Pharmacol*, 2002. 137(8): p. 1346-54.
181. Allbritton, N.L., T. Meyer, and L. Stryer, Range of messenger action of calcium ion and inositol 1,4,5-trisphosphate. *Science*, 1992. 258(5089): p. 1812-5.
182. Oishi, H., et al., Cytosolic-free calcium in smooth-muscle and endothelial cells in an intact arterial wall from rat mesenteric artery in vitro. *Cell Calcium*, 2001. 30(4): p. 261-7.

183. Isakson, B.E., S.I. Ramos, and B.R. Duling, Ca<sup>2+</sup> and inositol 1,4,5-trisphosphate-mediated signaling across the myoendothelial junction. *Circ Res*, 2007. 100(2): p. 246-54.
184. Diambra, L. and J.S. Marchant, Localization and socialization: experimental insights into the functional architecture of IP3 receptors. *Chaos*, 2009. 19(3): p. 037103.
185. Taylor, C.W., R. Taufiq Ur, and E. Pantazaka, Targeting and clustering of IP3 receptors: key determinants of spatially organized Ca<sup>2+</sup> signals. *Chaos*, 2009. 19(3): p. 037102.
186. Doughty, J.M., F. Plane, and P.D. Langton, Charybdotoxin and apamin block EDHF in rat mesenteric artery if selectively applied to the endothelium. *Am J Physiol*, 1999. 276(3 Pt 2): p. H1107-12.
187. Feletou, M., The Endothelium: Part 2: EDHF-Mediated Responses “The Classical Pathway”. *Colloquium Series on Integrated Systems Physiology: From Molecule to Function to Disease*, 2011. #20: p. 208.
188. Coleman, H.A., M. Tare, and H.C. Parkington, K<sup>+</sup> currents underlying the action of endothelium-derived hyperpolarizing factor in guinea-pig, rat and human blood vessels. *J Physiol*, 2001. 531(Pt 2): p. 359-73.
189. Eichler, I., et al., Selective blockade of endothelial Ca<sup>2+</sup>-activated small- and intermediate-conductance K<sup>+</sup>-channels suppresses EDHF-mediated vasodilation. *Br J Pharmacol*, 2003. 138(4): p. 594-601.
190. Andersson, D.A., et al., Effects of inhibitors of small- and intermediate-conductance calcium-activated potassium channels, inwardly-rectifying potassium channels and Na<sup>(+)</sup>/K<sup>(+)</sup> ATPase on EDHF relaxations in the rat hepatic artery. *Br J Pharmacol*, 2000. 129(7): p. 1490-6.
191. Chen, G. and D.W. Cheung, Effect of K<sup>(+)</sup>-channel blockers on ACh-induced hyperpolarization and relaxation in mesenteric arteries. *Am J Physiol*, 1997. 272(5 Pt 2): p. H2306-12.
192. Edwards, G., et al., K<sup>+</sup> is an endothelium-derived hyperpolarizing factor in rat arteries. *Nature*, 1998. 396(6708): p. 269-72.
193. Siegl, D., et al., Myoendothelial coupling is not prominent in arterioles within the mouse cremaster microcirculation in vivo. *Circ Res*, 2005. 97(8): p. 781-8.



194. Dora, K.A. and C.J. Garland, Properties of smooth muscle hyperpolarization and relaxation to K<sup>+</sup> in the rat isolated mesenteric artery. *Am J Physiol Heart Circ Physiol*, 2001. 280(6): p. H2424-9.
195. Zygmunt, P.M., et al., Differential actions of anandamide, potassium ions and endothelium-derived hyperpolarizing factor in guinea-pig basilar artery. *Naunyn Schmiedebergs Arch Pharmacol*, 2000. 361(5): p. 535-42.
196. Quignard, J.F., et al., Role of endothelial cell hyperpolarization in EDHF-mediated responses in the guinea-pig carotid artery. *Br J Pharmacol*, 2000. 129(6): p. 1103-12.
197. Coleman, H.A., M. Tare, and H.C. Parkington, EDHF is not K<sup>+</sup> but may be due to spread of current from the endothelium in guinea pig arterioles. *Am J Physiol Heart Circ Physiol*, 2001. 280(6): p. H2478-83.
198. Seol, G.H., et al., Inhibition of endothelium-dependent vasorelaxation by extracellular K(+): a novel controlling signal for vascular contractility. *Am J Physiol Heart Circ Physiol*, 2004. 286(1): p. H329-39.
199. Lacy, P.S., et al., Evidence against potassium as an endothelium-derived hyperpolarizing factor in rat mesenteric small arteries. *Br J Pharmacol*, 2000. 129(3): p. 605-11.
200. Allen, T., et al., Smooth muscle membrane potential modulates endothelium-dependent relaxation of rat basilar artery via myo-endothelial gap junctions. *J Physiol*, 2002. 545(Pt 3): p. 975-86.
201. Segall, L., S.E. Daly, and R. Blostein, Mechanistic basis for kinetic differences between the rat alpha 1, alpha 2, and alpha 3 isoforms of the Na,K-ATPase. *J Biol Chem*, 2001. 276(34): p. 31535-41.
202. Richards, G.R., et al., Suppression of K(+)-induced hyperpolarization by phenylephrine in rat mesenteric artery: relevance to studies of endothelium-derived hyperpolarizing factor. *Br J Pharmacol*, 2001. 134(1): p. 1-5.
203. Brace, R.A. and D.K. Anderson, Predicting transient and steady-state changes in resting membrane potential. *J Appl Physiol*, 1973. 35(1): p. 90-4.
204. Farr, H. and T. David, Models of neurovascular coupling via potassium and EET signalling. *J Theor Biol*. 286(1): p. 13-23.

205. Juhaszova, M. and M.P. Blaustein, Na<sup>+</sup> pump low and high ouabain affinity alpha subunit isoforms are differently distributed in cells. *Proc Natl Acad Sci U S A*, 1997. 94(5): p. 1800-5.
206. Blaustein, M.P. and V.A. Golovina, Structural complexity and functional diversity of endoplasmic reticulum Ca(2+) stores. *Trends Neurosci*, 2001. 24(10): p. 602-8.
207. Blaustein, M.P., et al., How does salt retention raise blood pressure? *Am J Physiol Regul Integr Comp Physiol*, 2006. 290(3): p. R514-23.
208. Carter, T.D. and D. Ogden, Kinetics of Ca<sup>2+</sup> release by InsP<sub>3</sub> in pig single aortic endothelial cells: evidence for an inhibitory role of cytosolic Ca<sup>2+</sup> in regulating hormonally evoked Ca<sup>2+</sup> spikes. *J Physiol*, 1997. 504 ( Pt 1): p. 17-33.
209. Bezprozvanny, I., J. Watras, and B.E. Ehrlich, Bell-shaped calcium-response curves of Ins(1,4,5)P<sub>3</sub>- and calcium-gated channels from endoplasmic reticulum of cerebellum. *Nature*, 1991. 351(6329): p. 751-4.

## **APPENDICES**

APPENDIX A: COMPLETE MODEL EQUATIONS FOR MODELS OF EC, SMC  
AND EC-SMC INTEGRATED MODEL

## Model equations

### 1. Standard parameter values

$z_K = z_{Na} = 1; z_{Ca} = 2; z_{Cl} = -1; N_{Av} = 6.022 \cdot 10^{23}; R = 8314 \text{ mJ/mol} \cdot \text{K}; F = 96485 \text{ C/mol};$   
 $T = 293.0 \text{ K}; [Ca]_o = 2.0 \text{ mM}; [Na]_o = 140.0 \text{ mM}; [Cl]_o = 129.0 \text{ mM}; [K]_o = 5.0 \text{ mM}.$

### 2. Smooth muscle cells [56]

#### 2.1. Membrane electrophysiology

$$\frac{dV_m}{dt} = \frac{-(I_{VOCC} + I_{Kv} + I_{BKCa} + I_{Kleak} + I_{NSC} + I_{SOC} + I_{ClCa} + I_{PMCA} + I_{NaK} + I_{NCX} + \sum I_{gj}) + I_{stim}}{C_m}$$

$$C_m = 25 \text{ pF}.$$

#### 2.1.1 L-type voltage-operated $Ca^{2+}$ channels

$$I_{VOCC} = A_m P_{VOCC} d_L f_L V_m \frac{(z_{Ca} F)^2 [Ca]_o - [Ca]_i \exp\left(\frac{V_m z_{Ca} F}{RT}\right)}{RT \left(1 - \exp\left(\frac{V_m z_{Ca} F}{RT}\right)\right)}$$

$$\frac{dd_L}{dt} = \frac{\bar{d}_L - d_L}{\tau_{dL}}; \bar{d}_L = \left(1 + \exp\left(-\frac{V_m}{8.3 \text{ mV}}\right)\right)^{-1}; \tau_{dL} = 2.5 \exp\left(-\left(\frac{V_m + 40 \text{ mV}}{30 \text{ mV}}\right)^2\right) + 1.15 \text{ [ms]}$$

$$\frac{df_L}{dt} = \frac{\bar{f}_L - f_L}{\tau_{fL}}; \bar{f}_L = \left(1 + \exp\left(\frac{V_m + 42.0 \text{ mV}}{9.1 \text{ mV}}\right)\right)^{-1}; \tau_{fL} = 65 \exp\left(-\left(\frac{V_m + 35 \text{ mV}}{25 \text{ mV}}\right)^2\right) + 45 \text{ [ms]}$$

$$P_{VOCC} = 1.88 \cdot 10^{-5} \text{ cm/s}; A_m = C_m * (10^{-6} \text{ cm}^2/\text{pF}).$$

#### 2.1.2. Large conductance $Ca^{2+}$ -activated $K^+$ channels

$$I_{BKCa} = A_m N_{BKCa} P_{KCa} i_{KCa}$$

$$P_{KCa} = 0.17 p_f + 0.83 p_s; \frac{dp_f}{dt} = \frac{\bar{p}_o - p_f}{\tau_{pf}}; \frac{dp_s}{dt} = \frac{\bar{p}_o - p_s}{\tau_{ps}}$$

$$\bar{p}_o = \left(1 + \exp\left(-\frac{V_m - V_{1/2KCa}}{18.25 \text{ mV}}\right)\right)^{-1}$$

$$V_{1/2KCa} = -41.7 \text{ mV} * \log_{10}([Ca]_i / (1 \text{ mM})) - 128.2 \text{ mV} - dV_{1/2KCaNO} R_{NO} - dV_{1/2KCaGMP} R_{cGMP}$$

$$R_{NO} = \frac{[NO]}{[NO] + 200 \text{ nM}}; R_{cGMP} = \frac{[cGMP]^2}{[cGMP]^2 + (1.5 \mu\text{M})^2}$$

$$i_{KCa} = P_{BKCa} V_m \frac{F^2 [K]_o - [K]_i \exp\left(\frac{V_m F}{RT}\right)}{RT \left(1 - \exp\left(\frac{V_m F}{RT}\right)\right)}$$

$P_{\text{BKCa}} = 3.9 \cdot 10^{-13} \text{ cm}^3/\text{s}$ ;  $dV_{1/2\text{KCaNO}} = 46.3 \text{ mV}$ ;  $N_{\text{BKCa}} = 6.6 \cdot 10^6 \text{ cm}^{-2}$ ;  $\tau_{pf} = 0.84 \text{ ms}$ ;  $\tau_{ps} = 35.9 \text{ ms}$ ;  $dV_{1/2\text{KCacGMP}} = 76 \text{ mV}$ .

### 2.1.3. Voltage-dependent $K^+$ channels

$$I_{\text{Kv}} = g_{\text{Kv}} p_{\text{K}} (0.45q_1 + 0.55q_2)(V_m - E_{\text{K}})$$

$$\bar{p}_{\text{K}} = \frac{1}{1 + \exp\left(-\frac{V_m + 11.0\text{mV}}{15.0\text{mV}}\right)}; \tau_{p\text{K}} = 61.5 \exp(-0.027V_m) [\text{ms}]; \frac{dp_{\text{K}}}{dt} = \frac{\bar{p}_{\text{K}} - p_{\text{K}}}{\tau_{p\text{K}}}$$

$$\bar{q} = \frac{1}{1 + \exp\left(\frac{V_m + 40.0\text{mV}}{14.0\text{mV}}\right)}; \frac{dq_1}{dt} = \frac{\bar{q} - q_1}{\tau_{q1}}; \frac{dq_2}{dt} = \frac{\bar{q} - q_2}{\tau_{q2}}$$

$g_{\text{Kv}} = 1.35 \text{ nS}$ ;  $\tau_{q1} = 371 \text{ ms}$ ;  $\tau_{q2} = 2884 \text{ ms}$ .

### 2.1.4. Unspecified $K^+$ leak channels

$$I_{\text{Kleak}} = g_{\text{Kleak}}(V_m - E_{\text{K}})$$

$g_{\text{Kleak}} = 0.067 \text{ nS}$ .

### 2.1.5. Nonselective cation channels

$$I_{\text{NSC}} = I_{\text{NaNSC}} + I_{\text{KNSC}} + I_{\text{CaNSC}}$$

$$I_{\text{NaNSC}} = A_m \left( \frac{[\text{DAG}]}{[\text{DAG}] + K_{\text{NSC}}} + d_{\text{NSCmin}} \right) P_{\text{oNSC}} P_{\text{NaNSC}} V_m \frac{F^2}{RT} \frac{[\text{Na}]_o - [\text{Na}]_i \exp\left(\frac{V_m F}{RT}\right)}{1 - \exp\left(\frac{V_m F}{RT}\right)}$$

$$I_{\text{KNSC}} = A_m \left( \frac{[\text{DAG}]}{[\text{DAG}] + K_{\text{NSC}}} + d_{\text{NSCmin}} \right) P_{\text{oNSC}} P_{\text{KNSC}} V_m \frac{F^2}{RT} \frac{[\text{K}]_o - [\text{K}]_i \exp\left(\frac{V_m F}{RT}\right)}{1 - \exp\left(\frac{V_m F}{RT}\right)}$$

$$I_{\text{CaNSC}} = A_m d_{\text{NSCmin}} P_{\text{oNSC}} P_{\text{CaNSC}} V_m \frac{(z_{\text{Ca}} F)^2}{RT} \frac{[\text{Ca}]_o - [\text{Ca}]_i \exp\left(\frac{z_{\text{Ca}} V_m F}{RT}\right)}{1 - \exp\left(\frac{z_{\text{Ca}} V_m F}{RT}\right)}$$

$$P_{\text{oNSC}} = 0.43 + \frac{0.57}{1 + \exp\left(-\frac{V_m - 47.12\text{mV}}{24.24\text{mV}}\right)}$$

$K_{\text{NSC}} = 3 \mu\text{M}$ ;  $P_{\text{NaNSC}} = 5.11 \cdot 10^{-7} \text{ cm}^2/\text{s}$ ;  $P_{\text{KNSC}} = 1.06 \cdot P_{\text{NaNSC}}$ ;  $P_{\text{CaNSC}} = 4.54 \cdot P_{\text{NaNSC}}$ ;  $d_{\text{NSCmin}} = 0.0244$ .

### 2.1.6. Store-operated nonselective cation channels

$$I_{\text{SOC}} = I_{\text{SOCCa}} + I_{\text{SOCNa}}$$

$$I_{\text{SOCCa}} = g_{\text{SOCCa}} P_{\text{SOC}} (V_m - E_{\text{Ca}}); I_{\text{SOCNa}} = g_{\text{SOCNa}} P_{\text{SOC}} (V_m - E_{\text{Na}})$$

$$P_{\text{SOC}} = \left(1 + \frac{[\text{Ca}]_u}{100\text{nM}}\right)^{-1}$$

$$g_{\text{SOC}_{\text{Ca}}} = 0.0083 \text{ nM}; g_{\text{SOC}_{\text{Na}}} = 0.0575 \text{ nM}.$$

### 2.1.7. Calcium-activated chloride channels

$$I_{\text{ClCa}} = C_m g_{\text{ClCa}} P_{\text{Cl}} (V_m - E_{\text{Cl}})$$

$$P_{\text{Cl}} = 0.0132 \frac{([\text{Ca}]_i)^{n_{\text{ClCa}}}}{([\text{Ca}]_i)^{n_{\text{ClCa}}} + (K_{\text{ClCa}})^{n_{\text{ClCa}}}} + \alpha_{\text{Cl}} \frac{([\text{Ca}]_i)^{n_{\text{ClCa}}}}{([\text{Ca}]_i)^{n_{\text{ClCa}}} + (K_{\text{ClCa,cGMP}})^{n_{\text{ClCa}}}}$$

$$\alpha_{\text{Cl}} = \frac{([\text{cGMP}])^{n_{\text{ClcGMP}}}}{([\text{cGMP}])^{n_{\text{ClcGMP}}} + (K_{\text{ClcGMP}})^{n_{\text{ClcGMP}}}} \quad K_{\text{ClCa,cGMP}} = (1 - 0.9\alpha_{\text{Cl}}) \cdot 400\text{nM}$$

$$g_{\text{ClCa}} = 0.23 \text{ nS/pF}; n_{\text{ClCa}} = 2; K_{\text{ClCa}} = 365 \text{ nM}; n_{\text{ClcGMP}} = 3.3; K_{\text{ClcGMP}} = 6.4 \mu\text{M}.$$

### 2.1.8. Plasma membrane $\text{Ca}^{2+}$ pump

$$I_{\text{PMCA}} = \bar{I}_{\text{PMCA}} \frac{[\text{Ca}]_i}{[\text{Ca}]_i + K_{m,\text{PMCA}}}$$

$$\bar{I}_{\text{PMCA}} = 5.37 \text{ pA}; K_{m,\text{PMCA}} = 170 \text{ nM}.$$

### 2.1.9. Plasma membrane $\text{Na}^+$ - $\text{Ca}^{2+}$ exchange

$$I_{\text{NCX}} = g_{\text{NCX}} R_{\text{NCX,cGMP}} \frac{[\text{Na}]_i^3 [\text{Ca}]_o \Phi_F - [\text{Na}]_o^3 [\text{Ca}]_i \Phi_R}{(1\text{mM})^4 + d_{\text{NCX}} ([\text{Na}]_o^3 [\text{Ca}]_i + [\text{Na}]_i^3 [\text{Ca}]_o)}$$

$$R_{\text{NCX,cGMP}} = 1 + 0.55 \frac{[\text{cGMP}]}{[\text{cGMP}] + 45\mu\text{M}}$$

$$\Phi_F = \exp\left(\frac{\gamma V_m F}{RT}\right); \Phi_R = \exp\left(\frac{(\gamma-1)V_m F}{RT}\right); \gamma = 0.45; d_{\text{NCX}} = 0.0003; g_{\text{NCX}} = 4.87 \cdot 10^{-4} \text{ pA}$$

### 2.1.10. Sodium-potassium pump

$$I_{\text{NaK}} = C_m \bar{I}_{\text{NaK}} Q \frac{([\text{K}]_o)^{n_{\text{HKo}}}}{([\text{K}]_o)^{n_{\text{HKo}}} + (K_{\text{dKo}})^{n_{\text{HKo}}}} \frac{([\text{Na}]_i)^{n_{\text{HNai}}}}{([\text{Na}]_i)^{n_{\text{HNai}}} + (K_{\text{dNai}})^{n_{\text{HNai}}}} \frac{V_m + 150\text{mV}}{V_m + 200\text{mV}}$$

$$Q = Q_{10}^{\frac{T-309.15\text{K}}{10}}; Q_{10} = 1.87$$

$$\bar{I}_{\text{NaK}} = 2.31 \text{ pA/pF}; K_{\text{dKo}} = 1.6 \text{ mM}; K_{\text{dNai}} = 22 \text{ mM}; n_{\text{HKo}} = 1.1; n_{\text{HNai}} = 1.7.$$

### 2.1.11. Sodium-potassium-chloride cotransport

$$I_{\text{NaKCl}}^{\text{Cl}} = -R_{\text{NaKCl,cGMP}} z_{\text{Cl}} A_m L_{\text{NaKCl}} \text{RFT} \log_e \left( \frac{[\text{Na}]_o [\text{K}]_o ([\text{Cl}]_o)^2}{[\text{Na}]_i [\text{K}]_i ([\text{Cl}]_i)^2} \right)$$

$$R_{\text{NaKCl,cGMP}} = 1 + 3.5 \frac{[\text{cGMP}]}{[\text{cGMP}] + 6.4 \mu\text{M}}$$

$$I_{\text{NaKCl}}^{\text{Na}} = I_{\text{NaKCl}}^{\text{K}} = -0.5 I_{\text{NaKCl}}^{\text{Cl}}$$

$$L_{\text{NaKCl}} = 1.79 \cdot 10^{-11} \text{ (mmol)}^2 / (\text{J} \cdot \text{s} \cdot \text{cm}^2).$$

*Reversal potentials*

$$E_A = \frac{RT}{z_A F} \ln \left( \frac{[A]_o}{[A]_i} \right), \text{ where A denotes K, Na, Ca or Cl.}$$

## 2.2. Sarcoplasmic reticulum

$$I_{\text{SERCA}} = \bar{I}_{\text{SERCA}} \frac{[\text{Ca}]_i}{[\text{Ca}]_i + K_{\text{m,up}}}$$

$$I_{\text{tr}} = ([\text{Ca}]_u - [\text{Ca}]_r) z_{\text{Ca}} F \cdot \text{vol}_u / \tau_{\text{tr}}$$

$$I_{\text{rel}} = (R_{10}^2 + R_{\text{leak}}) ([\text{Ca}]_r - [\text{Ca}]_i) z_{\text{Ca}} F \cdot \text{vol}_r / \tau_{\text{rel}}$$

$$\frac{d[\text{Ca}]_u}{dt} = \frac{I_{\text{SERCA}} - I_{\text{tr}} - I_{\text{IP3}}}{z_{\text{Ca}} F \text{vol}_u}$$

$$\frac{d[\text{Ca}]_r}{dt} = \frac{I_{\text{tr}} - I_{\text{rel}}}{z_{\text{Ca}} F \text{vol}_r} \left( 1 + \frac{[\overline{\text{CSQN}}] K_{\text{CSQN}}}{(K_{\text{CSQN}} + [\text{Ca}]_r)^2} \right)^{-1}$$

$$\tau_{\text{tr}} = 1000 \text{ms}; \tau_{\text{rel}} = 0.033 \text{ms}$$

$$K_{\text{m,up}} = 1 \mu\text{M}; \bar{I}_{\text{SERCA}} = 6.68 \text{ pA}; R_{\text{leak}} = 1.07 \cdot 10^{-5}; K_{\text{CSQN}} = 0.8 \text{ mM}; [\overline{\text{CSQN}}] = 15 \text{ mM};$$

$\text{vol}_u = 0.07 \text{ pL}; \text{vol}_r = 0.007 \text{ pL}.$

### 2.2.1. Ryanodine receptor

$$R_{00} = 1 - R_{01} - R_{10} - R_{11}$$

$$\frac{dR_{10}}{dt} = K_{r1} [\text{Ca}]_i^2 R_{00} - (K_{-r1} + K_{r2} [\text{Ca}]_i) R_{10} + K_{-r2} R_{11}$$

$$\frac{dR_{11}}{dt} = K_{r2} [\text{Ca}]_i R_{10} - (K_{-r1} + K_{-r2}) R_{11} + K_{r1} [\text{Ca}]_i^2 R_{01}$$

$$\frac{dR_{01}}{dt} = K_{r2} [\text{Ca}]_i R_{00} + K_{-r1} R_{11} - (K_{-r2} + K_{r1} [\text{Ca}]_i^2) R_{01}$$

$$K_{r1} = 2500 \text{ mM}^{-2} \text{ms}^{-1}; K_{r2} = 1.05 \text{ mM}^{-1} \text{ms}^{-1}; K_{-r1} = 0.0076 \text{ ms}^{-1}; K_{-r2} = 0.084 \text{ ms}^{-1}$$

### 2.2.2. IP<sub>3</sub> receptor

$$I_{\text{IP3}} = \bar{I}_{\text{IP3}} z_{\text{Ca}} \text{vol}_{\text{Ca}} F \left( \frac{[\text{IP}_3]}{[\text{IP}_3] + K_{\text{IP3}}} \cdot \frac{[\text{Ca}]_i}{[\text{Ca}]_i + K_{\text{act,IP3}}} h_{\text{IP3}} \right)^3 ([\text{Ca}]_u - [\text{Ca}]_i)$$



$$\frac{dh_{IP_3}}{dt} = k_{on,IP_3} (K_{inh,IP_3} - ([Ca]_i + K_{inh,IP_3})h_{IP_3})$$

$$\bar{I}_{IP_3} = 2880 \cdot 10^{-6} \text{ ms}^{-1}; K_{act,IP_3} = 170 \text{ nM}; K_{inh,IP_3} = 100 \text{ nM}; K_{IP_3} = 120 \text{ nM}; k_{on,IP_3} = 1.4 \text{ mM}^{-1} \text{ ms}^{-1}$$

### 2.3. $\alpha_1$ -adrenoceptor activation and $IP_3$ and DAG formation

$$\frac{d[R_G^S]}{dt} = k_{r,G} \xi_G [R_{T,G}] - \left( k_{r,G} + \frac{k_{p,G}[NE]}{K_{1,G} + [NE]} \right) \cdot [R_G^S] - k_{r,G} [R_{P,G}^S]$$

$$\frac{d[R_{P,G}^S]}{dt} = [NE] \left( \frac{k_{p,G}[R_G^S]}{K_{1,G} + [NE]} - \frac{k_{e,G}[R_{P,G}^S]}{K_{2,G} + [NE]} \right)$$

$$\rho_{r,G} = \frac{[NE][R_G^S]}{\xi_G [R_{T,G}] (K_{1,G} + [NE])}$$

$$\frac{d[G]}{dt} = k_{a,G} (\delta_G + \rho_{r,G}) ([G_{T,G}] - [G]) - k_{d,G} [G]$$

$$r_{h,G} = \alpha_G \frac{[Ca]_i}{[Ca]_i + K_{c,G}} [G]$$

$$\frac{d[IP_3]}{dt} = \frac{r_{h,G}}{\gamma_G} [PIP_2] - k_{deg,G} [IP_3] + \sum J_{IP_3}$$

$$\frac{d[DAG]}{dt} = \frac{r_{h,G}}{\gamma_G} [PIP_2] - k_{deg,G} [DAG]$$

$$\frac{d[PIP_2]}{dt} = -(r_{h,G} + r_{r,G}) [PIP_2] - r_{r,G} \gamma_G [IP_3] + r_{r,G} [PIP_{2,T}]$$

$$[R_{T,G}] = 2 \cdot 10^4; K_{1,G} = k_1^- / k_1^+ = 0.01 \text{ mM}; K_{2,G} = k_2^- / k_2^+ = 0.2 \text{ mM}; k_{r,G} = 1.75 \cdot 10^{-7} \text{ ms}^{-1}$$

$$k_{e,G} = 6 \cdot 10^{-6} \text{ ms}^{-1}; \xi_G = 0.85; [G_{T,G}] = 1 \cdot 10^5; k_{deg,G} = 1.25 \cdot 10^{-3} \text{ ms}^{-1}; k_{a,G} = 0.17 \cdot 10^{-3} \text{ ms}^{-1}$$

$$k_{d,G} = 1.5 \cdot 10^{-3} \text{ ms}^{-1}; [PIP_{2,T}] = 5 \cdot 10^7; r_{r,G} = 0.015 \cdot 10^{-3} \text{ ms}^{-1}; K_{c,G} = 0.4 \cdot 10^{-3} \text{ mM}$$

$$\alpha_G = 2.781 \cdot 10^{-8} \text{ ms}^{-1}; \gamma_G = 10^{-15} N_{AV} \text{ vol}_i; k_{p,G} = 0.$$

### 2.4. sGC activation and cGMP formation

$$\bar{V}_{cGMP} = V_{cGMP,max} \frac{B5_{sGC} [NO] + [NO]^2}{A0_{sGC} + A1_{sGC} [NO] + [NO]^2}$$

$$\tau_{sGC} = \begin{cases} \tau_{sGC}^a & \text{if } (\bar{V}_{cGMP} - V_{cGMP}) \geq 0 \\ \tau_{sGC}^d & \text{otherwise} \end{cases}$$

$$\frac{dV_{cGMP}}{dt} = \frac{\bar{V}_{cGMP} - V_{cGMP}}{\tau_{sGC}}$$

$$\frac{d[\text{cGMP}]}{dt} = V_{\text{cGMP}} - k_{\text{pde,cGMP}} \frac{[\text{cGMP}]^2}{[\text{cGMP}] + K_{\text{m,pde}}}$$

$$k_{1,\text{sGC}} = 2 \cdot 10^3 \text{ mM}^{-1} \text{ ms}^{-1}; k_{-1,\text{sGC}} = 15 \cdot 10^{-3} \text{ ms}^{-1}; k_{2,\text{sGC}} = 0.64 \cdot 10^{-5} \text{ ms}^{-1}$$

$$k_{-2,\text{sGC}} = 0.1 \cdot 10^{-6} \text{ ms}^{-1}; k_{3,\text{sGC}} = 4.2 \text{ mM}^{-1} \text{ ms}^{-1}; k_{\text{D,sGC}} = 0.4 \cdot 10^{-3} \text{ ms}^{-1}; k_{\text{D}\tau,\text{sGC}} = 0.1 \cdot 10^{-3} \text{ ms}^{-1}$$

$$B5_{\text{sGC}} = k_{2,\text{sGC}} / k_{3,\text{sGC}}$$

$$A0_{\text{sGC}} = ((k_{-1,\text{sGC}} + k_{2,\text{sGC}})k_{\text{D,sGC}} + k_{-1,\text{sGC}}k_{-2,\text{sGC}}) / (k_{1,\text{sGC}}k_{3,\text{sGC}})$$

$$A1_{\text{sGC}} = ((k_{1,\text{sGC}} + k_{3,\text{sGC}})k_{\text{D,sGC}} + (k_{2,\text{sGC}} + k_{-2,\text{sGC}})k_{1,\text{sGC}}) / (k_{1,\text{sGC}}k_{3,\text{sGC}})$$

$$k_{\text{pde,cGMP}} = 0.0695 \cdot 10^{-3} \text{ ms}^{-1}; \tau_{\text{sGC}}^{\text{a}} = 0.23 \text{ s}; \tau_{\text{sGC}}^{\text{d}} = 10 \text{ s}; V_{\text{cGMP,max}} = 1.26 \cdot 10^{-7} \text{ mM/ms};$$

$$K_{\text{m,pde}} = 10^{-3} \text{ mM}$$

## 2.5. Ionic balances

$$I_{\text{Catotm}} = I_{\text{SOCCa}} + I_{\text{VOCC}} - 2I_{\text{NCX}} + I_{\text{PMCA}} + I_{\text{CaNSC}}$$

$$\frac{d[\text{Ca}]_i}{dt} = -\frac{I_{\text{Catotm}} + I_{\text{SERCA}} - I_{\text{rel}} - I_{\text{IP3}} + \sum I_{\text{gj,Ca}}}{z_{\text{Ca}} F \cdot \text{vol}_{\text{Ca}}} \left( 1 + \frac{[\bar{\text{S}}_{\text{CM}}]K_{\text{d}}}{(K_{\text{d}} + [\text{Ca}]_i)^2} + \frac{[\bar{\text{B}}_{\text{F}}]K_{\text{dB}}}{(K_{\text{dB}} + [\text{Ca}]_i)^2} \right)^{-1}$$

$$I_{\text{Natotm}} = I_{\text{NaKCl}}^{\text{Na}} + I_{\text{SOCNa}} + 3I_{\text{NaK}} + 3I_{\text{NCX}} + I_{\text{NaNSC}}; \frac{d[\text{Na}]_i}{dt} = -\frac{I_{\text{Natotm}} + \sum I_{\text{gj,Na}}}{F \cdot \text{vol}_i}$$

$$I_{\text{Ktotm}} = I_{\text{NaKCl}}^{\text{K}} + I_{\text{Kv}} + I_{\text{BKCa}} + I_{\text{KNSC}} + I_{\text{Kleak}} - 2I_{\text{NaK}}; \frac{d[\text{K}]_i}{dt} = -\frac{I_{\text{Ktotm}} + \sum I_{\text{gj,K}}}{F \cdot \text{vol}_i}$$

$$I_{\text{Cltotm}} = I_{\text{NaKCl}}^{\text{Cl}} + I_{\text{ClCa}}; \frac{d[\text{Cl}]_i}{dt} = -\frac{I_{\text{Cltotm}} + \sum I_{\text{gj,Cl}}}{z_{\text{Cl}} F \cdot \text{vol}_i}$$

$$[\bar{\text{S}}_{\text{CM}}] = 0.1 \text{ mM}; [\bar{\text{B}}_{\text{F}}] = 0.1 \text{ mM}; K_{\text{d}} = 260 \text{ nM}; K_{\text{dB}} = 530 \text{ nM}; \text{vol}_i = 1.0 \text{ pL}; \text{vol}_{\text{Ca}} = 0.7 \text{ pL}.$$

## 2.6. Initial conditions

$$V_{\text{m}} = -52.7 \text{ mV}; [\text{Ca}]_i = 96 \text{ nM}; [\text{Ca}]_{\text{u}} = 0.77 \text{ mM}; [\text{Ca}]_{\text{r}} = 0.73 \text{ mM}; [\text{Na}]_i = 9.4 \text{ mM}; [\text{K}]_i$$

$$= 121 \text{ mM}; [\text{Cl}]_i = 42.0 \text{ mM}; [\text{IP}_3] = [\text{DAG}] = [\text{cGMP}] = 0; V_{\text{cGMP}} = 0$$

$$I_{\text{VOCC}}: d_{\text{L}} = 1/(1+\exp(-V_{\text{m}}/8.3\text{mV})); f_{\text{L}} = 1/(1+\exp((V_{\text{m}}+42.0\text{mV})/9.1\text{mV}))$$

$$I_{\text{BKCa}}: p_{\text{f}} = p_{\text{s}} = 1/(1+\exp(-(V_{\text{m}}-V_{1/2\text{KCa}})/18.25\text{mV}))$$

$$I_{\text{Kv}}: p_{\text{K}} = 1/(1+\exp(-(V_{\text{m}}+11)/15)); q_1 = q_2 = 1.0/(1+\exp((V_{\text{m}}+40)/14))$$

$$\text{RyR}: R_{01} = 0.0012; R_{10} = 0.003; R_{11} = 3.62 \cdot 10^{-6}$$

$$\text{IP}_3\text{R}: h_{\text{IP}_3} = K_{\text{inh,IP}_3} / ([\text{Ca}]_i + K_{\text{inh,IP}_3})$$

$$\alpha 1\text{-adrenoceptor}: [\text{R}_{\text{G}}^{\text{S}}] = [\text{R}_{\text{T,G}}] \cdot \xi_{\text{G}}; [\text{R}_{\text{P,G}}^{\text{S}}] = 0; [\text{PIP}_2] = [\text{PIP}_{2,\text{T}}] - (1 + k_{\text{deg,G}} / r_{\text{r,G}}) \gamma_{\text{G}} [\text{IP}_3];$$

$$r_{\text{h,G}} = k_{\text{deg,G}} \cdot \gamma_{\text{G}} [\text{IP}_3] / [\text{PIP}_2]; G = r_{\text{h,G}} (K_{\text{c,G}} + [\text{Ca}]_i) / (\alpha_{\text{G}} [\text{Ca}]_i); \delta_{\text{G}} = k_{\text{d,G}} \cdot G / (k_{\text{a,G}} ([\text{G}_{\text{T,G}}] - G))$$

### 3. Endothelial cells [78]

#### 3.1 Membrane electrophysiology

$$\frac{dV_m}{dt} = -\frac{1}{C_m} (I_{\text{SOC}} + I_{\text{NSC}} + I_{\text{VRAC}} + I_{\text{CaCC}} + I_{\text{Kir}} + I_{\text{IKCa}} + I_{\text{SKCa}} + I_{\text{NaK}} + I_{\text{NCX}} + I_{\text{PMCA}} + \sum I_{\text{gj}} - I_{\text{stim}})$$

$$C_m = 14 \text{ pF.}$$

##### 3.1.1 Inward rectifier potassium channel current ( $I_{\text{Kir}}$ )

$$I_{\text{Kir}} = \frac{G_{\text{Kir,max}} \cdot (V_m - E_K)}{1 + e^{\frac{\Delta V - \Delta V_{\text{Kir,h}}}{v_{\text{Kir}}}}}$$

$$G_{\text{Kir,max}} = G_{\text{Kir}} \cdot ([K^+]_o)^{n_{\text{Kir}}}$$

$$\Delta V = V_m - E_K$$

$$\Delta V_{\text{Kir,h}} = 39.42 \text{ mV}; v_{\text{Kir}} = 7.084 \text{ mV}; G_{\text{Kir}} = 0.1423 \text{ nS/mM}^{0.5}; n_{\text{Kir}} = 0.5.$$

##### 3.1.2 Calcium-activated potassium channel currents ( $I_{\text{SKCa}}, I_{\text{IKCa}}$ )

$$I_X = G_X \cdot P_{O,X} \cdot (V_m - E_K)$$

$$P_{O,X} = \frac{[Ca^{2+}]_i^{n_X}}{[Ca^{2+}]_i^{n_X} + K_{X,Cai}^{n_X}}$$

where X denotes SK<sub>Ca</sub> or IK<sub>Ca</sub>.

$$G_{\text{SKCa}} = 0.62 \text{ nS}; G_{\text{IKCa}} = 1.72 \text{ nS}; n_{\text{SKCa}} = 5 \text{ } n_{\text{IKCa}} = 4; K_{\text{SKCa,Cai}} = 237 \text{ nM}; K_{\text{IKCa,Cai}} = 740 \text{ nM.}$$

##### 3.1.3 Calcium-activated chloride channel current ( $I_{\text{CaCC}}$ )

$$I_{\text{CaCC}} = G_{\text{CaCC}} \cdot P_{O,\text{CaCC}} \cdot \frac{1}{1 + \left( \frac{K_{\text{CaCC,Cai}}}{[Ca^{2+}]_i} \right)^{n_{\text{CaCC}}}} \cdot (V_m - E_{\text{Cl}})$$

$$\frac{dP_{O,\text{CaCC}}}{dt} = \frac{P_{O,\text{CaCC,SS}} - P_{O,\text{CaCC}}}{\tau_{\text{CaCC}}}$$

$$P_{O,\text{CaCC,SS}} = \frac{1}{1 + e^{-\frac{(V_m - V_{\text{CaCC,h}})}{v_{\text{CaCC}}}}}$$

$$\tau_{\text{CaCC}} = 386.2 \cdot e^{-\left( \frac{V_m - 19.9 \text{ mV}}{88.9 \text{ mV}} \right)^2} \quad [\text{ms}]$$

$$V_{\text{CaCC,h}} = 662 \text{ mV}; v_{\text{CaCC}} = 132 \text{ mV}; G_{\text{CaCC}} = 37.38 \text{ nS}; n_{\text{CaCC}} = 1.89; K_{\text{CaCC,Cai}} = 287 \text{ nM.}$$

##### 3.1.4 Volume-regulated anion channel current ( $I_{\text{VRAC}}$ )

$$I_{\text{VRAC}} = G_{\text{VRAC}} \cdot (V_m - E_{\text{Cl}})$$

$$G_{\text{VRAC}} = 0.381 \text{ nS.}$$

### 3.1.5 Store-operated cation channel current ( $I_{\text{SOC}}$ )

$$I_{\text{SOC,Na}} = P_{\text{SOC,Na}} \cdot A_m \cdot \frac{F^2}{RT} \cdot V_m \cdot \frac{[\text{Na}^+]_i - [\text{Na}^+]_o \cdot e^{-\frac{V_m F}{RT}}}{1 - e^{-\frac{V_m F}{RT}}}$$

$$I_{\text{SOC,Ca}} = P_{\text{SOC,Ca}} \cdot A_m \cdot \frac{z_{\text{Ca}}^2 F^2}{RT} \cdot V_m \cdot \frac{[\text{Ca}^{2+}]_i - [\text{Ca}^{2+}]_o \cdot e^{-\frac{z_{\text{Ca}} V_m F}{RT}}}{1 - e^{-\frac{z_{\text{Ca}} V_m F}{RT}}}$$

$$I_{\text{SOC}} = P_{\text{O,SOC}} \cdot (I_{\text{SOC,Na}} + I_{\text{SOC,Ca}})$$

$$P_{\text{SOC,Na}} = \frac{P_{\text{SOCNa,max}}}{1 + \left( \frac{[\text{Ca}^{2+}]_o}{K_{\text{SOC,Cao}}} \right)^{n_{\text{SOC,Na}}}}$$

$$P_{\text{O,SOC}} = \frac{0.25}{1 + \left( \frac{[\text{Ca}^{2+}]_{\text{IS}}}{K_{\text{SOC,CaIS}}} \right)^{n_{\text{SOC}}}} + 0.083$$

$$P_{\text{SOCNa,max}} = 3.95 \times 10^{-7} \text{ cm/s}; P_{\text{SOC,Ca}} = 1.15 \times 10^{-7} \text{ cm/s}; n_{\text{SOC,Na}} = 0.622; n_{\text{SOC}} = 3.2;$$

$$K_{\text{SOC,CaIS}} = 0.47 \text{ mM}; K_{\text{SOC,Cao}} = 2.0 \times 10^{-4} \text{ mM}; A_m = 14 \times 10^{-6} \text{ cm}^2.$$

### 3.1.6 Nonselective cation channel current ( $I_{\text{NSC}}$ )

$$I_{\text{NSC,Na}} = P_{\text{NSC,Na}} \cdot A_m \cdot \frac{F^2}{RT} \cdot V_m \cdot \frac{[\text{Na}^+]_i - [\text{Na}^+]_o \cdot e^{-\frac{V_m F}{RT}}}{1 - e^{-\frac{V_m F}{RT}}}$$

$$I_{\text{NSC,K}} = P_{\text{NSC,K}} \cdot A_m \cdot \frac{F^2}{RT} \cdot V_m \cdot \frac{[\text{K}^+]_i - [\text{K}^+]_o \cdot e^{-\frac{V_m F}{RT}}}{1 - e^{-\frac{V_m F}{RT}}}$$

$$I_{\text{NSC,Ca}} = P_{\text{NSC,Ca}} \cdot A_m \cdot \frac{z_{\text{Ca}}^2 F^2}{RT} \cdot V_m \cdot \frac{[\text{Ca}^{2+}]_i - [\text{Ca}^{2+}]_o \cdot e^{-\frac{z_{\text{Ca}} V_m F}{RT}}}{1 - e^{-\frac{z_{\text{Ca}} V_m F}{RT}}}$$

$$I_{\text{NSC}} = I_{\text{NSC,Na}} + I_{\text{NSC,K}} + I_{\text{NSC,Ca}}$$

$$P_{\text{NSC,Na}} = \frac{P_{\text{NSC,Namax}}}{1 + \left( \frac{[\text{Ca}^{2+}]_o}{K_{\text{NSC,Cao}}} \right)^{n_{\text{NSC}}}}$$

$$P_{\text{NSC,Namax}} = 5.34 \times 10^{-8} \text{ cm/s}; P_{\text{NSC,K}} = 0.49 \times 10^{-7} \text{ cm/s}; P_{\text{NSC,Ca}} = 2.4 \times 10^{-8} \text{ cm/s.}$$

3.1.7 *Sodium-calcium exchanger current* ( $I_{NCX}$ )

$$I_{NCX} = \frac{1}{1 + \left( \frac{K_{NCX,Cai}}{[Ca^{2+}]_i} \right)^{n_{NCX,h}}} \cdot g_{NCX} \frac{([Na^+]_i^{n_{NCX}} \cdot [Ca^{2+}]_o \cdot \varphi_F - [Na^+]_o^{n_{NCX}} \cdot [Ca^{2+}]_i \cdot \varphi_R)}{(1\text{mM})^4 + d_{NCX} ([Na^+]_o^{n_{NCX}} \cdot [Ca^{2+}]_i + [Na^+]_i^{n_{NCX}} \cdot [Ca^{2+}]_o)}$$

$$\varphi_F = e^{\gamma V_m (n_{NCX}-2) z_{NCX} F/RT}$$

$$\varphi_R = e^{(\gamma-1) V_m (n_{NCX}-2) z_{NCX} F/RT}$$

$g_{NCX} = 1.99 \text{ pA}$ ;  $n_{NCX,h} = 1.50$ ;  $n_{NCX} = 3$ ;  $\gamma = 0.4834$ ;  $d_{NCX} = 3.04 \times 10^{-4}$ ;  $z_{NCX} = 1$ ;  
 $K_{NCX,Cai} = 0.502 \text{ mM}$ .

3.1.8 *Sodium-potassium ( $Na^+/K^+$ ) ATPase current* ( $I_{NaK}$ )

$$I_{NaK} = \bar{I}_{NaK} \frac{[K^+]_o}{[K^+]_o + K_{NaK,Ko}} \cdot \frac{[Na^+]_i^{1.5}}{[Na^+]_i^{1.5} + K_{NaK,Nai}^{1.5}} \cdot \frac{V_m + 135.1\text{mV}}{V_m + 300\text{mV}}$$

$$\bar{I}_{NaK} = 20.18 \text{ pA}; K_{NaK,Ko} = 1.32 \text{ mM}; K_{NaK,Nai} = 14.52 \text{ mM}.$$

3.1.9 *Sodium-potassium-chloride ( $Na^+/K^+/2Cl^-$ ) cotransport flux* ( $I_{NaKCl}$ )

$$I_{NaKCl\_Cl} = -L_{NaKCl} \cdot A_m \cdot RTF \cdot z_{Cl} \cdot \ln \left[ \frac{[Na^+]_o}{[Na^+]_i} \cdot \frac{[K^+]_o}{[K^+]_i} \cdot \left( \frac{[Cl^-]_o}{[Cl^-]_i} \right)^2 \right]$$

$$I_{NaKCl\_K} = I_{NaKCl\_Na} = -0.5 \cdot I_{NaKCl\_Cl}$$

$$L_{NaKCl} = 3.2 \times 10^{-9} (\text{mmol})^2 \text{ J}^{-1} \text{ s}^{-1} \text{ cm}^{-2}.$$

### 3.1.10 Plasma membrane calcium ATPase current ( $I_{PMCA}$ )

$$I_{PMCA} = \bar{I}_{PMCA} \frac{[Ca^{2+}]_i^{n_{PMCA}}}{[Ca^{2+}]_i^{n_{PMCA}} + K_{PMCA,Cai}^{n_{PMCA}}}$$

$$\bar{I}_{PMCA} = 2.67 \text{ pA}; K_{PMCA,Cai} = 0.260 \times 10^{-3} \text{ mM}; n_{PMCA} = 1.4.$$

$$E_A = \frac{RT}{z_A F} \ln \left( \frac{[A]_o}{[A]_i} \right) \text{ where A denotes } K^+, Na^+, Ca^{2+} \text{ or } Cl^-.$$

### 3.1.11 Nernst potential ( $E$ )

## 3.2 Fluid compartment model

### 3.2.1 $IP_3$ receptor current ( $I_{IP3R}$ )

$$I_{IP3R} = \bar{I}_{IP3R} \cdot \frac{[IP_3]^{3.8}}{[IP_3]^{3.8} + K_{m,IP3}^{3.8}} \cdot P_{i,IP3R} \cdot ([Ca^{2+}]_{IS} - [Ca^{2+}]_i)$$

$$P_{i,IP3R} = \frac{K_{i,Cai}^{3.8}}{[Ca^{2+}]_i^{3.8} + K_{i,Cai}^{3.8}}$$

$$\bar{I}_{IP3R} = 4.67 \times 10^6 \text{ pA/mM}; K_{m,IP3} = 1.6 \times 10^{-3} \text{ mM}; K_{i,Cai} = 1.0 \times 10^{-3} \text{ mM}.$$

3.2.2 *Sarco/endoplasmic reticulum calcium ATPase ( $I_{SERCA}$ ) and ER leak ( $I_{leak}$ ) currents*

$$I_{SERCA,IS} = \bar{I}_{SERCA,IS} \left( \frac{[Ca^{2+}]_i}{[Ca^{2+}]_i + K_{SERCA,IS}} \right)^2$$

$$I_{leak,IS} = k_{leak,IS} ([Ca^{2+}]_{IS} - [Ca^{2+}]_i)^2$$

$$\bar{I}_{SERCA,IS} = 0.88 \text{ pA}; K_{SERCA,IS} = 0.15 \times 10^{-3} \text{ mM}; k_{leak,IS} = 0.0176 \text{ pA/(mM)}^2.$$

### 3.3 Intracellular ionic and material balances

$$I_{Catotm} = I_{SOC,Ca} - 2I_{NCX} + I_{PMCA} + I_{NSC,Ca}$$

$$\frac{d[Ca^{2+}]_i}{dt} = - \frac{I_{Catotm} + I_{SERCA,IS} - I_{leak,IS} - I_{IP3R} + \sum I_{gi,Ca}}{z_{Ca} \cdot F \cdot vol_{Ca}} - \frac{d[Ca^{2+}]_B}{dt}$$

$$\frac{d[Ca^{2+}]_B}{dt} = kB_{on} \cdot [Ca^{2+}]_i \cdot (B_T - [Ca^{2+}]_B) - kB_{off} \cdot [Ca^{2+}]_B$$

$$\frac{d[Ca^{2+}]_{IS}}{dt} = - \frac{I_{IP3R} - I_{SERCA,IS} + I_{leak,IS}}{z_{Ca} \cdot F \cdot vol_{IS}} \left[ 1 + \frac{\overline{CSQN} \cdot K_{CSQN}}{(K_{CSQN} + [Ca^{2+}]_{IS})^2} \right]^{-1}$$

$$\frac{d[Na^+]_i}{dt} = - \frac{I_{SOC,Na} + 3I_{NCX} + I_{NSC,Na} + 3I_{NaK} + I_{NaKCl,Na} + \sum I_{gi,Na}}{z_{Na} \cdot F \cdot vol_i}$$

$$\frac{d[K^+]_i}{dt} = - \frac{I_{SK,Ca} + I_{IK,Ca} + I_{Kir} + I_{NSC,K} - 2I_{NaK} + I_{NaKCl,K} + \sum I_{gi,K}}{z_K \cdot F \cdot vol_i}$$

$$\frac{d[Cl^-]_i}{dt} = - \frac{I_{NaKCl,Cl} + I_{VRAC} + I_{CaCC} + \sum I_{gi,Cl}}{z_{Cl} \cdot F \cdot vol_i}$$

$$\frac{d[IP_3]}{dt} = Q_{GIP3} - k_{DIP3} \cdot [IP_3] + \sum J_{IP3}$$

$$\frac{dQ_{GIP3}}{dt} = \frac{Q_{GIP3,SS} - Q_{GIP3}}{\tau_{IP3}}$$

$$kB_{on} = 100 \text{ (mM)}^{-1} \cdot (\text{ms})^{-1}; kB_{off} = 0.300 \text{ (ms)}^{-1}; B_T = 0.120 \text{ mM}; \overline{CSQN} = 15 \text{ mM}; K_{CSQN} = 0.8 \text{ mM}; Q_{GIP3,SS} = 5.5 \times 10^{-8} \text{ mM/ms}; k_{DIP3} = 2.0 \times 10^{-3} \text{ (ms)}^{-1}; \tau_{IP3} = 5 \text{ s}; vol_i = 1.173 \text{ pL}; vol_{Ca} = 0.912 \text{ pL}; vol_{IS} = 0.335 \text{ pL}.$$

### 3.2. Initial conditions

$$V_m = -49.8 \text{ mV}; [Ca^{2+}]_i = 131 \text{ nM}; [Ca^{2+}]_{IS} = 3.3 \text{ mM}; [Na^+]_i = 18.7 \text{ mM}; [K^+]_i = 116 \text{ mM}; [Cl^-]_i = 46.3 \text{ mM};$$

$$P_{O, CaCC} = \frac{1}{1 + e^{-(V_m - V_{CaCC,h})/V_{CaCC}}},$$

$$[Ca^{2+}]_b = kB_{on} * [Ca^{2+}]_i / (kB_{on} * [Ca^{2+}]_i + kB_{off}) * B_T.$$

#### 4. Intercellular communication [129]

##### 4.1. Ionic coupling

$$I_{gj} = \sum_S I_{gj,S}$$

$$I_{gj,S} = Pz_S^2 \frac{V_{gj} F^2}{RT} \frac{[S]_i^n - [S]_i^m \exp(-z_S V_{gj} F / RT)}{1 - \exp(-z_S V_{gj} F / RT)}$$

$S = Ca^{2+}, K^+, Na^+, Cl^-$ ;  $V_{gj} = V_m^n - V_m^m$ ,  $n, m$  – cell index.

##### 4.2. $IP_3$ coupling

$$J_{IP3} = p_{IP3} ([IP_3]^n - [IP_3]^m)$$

##### 4.3. NO coupling

$$\bar{Q}_{NO,ss} = \frac{Q_{NO,ss}}{Q_{NO,max}} = \frac{[Ca^{2+}]_i^n}{[Ca^{2+}]_i^n + K_{m,Ca}^{NO}}$$

$$\frac{d\bar{Q}_{NO}}{dt} = \frac{\bar{Q}_{NO,ss} - \bar{Q}_{NO}}{\tau_{eNOS}}$$

$$[NO]^{SM} = [NO]_{max} \bar{Q}_{NO}$$

$$\tau_{eNOS} = 2 \text{ s}; K_{m,Ca}^{NO} = 300 \text{ nM}; n = 4.2; [NO]_{max} = 380 \text{ nM}.$$

APPENDIX B  
 ACCOUNTING FOR THICKNESS DIFFERENCES IN 2D FINITE ELEMENT  
 MODELS

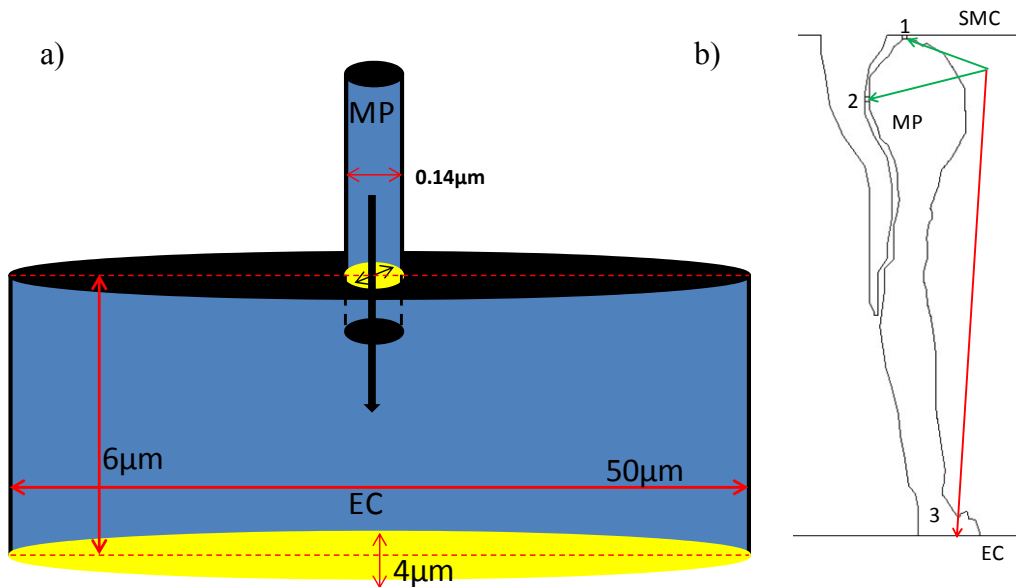


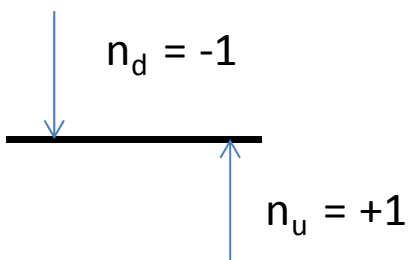
Figure A2.1: a) difference in area and thickness of MP with respect to the bulk EC, b) boundaries in the finite element model where discontinuity is applied.

Fluxes are accounted for at the boundaries between the MEGJs and the MPs as well as between MPs and EC bulk. This is done externally because the 2D model cannot recognize the different in thickness of the MP and the bulk EC.

Therefore, the discontinuity in fluxes at the shown boundaries is implemented using a discontinuity condition at the boundaries

a) Boundary 1: GJ1 to MP

The equation of discontinuity at the boundary in Nernst plank module in comsol is of the form





$$-n_u N_u - n_d N_d = N_0$$

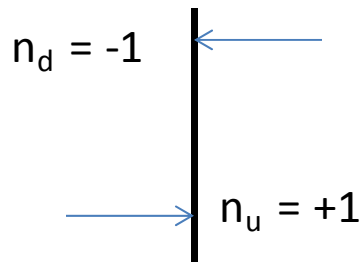
Where ‘N’ is the electrochemical flux (Eq. 4.4). At boundary 1, we want the incoming (downward flux) to be X times higher where X is the ratio of MP volume with height of MP same as EC (as implemented by default in the model) to actual volume of MP (calculated as the volume of a cylinder with the assumed area and height Figure A2.1a).

Therefore by replacing  $-n_d N_d$  in the equation to  $-n_d \cdot X \cdot N_d$ , we can calculate an expression for  $N_0$  as

$$N_0 = -(X - 1)N_d$$

b) Boundary 2: GJ2 to MP

The expression for  $N_0$  in this case is slightly different as we now need  $-n_u N_u$  to be

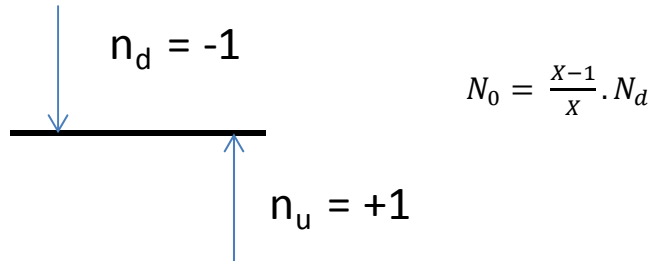


$-n_u \cdot X \cdot N_u$  (i.e. incoming flux higher). Substituting in the discontinuity equation, we get an expression for  $N_0$  as

$$N_0 = (X - 1)N_u$$

c) Boundary 3: MP to EC bulk

At this boundary, we need to reverse the action performed at the top two boundaries, as the flux is now diluted back into larger depth of EC bulk. Thus, at this location, we need  $-n_d N_d$  term to be  $-n_d \cdot \left(\frac{1}{X}\right) \cdot N_d$ . Substituting into the discontinuity equation, we get



$$N_0 = \frac{X-1}{X} \cdot N_d$$

Thus by adding these discontinuities to the three boundaries, we have accounted for the discontinuities in the thickness of MP and EC bulk. We have done a similar change for IP<sub>3</sub>. The only difference in IP<sub>3</sub> is that the flux term ( $N_0$ ) only contains a concentration gradient term and is not affected by  $V_m$  (see Eq 4.5).

## VITA

### SRIDEVI NAGARAJA

|           |   |
|-----------|---|
| 2006-2011 | Doctoral candidate, Department of Biomedical Engineering, Florida International University                              |
| 2005-2006 | Customer service associate at IBM Daksh, Mumbai, India  |
| 2001-2005 | Bachelor of Engineering, Instrumentation Engineering, Rajiv Gandhi Institute of technology, University of Mumbai, India |

### PUBLICATIONS AND CONFERENCE PROCEEDINGS

1. Kapela, A., S. Nagaraja and N. Tsoukias, 2009, "A mathematical model of vasoreactivity in rat mesenteric arterioles. II. Conducted vasoreactivity." *Am J Physiol Heart Circ Physiol* 298(1):H52-65
2. Kapela, A., S. Nagaraja, J. Parikh and N. Tsoukias, 2011, "Modeling  $Ca^{2+}$  signaling in the microcirculation: intercellular communication and vasoreactivity." *Critical reviews in biomedical engineering* (In press)
3. Cam Ha Tran, Mark Taylor, Frances Plane, Sridevi Nagaraja, et al. 2011, "Endothelial Calcium Wavelets and the Induction of Myoendothelial Feedback." *Am J Physiol Cell Physiol* (In review, C-00418-2011)
4. Nagaraja, S., A. Kapela and N. Tsoukias, 2011, "Modeling communication in myoendothelial projections." *Microcirculation* (In review, UMIC-2011-0117)
5. Nagaraja, S., A. Kapela and N. Tsoukias, 2011, "Myoendothelial projections in vasoreactivity: a theoretical study." (Manuscript completed, to be submitted)
6. Sridevi Nagaraja, Adam Kapela and Nikolaos Tsoukias. "Role of EC Projection in Myoendothelial Communication: A Theoretical Study", *FASEB J.* 2011 25:819.18

7. Sridevi Nagaraja, Adam Kapela and Nikolaos Tsoukias. " Microprojections amplify EC response to SMC stimulation: A theoretical study", FASEB J.2010 24:976.14

8. Adam Kapela, Sridevi Nagaraja and Nikolaos Tsoukias. " A theoretical study of myoendothelial communication: K<sup>+</sup> mediated EDHF signaling and the role of myoendothelial projections", FASEB J.2009 23:852.19

9. A.Kapela, T.Gadkari, S. Nagaraja and N.M.Tsoukias. "Multiscale mathematical modeling of microvascular tone regulation", IFMBE Proceedings 25th Southern Biomedical Engineering Conference 2009, 15 -- 17 May 2009, Miami, Florida, USA; 24: 297-298; ISBN: 978-3-642 -01696-7; 2009.